

Molecular Modeling of Ion Transport and Ion Sensing in Proteins

Tuğba Nur Öztürk

A Thesis
In the Department
of
Physics

Presented in Partial Fulfillment of the Requirements
For the Degree of
Doctor of Philosophy (Physics) at
Concordia University
Montreal, Quebec, Canada

July 2019

© Tuğba Nur Öztürk, 2019

**CONCORDIA UNIVERSITY
SCHOOL OF GRADUATE STUDIES**

This is to certify that the thesis prepared

By: **Tuğba Nur Öztürk**

Entitled: **Molecular Modeling of Ion Transport and Ion Sensing in Proteins**

and submitted in partial fulfillment of the requirements for the degree of

Doctor of Philosophy (Physics)

complies with the regulations of the University and meets the accepted standards with respect to originality and quality.

Signed by the final examining committee:

Dr. Uri Shalev

Chair

Dr. Sarah Rauscher

External Examiner

Dr. Christopher Brett

External to Program

Dr. Christophe Grova

Examiner

Dr. Laszlo Kalman

Examiner

Dr. Guillaume Lamoureux

Thesis Supervisor

Approved by

Dr. Valter Zazubovits, Graduate Program Director

July 30, 2019

Dr. André G. Roy, Dean, Faculty of Arts and Science

ABSTRACT

Molecular Modeling of Ion Transport and Ion Sensing in Proteins

Tuğba Nur Öztürk, Ph.D.

Concordia University, 2019

Molecular modeling complements conventional experiments by providing atomistic details behind the structural dynamics of transport proteins and unraveling the complex relationships among their structures and functions. In this thesis, we use molecular modeling to study the Orai channel and ProP transporter. Orai proteins function as store-operated calcium channels in most eukaryotic cells and are particularly interesting due to their high calcium selectivity, low conductance and unusual pore structures. We present molecular dynamics simulations of two Orai multimers – hexamer and tetramer – and examine their structural dynamics. The results show that the Orai tetramer retains most of the structural features of the hexamer, while creating a more tightly-packed hydrophobic pore. We then present free energy calculations of ion permeation through these multimers. To test whether the Orai pore can be opened via helix rotation, the multimers with rotated pore-forming helices were also simulated. Our results demonstrate that helix rotation significantly lowers the energy cost of ion translocation along the Orai pore, regardless of multimeric state. What depends on stoichiometry is the Ca^{2+} selectivity versus Na^+ . When opened, the hexameric pore is better adapted to Ca^{2+} permeation, displaying changes in relative permeabilities that are consistent with calcium-selective currents. Interestingly, the opening of the hexamer barely makes a difference for the permeation of Na^+ and K^+ ions, while opening the tetramer almost completely removes the barrier for these ions.

We also present our work on the *E. coli* ProP transporter, which pumps osmolytes into cells to prevent cellular dehydration as the cytoplasmic cation concentration increases. We built a homology model of the cytoplasmic C-terminal domain (CTD) of ProP that is implicated in osmosensing and performed molecular dynamics simulations to examine salt dependency in the

CTD-membrane association. The salinity dependence of the CTD-membrane interaction does not arise from changing salt bridge patterns. In fact, it correlates with a decrease in membrane fluidity due to increasing salinity.

To our knowledge, the studies presented here are the first computational work addressing the selectivity and permeation of Orai channels in two different multimeric states, as well as building a model structure of the cytoplasmic domain of ProP.

ACKNOWLEDGMENTS

First and foremost, I thank Dr. Guillaume Lamoureux for his continuous support and supervision. He led me out of my comfort zone from the very first day, and I gained stronger confidence in my abilities than I could have thought possible. Five years later, I am a better scientist for it. My gratitude extends to my committee members: Dr. Christophe Grova, Dr. Christopher Brett, Dr. Laszlo Kalman and Dr. Sarah Rauscher, for their valuable time and advice. My special thanks go to Dr. Janet Wood for her endless guidance, support and inspiring knowledge; I have learned so much from her.

My time in Concordia University could not have been the same without the GradProSkills team, more specifically Kristy Clarke, Racha Cheikh-Ibrahim and Cristina Barbu. Thank you so much for giving me the opportunity to design and facilitate several workshops on the topics that excited me the most. I will always feel lucky to have worked with you all. My gratitude also extends to Dr. Marleah Blom, Dr. Vivek Venkatesh, Joanne Rankin and all the members of the Center of Teaching and Learning. I am grateful for the support and the many teaching opportunities they have offered to me.

I have made amazing friends here and I should thank them all: my colleagues at CERMM for all the coffee breaks and board game nights; my amazing chemist friend, Hala Youssef, for answering all of my chemistry questions, listening to all of my rehearsal talks, and bringing me the best snacks (and post-its); and finally Rebecca, David and Serap for everything!

For the first time in my life, I was away from my family for so long. Mom, dad and my little brother, I can never thank you enough for everything. I know that you would support any one of my crazy ideas until the end. Let's hope this one was the last! I am also lucky and grateful to have built my second home, here in Montreal. Thank you, Maxime, for letting me be your shenanigan and for sketching so many ion channels for my talks. You and your amazing family made my life much better. Finally, Mousse, thank you for being such a good boy especially while mommy was writing her thesis.

Tuğba Nur Öztürk

To my family in Gökçeada and my family in Montréal.

Table of Contents

List of Figures	x
List of Tables	xii
List of Abbreviations	xiii
Chapter 1. Introduction	1
1.1. Orai Calcium Channel.....	5
1.2. ProP Osmolyte Transporter.....	9
Chapter 2. Computational Methods	13
2.1. Homology Modeling.....	13
2.1.1. Identifying the Template Sequence(s)	14
2.1.2. Aligning the Target Sequence with the Template Sequence(s)	14
2.1.3. Generating the Model Structure	15
2.1.4. Evaluating the Model.....	16
2.2. Molecular Dynamics	16
2.2.1. Equations of Motion	17
2.2.2. Force Fields	19
2.3. Enhanced Sampling Methods in Molecular Dynamics	21
2.3.1. Free Energy Calculations	22
2.3.2. Umbrella Sampling and Weighted Histogram Analysis Method	24
2.3.3. Adaptive Biasing Force Method	27
Chapter 3. Structural Dynamics of Orai Channels	29
3.1. Abstract	29
3.2. Introduction	30
3.3. Computational Details	32

3.3.1. Modeling of the Orai Channels	32
3.3.2. Simulation Setup	32
3.4. Results and Discussion	35
3.4.1. Structural Stability of the Closed and Open Orai Channels	35
3.4.2. Contacts within the Closed Orai Channels	35
3.4.3. Pore Structures of the Closed Orai Channels	42
3.4.4. Can a TM1 Helix Rotation Open Orai Channels?	44
3.5. Conclusion	51
Chapter 4. Origin of Ion Selectivity in Orai Channels.....	54
4.1. Abstract	54
4.2. Introduction	54
4.3. Computational Details	56
4.3.1. Modeling of the Closed and Open Orai Channels	56
4.3.2. Simulation Setup	57
4.3.3. Molecular Dynamics Simulations of the Orai Channels	58
4.3.4. Umbrella Sampling Simulations	59
4.4. Results and Discussion	60
4.4.1. Orai Channel Structure and Generation of the Models	60
4.4.2. Stability of Orai Channels	62
4.4.3. Ion Permeation through the Closed Hexameric and Tetrameric Channels ...	64
4.4.3.1. Closed Hexamer	64
4.4.3.2. Closed Tetramer	66
4.4.4. Ion Permeation through the Open Hexameric and Tetrameric Channels	68
4.4.4.1. Open Hexamer	69

4.4.4.2. Open Tetramer	70
4.4.5. Modeling of Calcium Ions for Biomolecular Simulations	72
4.5. Conclusion	73
Chapter 5. Modeling the Effect of Salinity on the Cytoplasmic Domain of ProP.....	76
5.1. Abstract	76
5.2. Introduction	76
5.3. Computational Details	78
5.3.1. Building Model Structures of the <i>E. coli</i> ProP CTD	78
5.3.2. Investigating the Conformational Dynamics of the loop	79
5.3.3. Building a More Realistic Model of the ProP Peptide	80
5.4. Results and Discussion	81
5.4.1. What can Molecular Dynamics Simulations of the ProP CTD Tell Us?	81
5.4.2. Residues 439-450 Form a Salt-Sensitive Loop.....	85
5.4.3. The CTD-Lipid Dissociation	87
5.5. Conclusion	91
Chapter 6. Conclusion	92
References	98

List of Figures

Figure 1.1. Gating mechanisms of channels	2
Figure 1.2. Primary and secondary active transporters	3
Figure 1.3. Crystal structure of <i>D. melanogaster</i> Orai protein (PDB ID: 4HKR)	7
Figure 1.4. Schematic diagram of the ProP structure	10
Figure 1.5. Proposed structural mechanism of ProP osmosensing	11
Figure 2.1. Periodic boundary conditions for a simple two-dimensional system	19
Figure 2.2. Bonded and non-bonded interaction terms in the CHARMM36 force field	20
Figure 2.3. The diagram of free energy calculations for ion permeation studies	27
Figure 3.1. The equilibrated structures of the closed and open Orai multimers	36
Figure 3.2. Contact probability maps of the closed Orai multimers	37
Figure 3.3. Salt bridges of the closed Orai multimers	41
Figure 3.4. Density profiles of salt ions and water molecules along the closed Orai pores	43
Figure 3.5. Contact probability maps of the open Orai multimers	45
Figure 3.6. Salt bridges of the open Orai multimers	48
Figure 3.7. Density profiles of salt ions and water molecules along the open Orai pores	50
Figure 4.1. Top and side views of the equilibrated Orai multimers	61
Figure 4.2. Distribution of pore-lining residues E178 inside the closed and open Orai pores	62
Figure 4.3. Free energy profiles for single Ca^{2+} , Na^{+} and K^{+} permeation through Orai pores	65
Figure 4.4. Free energy profiles for permeation of a single Ca^{2+} ion	69

Figure 4.5. Free energy profiles for permeation of a single hydrated Ca^{2+} ion	70
Figure 5.1. The sequences of the cytoplasmic C-terminal domains of ProP orthologues	77
Figure 5.2. The model structure of the ProP CTD peptide	82
Figure 5.3. Contacts between ProP-lipid head groups	84
Figure 5.4. Salt bridges within the ProP peptide.	85
Figure 5.5. Free energy profiles of the loop in solution under different salt concentrations.....	86
Figure 5.6. ProP-lipid salt bridges and the lipid order parameter	88

List of Tables

Table 1.1. Intracellular and extracellular concentrations of the most physiologically important inorganic ions found in the human body: Ca^{2+} , Cl^- , K^+ , Mg^{2+} and Na^+	1
Table 3.1. Hydrogen bonds constrained during the equilibration phase.....	34
Table 3.2. Significant contacts in the closed Orai multimers	38
Table 3.3. Significant contacts in the open Orai multimers.....	46
Table 4.1. NBFIX parameters used for interactions involving a Ca^{2+} ion.....	58
Table 4.2. Hydrogen bonds constrained during the equilibration phase.....	59
Table 4.3. Coordination of the permeant ions through the closed and open Orai channels	66
Table 5.1. The number of atoms in the simulation boxes.....	79
Table 5.2. The intra-peptide, peptide-salt/water/lipid contacts	83

List of Abbreviations

ABF	Adaptive Biasing Force method
ATP	Adenosine Triphosphate
CAR	Calcium Accumulating Region
CRAC	Calcium-Release Activated Calcium
Cryo-EM	Cryo-Electron Microscopy
CTD	Cytoplasmic C-terminal Domain
DOPE	Discrete Optimized Protein Energy
ER	Endoplasmic Reticulum
MD	Molecular Dynamics
MFS	Major Facilitator Superfamily
MscL	Mechanosensitive Channels of Large Conductance
NCBI	National Center for Biotechnology Information
NMR	Nuclear Magnetic Resonance
NPT	Isothermal–isobaric ensemble
NVT	Isothermal–isobaric ensemble
OPM	Orientations of Proteins in Membranes
PDB	Protein Data Bank
Phyre2	Protein Homology/Analogy Recognition Engine
PM	Plasma Membrane
PPM	Positioning of Proteins in Membrane
RMSD	Root-Mean-Square Deviation
STIM	Stromal Interaction Molecule
TM	Transmembrane
XRD	X-Ray Diffraction
WHAM	Weighted Histogram Analysis Method

Chapter 1. Introduction

Inorganic ions are necessary for cell survival. They play direct, physiological roles by interacting with proteins, lipids and nucleic acids, or are used as coupling ions to promote the transmembrane movement of other ions or organic solutes. For instance, Na^+ and K^+ play vital roles in (1) maintaining membrane potential; (2) balancing osmotic pressure on both sides of the cell membrane; and (3) generating nerve impulses [1,2]. Living systems maintain these ions at precise concentrations through a process called homeostatic regulation, which ensures that the physical and chemical conditions within cells conserve a steady state. This regulation necessitates the movement of ions across the cell membrane, as their concentrations are not static and vary in intracellular and extracellular fluids (see Table 1). In single cells, ion transport facilitates signalling, volume regulation and pH balance, while in higher organisms flow of ions also mediates muscle contraction, immune responses, secretion and proliferation [1,3].

The hydrophobic nature of the lipid bilayer that forms the cell membrane creates an energy barrier that acts against the permeation of most charged molecules, including inorganic ions. Allowing and controlling the precise flow of ions through the membrane therefore becomes the essential task of transport proteins, which are specialized to determine the types of ions permitted through, as well as when they may pass and in which direction. For instance, Ca^{2+} acts as an effective signal inside cells because its intracellular concentration is tightly controlled – at sub-micromolar levels – by Ca^{2+} -activated ATPase, a specific class of transport protein [4].

Table 1.1. Intracellular and extracellular concentrations of the most physiologically important inorganic ions found in the human body: Ca^{2+} , Cl^- , K^+ , Mg^{2+} and Na^+ [2,5]

Ion	Intracellular Concentration (mM)	Extracellular Concentration (mM)
Ca^{2+}	0.0001	2
Cl^-	4	104
K^+	140	4
Mg^{2+}	1	1
Na^+	10	140

Transport proteins are broadly divided into two classes: channels and transporters (the latter also known as pumps) [6,7]. Channels mediate the energetically favourable physical translocation of ions, and hence mediate the transport of small molecules via passive diffusion. Transporters, on the other hand, maintain a concentration gradient across the cell membrane by consuming energy to transport ions against their electrochemical potential.

Compared to the nonpolar membrane, a channel provides a hydrophilic—and therefore energetically favorable— permeation pathway for conducting certain types of ions [3]. The access to this pathway is altered by a conformational change known as gating, which can be used to categorize channels: voltage-gated channels open in response to changes in the membrane potential; ligand-gated channels open in response to the binding of a specific molecule; tension-gated channels open in response to stretch, pressure or shear (see Figure 1.1). The transport mechanism of an ion channel involves relatively little energetic interaction between the channel and its permeant ion [8], because the permeant ions move in the direction of their concentration gradient. Since channels mediate the physical translocation of ions in this thermodynamically downhill manner, their rate of ion transport is much faster compared to the rate by transporters. To be more precise, single channel studies revealed that the characteristic current through an open channel is around 1 pA, corresponding to 10^7 ions per second [9]. Transport rate is often used as a criterion to classify a transport protein as a channel or a transporter.

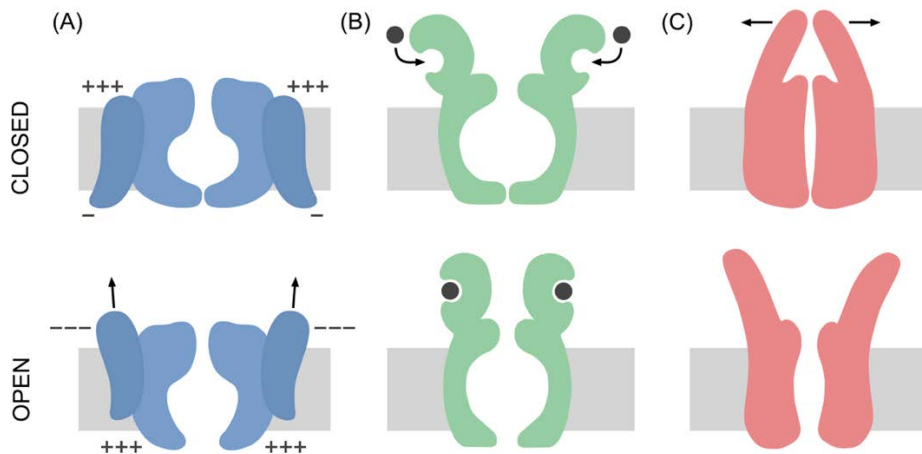


Figure 1.1. Gating mechanisms of (A) voltage-gated, (B) ligand-gated and (C) tension-gated channels (adapted from Ref. [9]).

In contrast with channels, transporters consume energy provided by ATP or the electrochemical potential gradient of a coupling ion to mediate the thermodynamically uphill transport of inorganic ions or organic solutes. Their transport mechanisms often involve one or more high affinity interaction with the substrate, resulting in transport rates several orders of magnitude slower than those of channels [3]. Transporters are also divided into two broad classes: primary active transporters that couple the movement of the transported molecule to the hydrolysis of ATP, and secondary active transporters that couple the movement of two (or more) inorganic ions, or of an inorganic ion and an organic molecule [8] (see Figure 1.2).

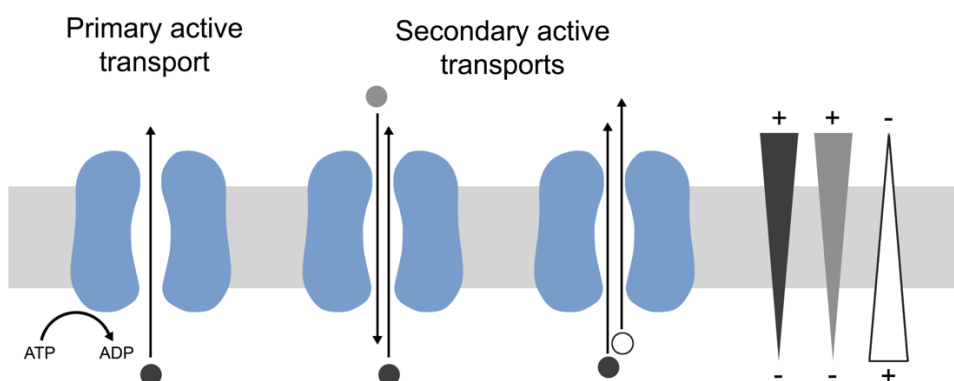


Figure 1.2. Primary and secondary active transporters (adapted from Ref. [10]). Secondary active transporters are named symporters if both ligands are transported in the same direction and antiporters if the ligands are transported in opposite directions. The diagrams given on the right show the electrochemical-potential gradients of the ligands. These ligands are often ions such as Cl^- , H^+ , K^+ and Na^+ .

Despite the difference in their transport rates, channels and transporters have several common features. For example, they act on both inorganic ions and organic solutes (with and without a net charge). In addition, they generally consist of transmembrane domains that are mostly formed of bundles of alpha helices. In the transmembrane domains, the side-chains of most amino acids are hydrophobic, whereas in the solvent-exposed regions, polar and charged amino acid side-chains can be found. The amino acids lining a permeation pathway often create a unique microenvironment that reduces the energetic cost of the translocation of the certain kind of ion for which the transport protein is selective. Transport proteins, regardless of their classes, are generally very selective for a certain kind of ion or molecule. The simplest definition of selectivity is the ability of a transport protein to select a specific ion type to permeate more easily – at a faster rate – than the other ions [7]. For example, Orai calcium channels, which will be one

of the main objects of the present study, show 1000-fold preference for Ca^{2+} ions against Na^{+} ions [11].

Transport proteins constitute an important class of membrane proteins, drawing increasing amount of attention in the field of cell biophysics due to their indirect or direct roles in almost every cellular function. The three-dimensional structures of these proteins have been characterized with experimental techniques such as X-ray diffraction (XRD), nuclear magnetic resonance (NMR) and cryo-electron microscopy (cryo-EM). The first crystal structure of an ion channel (the KcsA K^{+} channel) was determined by Doyle et al. using X-ray diffraction [12]. Even though it is static, the crystal structure of the KcsA channel provided insights into its high K^{+} selectivity. Such structural data also provide a starting point for molecular dynamics simulations, with which a biomolecular system (such as a transport protein) can be simulated by employing Newton's second law. These simulations predict dynamic processes with a high level of temporal and spatial resolution that is not possible through experimental methods [13,14]. In addition, a typical molecular dynamics simulation investigates the dynamics of a transport protein embedded into a lipid bilayer and solvated by water and salt ions, whereas some crystallography experiments lack a realistic membrane environment. Consequently, molecular dynamics have become a popular modeling method to elucidate the underlying physical mechanisms of transport proteins, and to relate functional measurements to structural data in atomic detail [7,15–17]. For example, molecular dynamics studies of the following transport proteins have complemented experimental studies to shed light on the relationship between the structures and functions of these proteins: gramicidin A channels [18], KcsA channels [19,20], NaK channels [20], LeuT transporters [21], and $\text{Na}^{+}/\text{K}^{+}$ pumps [22]. More recent molecular dynamics studies cover a wide range of channels and transporters such as the Ca^{+} selective voltage-gated channel $\text{Ca}_v1.2$ [23], the serotonin transporter SERT [24], and the Na^{+} -coupled betaine transporter BetP [25]. In the last decade, it has become possible to perform microsecond-long molecular dynamics simulations of individual transport proteins in almost native environments (all-atom models of membranes, water and salt ions) [7,26]. As technology advances, molecular dynamics can be used for the investigation of larger biomolecular systems for longer timescales.

The studies presented in this thesis focus on two transport proteins: the Orai calcium channel and the ProP osmolyte transporter. In addition to being classified in different classes of transport proteins, these proteins are also exposed to different cellular environments. The former is a eukaryotic channel whereas the latter is a prokaryotic transporter. Here we use molecular modeling methods to study these two structurally and functionally different transport proteins. The next two sections present each protein and explain our aims for studying them. Chapter 2 describes the computational methods used in the studies presented here: homology modeling, molecular dynamics, and molecular dynamics combined with enhanced sampling methods. Chapter 3 presents the computational investigation of conformational dynamics of hexameric and tetrameric Orai proteins. Chapter 4 investigates the free energy profiles of translocating single ions along the pores of these proteins. Chapter 5 presents our study on understanding the role of the C-terminal domain of the ProP transporter in osmosensing. Finally, Chapter 6 emphasizes the conclusions of these studies and suggests an outlook for future research.

1.1. Orai Calcium Channel

Intracellular Ca^{2+} concentrations are tightly regulated by Ca^{2+} transporters in the plasma membrane (PM) and in the endoplasmic and sarcoplasmic reticulum membranes of eukaryotic cells. These transporters can maintain the intracellular Ca^{2+} concentration up to 20 000 times lower than in the extracellular milieu [27]. Cells use Ca^{2+} as a crucial signalling messenger for several cellular functions including muscle contraction, immune activation, and proliferation; and low intracellular concentrations make cells sensitive to Ca^{2+} perturbations [27–29]. One of the most conserved mechanisms of Ca^{2+} influx is mediated by Ca^{2+} release-activated Ca^{2+} (CRAC) channels. These channels are activated when Ca^{2+} stores in the endoplasmic reticulum (ER) are depleted. In 2005, an ER membrane protein named stromal interacting molecule (STIM) was identified as the calcium sensor of these channels [30–32]. A year later, a plasma membrane protein – Orai – was identified as the pore subunit of these channels [33–35]. Other names have been subsequently given to these channels including store-operated calcium channels and Orai calcium channels.

Over the last decade, CRAC channels have attracted attention because of the distinct features of the Ca^{2+} currents they generate: low single-channel conductance, high calcium selectivity against Na^+ and K^+ , direct dependency on Ca^{2+} stores of the ER, inward rectification and independence

from the membrane voltage [27]. CRAC channels continue to provide an interesting field of research mostly due to three unresolved issues: (1) how Orai channels are gated by STIM proteins; (2) how Orai proteins with different oligomeric states selectively mediate Ca^{2+} flux; and (3) how their unusual pore environment mediates Ca^{2+} permeation.

Orai proteins are activated by STIM proteins which function as Ca^{2+} sensors in the ER. When the Ca^{2+} concentration in the ER decreases, STIM proteins oligomerize and diffuse to the ER-PM junction. There, they interact with Orai dimers and multimerize them. The binding of STIM proteins opens the pores of Orai channels, initiating Ca^{2+} entry into the cell mediated by Orai proteins. The underlying mechanism behind the gating of Orai channels is not fully understood: where STIM binds and how it gates the Orai proteins are still subjects of interest [29,36]. Studies of the STIM:Orai ratio have yielded different results including 1:1 [37] and 2:1 [36,38,39]. In general, STIM is believed to interact strongly with the C-terminus of the Orai protein [37] and weakly with the N-terminus [39–41]. For example, a recent study revealed that STIM is likely to interact with the C-terminus of the Orai protein indirectly while forming a unique dynamical coupling with Orai: STIM not only multimerizes and gates Orai, but also alters its Ca^{2+} selectivity [36]. That being said, the gating mechanism of Orai channels and stoichiometry of the Orai-STIM machinery remain open questions in the field.

Following the identification of Orai as the CRAC pore subunit, several studies concluded that CRAC channels are active as a tetrameric assembly of Orai proteins [42–50]. That conception has remained the most widely accepted, though other oligomeric states of Orai proteins have been reported [51–53]. However, the arrival of the first crystal structure of the *Drosophila melanogaster* Orai protein [11] challenged the established idea that the tetrameric assembly of Orai is the active channel. In fact, some studies identified the functional Orai as a hexamer [36,54–56], and store-operated calcium entries were also detected using different Orai1 concatemers, including dimers, tetramers and hexamers [55]. None of these studies have explained the differences between these multimeric states; their focus simply shifts from tetramer to hexamer.

The *D. melanogaster* Orai is a member of the conserved family of Orai proteins and shares 73% sequence identity with its human ortholog, Orai1. The crystal structure of the Orai protein

revealed a hexamer assembly of its subunits [11] (see Figure 1.3). Each subunit consists of four transmembrane helices (TM1-TM4) followed by a cytosolic helix (TM4-extension) that adopts two different conformations in the neighbouring subunits: in one subunit, the TM4-extension helix extends toward the cytosol, whereas in the next subunit it bends backward toward the neighbouring subunit. This gives a threefold symmetry to the channel in its outer helical ring, and the rest shows a six-fold symmetry.

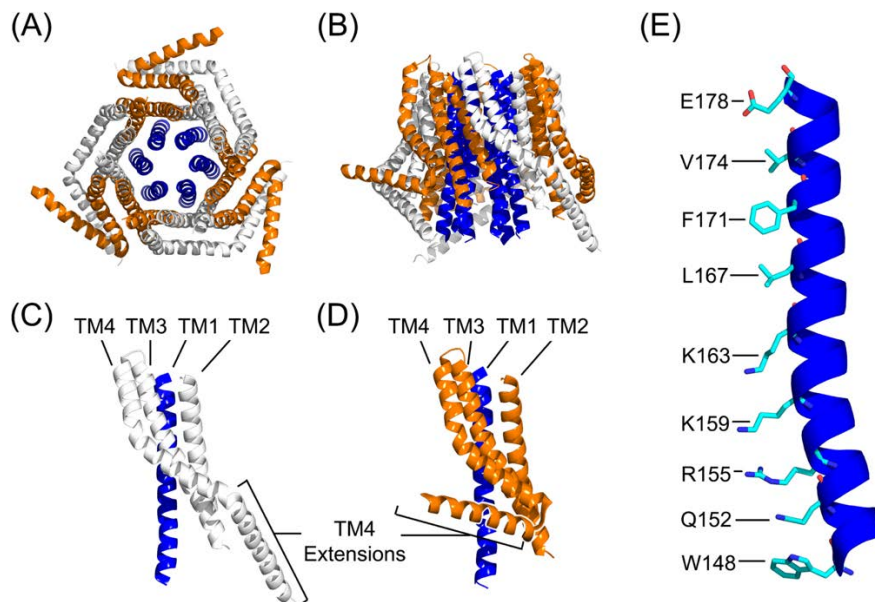


Figure 1.3. Crystal structure of *D. melanogaster* Orai protein (PDB ID: 4HKR) [12]. (A) Top and (B) side views of the Orai channel, comprised of six Orai subunits. In each subunit, the TM1 helices that form the ion pore are colored in blue. (C) In one subunit, the rest of the transmembrane helices (TM2, TM3, TM4 and TM4-extension helices) are shown in white. The TM4-extension helix of subunit A extends toward the cytosol. (D) In the neighbouring subunit B, the TM2, TM3, TM4 and TM4-extension helices are shown in orange. In this subunit, the TM4-extension helix adopts a different conformation; it bends toward subunit A. The conformation difference in TM4-extension helices causes Orai channels to have a three-fold symmetry. (E) The side view of the TM1 helix is shown in the cartoon representation, with the pore-lining residues shown in the licorice representation.

The pore of the Orai crystal, formed by a ring of TM1 helices, was found in a closed conformation [11]. On the extracellular side, there is a short selectivity filter formed by the E178 residues of the TM1 helices (Figure 1.3E). The hydrophobic region of the pore, formed by V174, F171 and L167, is followed by the basic region lined by K163, K159 and R155. The pore, formed by Q152 and W148, then widens toward the cytosol with a diameter larger than 10 Å. A ring of glutamate residues is often found in voltage-gated Ca^{2+} as well as Na^{+} channels. However, the basic region is unique to Orai channels. Even though the crystal structure presents a binding site for anions stabilizing the basic region in the closed conformation of the Orai

channel, it is still uncommon for a cation channel to have a pore lined with eighteen basic amino acids (residues K163, K159, R155 for each Orai subunit) [11,57].

Be it their gating mechanism, multimeric state or permeation mechanism, Orai channels provide an unusual environment for Ca^{2+} permeation. Since 2012, experimental studies have focused on understanding how Orai channels function. Fortunately, with the arrival of the crystal structure from the *D. melanogaster* Orai, computational studies can also address these questions and provide atomistic details. Dong et al. computationally studied Na^+ permeation along the pores of the wild-type *D. melanogaster* Orai and its conductive variant (V174A), and concluded that the Orai channel is likely to be regulated by water molecules in its pore [58]. In another study, Alansary et al. built homology models of the *Homo sapiens* Orai1 and the Orai-interacting domain of Stim1 to examine the effect of interactions between TM3 and TM4 helices of Orai on channel activation using molecular dynamics simulations. They identified a residue as a potential candidate for further drug design studies [59]. Similarly, in another study [60], four potential inhibitors of the *H. sapiens* Orai1 protein were investigated using molecular modeling and docking approaches. In contrast, Maganti et al. [61,62] performed molecular dynamics simulations to examine calmodulin binding to the Orai1 channel. Several studies focused on a Ca^{2+} accumulating region (CAR) located in the loop connecting TM1 and TM2, and used both experimental and computational approaches to investigate the role of N-terminal helices on the activation mechanism of Orai channels [63–66]. More recently, Yamashita et al. [67] and Yeung et al. [68], combining experiments with molecular dynamics simulations to study the wild-type Orai1 and its variants, proposed that STIM proteins activate Orai channels by rotating its pore-forming inner helices. These authors did not explore their hypothesis with free energy calculation methods (see Section 2.3).

Even though Orai proteins have been extensively examined in the last decade, several questions about them remain unanswered. Understanding how these channels function is of particular importance since these proteins are implicated in several diseases. For example, in humans, gain-of-function mutations in Orai proteins are known to cause tubular aggregate myopathy [69,70], whereas their loss-of-function mutations result in immunodeficiency [71,72], hypotonia (muscle weakness) [73], ectodermal dysplasia [74,75], and nonprogressive myopathy [76]. Consequently, the aim of Chapter 3 and 4 of this thesis is to answer the following questions: (1) Can Orai

proteins form tetramer assemblies as well-packed as hexamer assemblies and do their dynamics differ significantly? and (2) Can the selective permeation of Ca^{2+} along the pores of hexameric and tetrameric assemblies of Orai proteins be studied using molecular dynamics simulations in atomic detail?

1.2. ProP Osmolyte Transporter

Osmosensing and osmoregulation are important for cell survival. Cells must respond to changes in their environment rapidly. Changes in extracellular osmolality provoke water flow across the membrane, and therefore directly alter intracellular water activity. In a physicochemical sense, water activity affects cell volume, membrane tension, cytoplasmic viscosity, membrane potential and ion gradients [77,78]. This alters interactions among biomolecules, including ions and proteins. As a response to changes in their environments, transport proteins residing in the cell membrane are expected to undergo conformational changes and to alter their interactions with the lipid membrane [78].

Bacterial cytoplasmic membranes are highly permeable to water and cellular hydration can be altered in microseconds [77]. To survive, bacterial cells must respond to water flux into or out of their membrane. They do so by releasing or accumulating small organic solutes and electrolytes. This mechanism, known as the osmoregulatory response, is carried out by both mechanosensitive channels and osmoregulatory transporters [79]. Mechanosensitive channels open in response to forces exerted by the lipid membrane, and release osmolytes from the cytoplasm when the external osmolality decreases unexpectedly. Alternatively, osmoregulatory transporters mediate cytoplasmic accumulation of osmolytes as the external osmolality increases. The signals to which these transporters respond have been the subject of extensive investigation [80]. In *Escherichia coli* (*E. coli*), a H^+ /osmoprotectant symporter named ProP functions both as an osmosensor and an osmoregulator. It mediates the accumulation of osmolytes such as proline and glycine betaine [81–83], and is activated as the external osmolality increases.

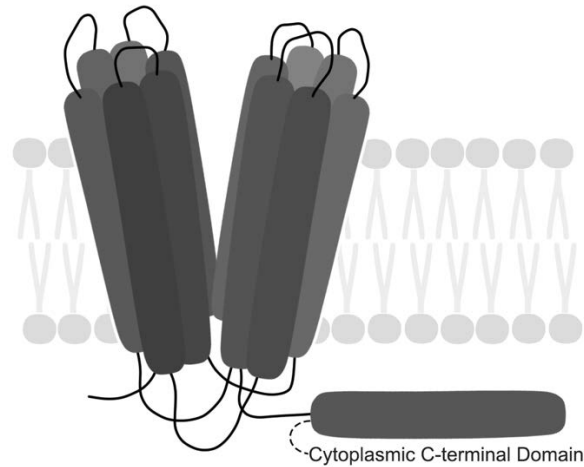


Figure 1.4. Schematic diagram of the ProP structure (adapted from Ref. [78]). ProP consists of 12 transmembrane helices forming two adjacent ellipsoids and an anionic, cytoplasmic C-terminal domain (CTD).

ProP is a 500 amino acid residue Major Facilitator Superfamily (MFS) member, residing in the cytoplasmic membrane [84]. Like other MFS members, ProP consists of 12 transmembrane helices (TMs) integral to the membrane [84]. Unlike its paralogs, ProP also includes an extended, charged cytoplasmic C-terminal domain (CTD) connected to transmembrane helix XII [84]. The CTD of ProP is implicated in its activity and it forms a homodimeric, antiparallel, alpha-helical coiled-coil with an adjacent ProP [83,85,86]. ProP activity forms a sigmoid function of the osmolality in intact cells and in proteoliposomes reconstituted with the purified protein [80,81,87]. Thus, ProP serves both as an osmosensor and an osmoregulator, in its lipid environment, and in the absence of other proteins. A thermodynamic analysis of the osmotic activation of ProP in proteoliposomes supported a two-state model, in which ProP—from an inactive form—is activated when the inorganic cation concentration of the proteoliposomes lumen increases, as a result of increasing osmolality of the external medium [88]. The cation effect was found not to be ion-specific [88] and an increase in the luminal concentration of a noncharged but polar molecule, glucose, did not activate ProP [87]. Taken together, these studies implied that Coulombic effects were critical to the osmotic activation mechanism. Such effects might include the proximity of ProP and the lipid; folding or assembly of anionic CTDs; and/or an increase in local membrane surface charge density [88]. The osmolality at which ProP activates is modulated by the proportion of anionic phospholipids in its host membrane, indicating that interactions between ProP and lipids might also play a role in osmosensing [89].

On one hand, several studies [83,86,89,90] indicated that some modifications to the CTD, including the part forming the coiled-coil, profoundly affect ProP activity and the osmotic activation of ProP. On the other hand, the coiled-coil is not essential for osmosensing since there are osmosensing ProP orthologues lacking the coiled-coil domain [91]. These seemingly paradoxical findings contribute to making the effect of the CTD in the osmosensing mechanism of ProP a complex, open question.

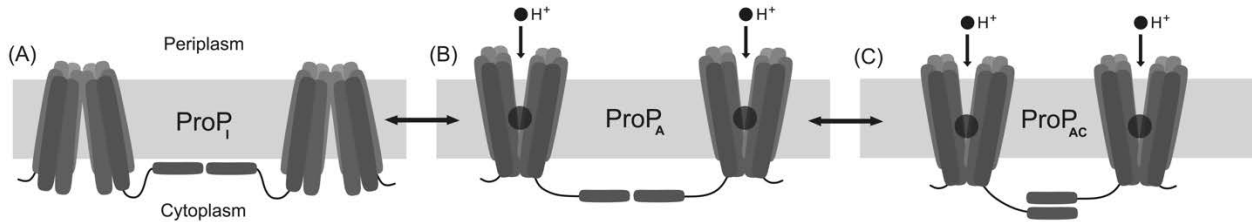


Figure 1.5. Proposed structural mechanism (adapted from Ref. [91]). According to this model, ProP may exist in three forms: ProP_I, ProP_A and ProP_{AC}. (A) When inactive, the CTD associates with the membrane and locks the protein in an inactive, inward-facing conformation, ProP_I. (B) Increasing cytoplasmic cation concentration weakens the CTD-membrane interaction. Then, ProP_A is active and free to alternate between the inward and outward facing conformations. (C) Two adjacent ProP CTDs form an alpha-helical coiled-coil stabilizing an active conformation. Coiled-coil formation prevents the CTD from returning to the membrane surface since the arrangements of the CTDs in the ProP_I and ProP_{AC} are mutually exclusive as concluded in our previous work [91]. H⁺ and osmolytes are shown as small and large circles, respectively. The distribution of ProP transporters in these three conformations is modulated by osmolality: ProP_I would be favored in low osmolality, and ProP_A and ProP_{AC} in high osmolality.

Our previous work [91] showed that the ProP CTD can either form a coiled-coil dimer or associate as a monomer with the surface of the anionic *E. coli* lipid membrane. Therefore, we proposed a model for the activation mechanism of ProP by comparing (1) the osmolality dependence of the activities of ProP sequence variants; (2) interactions between corresponding peptides and liposomes [90]; and (3) direct effects of salt on the membrane lipid [91]. According to the model, the CTD-membrane association locks ProP in an inactive conformation. That association is destabilized as the cytoplasmic cation concentration increases. In the active ProP the CTD is released, and then is stabilized by the coiled-coil formation. Several factors may contribute to this phenomenon: (1) increasing salt concentrations affecting the membrane lipid (decreasing the membrane fluidity [91]) as well as the loop connecting TMXII to the CTD helix; (2) salt bridges and hydrogen bonds between the CTD-membrane; and (3) interactions within the ProP peptide.

Chapter 5 presents our study of ProP transporters in collaboration with Dr. Janet Wood's laboratory, and it aims to build a realistic model of the C-terminal domain (CTD) of ProP in order to understand the role the CTD plays in osmotic activation of ProP. Our modeling approach is specifically tailored to interpret complex experimental data by probing the interactions between the ProP CTD and the membrane at atomic resolution. Here, we present only the computational part of the project revealing new insights regarding the salt dependence of the CTD-membrane interaction.

Chapter 2. Computational Methods

This chapter covers the computational methods used in the studies presented in this thesis: homology modeling, molecular dynamics and two of the enhanced molecular dynamics methods capable of estimating the free energy of a system – the umbrella sampling and the adaptive biasing force method.

2.1. Homology Modeling

The function of a protein is determined by its three-dimensional structure, and thereby its sequence. Protein structures can be experimentally determined by X-ray diffraction (XRD), nuclear magnetic resonance (NMR) spectroscopy or cryo-electron microscopy (cryo-EM) methods. However, membrane proteins are difficult to purify and crystallize due to their large hydrophobic domains, their flexibility and their tendency to aggregate in solution [92]. In theory, the amino acid sequence of a protein can be used to determine its structure [93]. When a sequence-level similarity exists between two proteins, structure similarities between them can be expected, since compared to their sequences the three dimensional structures of proteins from the same family are more conserved [94–96]. When there is no available structure for a protein of interest, its structure needs to be predicted so that it can provide a starting point for molecular dynamics-based studies, including protein-protein or protein-membrane interactions, ligand binding, ion selectivity and gating mechanisms of transport proteins.

Homology modeling, also known as comparative modeling, generates the most probable structure of a protein (target) by satisfying spatial restraints built based on its alignment with a related protein sequence (template) whose structure is known [97]. In the studies included in this thesis, MODELLER [97] was used for homology modeling. Therefore, homology modeling will be explained through MODELLER for the rest of this section. MODELLER is a Python module which requires three input files: a text file of the alignment between the template sequence and the target sequence; the atomic coordinates of the structure of the template protein in the Protein Data Bank (PDB) file format; and a Python script including the details of the model generation [98,99]. The prediction of a three-dimensional structure of a sequence of interest, using homology modeling, can be explained in four main steps: (1) identifying a template sequence;

(2) aligning the template and the target sequences; (3) generating a model structure; and (4) evaluating the model [99].

2.1.1. Identifying the Template Sequence(s)

The first step of homology modeling is the identification of one or more template sequences with known structures that are related to the target protein. This step often begins with a search on the PDB for any known structures of the target protein. Then several databases, including NCBI [100] and PDB [101], can be used to search for template proteins that are similar to the target protein. A multiple sequence alignment and phylogenetic tree can be helpful to identify the templates from the closest subfamily of the target protein [93,97,98]. In general, the most important criteria when identifying the potential templates are to satisfy the highest possible sequence similarity between them and the target sequence; and to minimize the number and the length of gaps in the alignment [98]. It is also worthwhile to consider the similarity of the target and template's environment (such as solvent, pH and ligands), and the resolution of the template's experimental crystal structure.

2.1.2. Aligning the Target Sequence with the Template Sequence(s)

The following step is the alignment of the target to one or multiple template sequences. If the sequence identity between the template and target sequences is above 50%, their alignment could be straightforward [93]. In the case of a sequence identity lower than 50%, the alignment should be done carefully. If necessary, the alignment should be revised, and model building should be repeated accordingly. Careful attention should be given to certain details of the procedure to facilitate alignment, for example: minimizing the number of gaps and the number of misaligned residues in the alignment; avoiding the gaps in the buried regions or between two residues that are separated by a large distance; choosing multiple sequences from a non-redundant sequence database; and superposing the aligned regions in the presence of multiple templates [93,98].

When sequence identity is low (below 25%), alignment becomes technically challenging and may result in inaccuracies in the homology model. However, it might be necessary to build a partial and not very accurate model to be used in computational studies combined with laboratory experiments directed towards understanding the function of a protein. In the case of low sequence identity with the template, the model of the target protein might differ significantly

from its real structure. But the different parts of this model can still be reliably used to derive useful information about the protein, as is convincingly shown in a study involving the NS3 protease domain of the hepatitis C virus [102]. In Chapter 5, we built a homology model of the *E. coli* ProP transporter using the XylE xylose transporter of *E. coli* as a template. The sequence identity between these proteins are 20%. Yet, we chose to use a part of this model that corresponds to the transmembrane helix XII.

2.1.3. Generating the Model Structure

Several methods can build a homology model of the target sequence: rigid body assembly, segment matching and spatial restraints [98,99,103]. MODELLER constructs a three-dimensional structure of the target sequence by satisfying spatial restraints. These restraints may include homology restraints (based on the distance and dihedral angles extracted from the alignment between the target and template sequences), stereochemical restraints (based on the bond length and bond angle parameters from the CHARMM force field), statistical restraints (on the dihedral angles and side-chain conformations (rotamers) extracted from a set of representative protein structures) and/or optional restraints defined by the user [97,98].

After constructing the backbone atoms, MODELLER uses a knowledge-based approach to choose the rotamers, guided by the rotamer libraries extracted from high-resolution crystal structures [93,97,99]. For the residues in the hydrophobic core of a protein, the prediction accuracy of the rotamers is high compared to those for the surface residues. This is due to the flexibility of surface residues and the lack of accuracy in energy score function for the rotamers when it comes to describing complicated electrostatic interactions and associated entropy effects [93]. Once all the protein atoms excluding the hydrogen atoms are constructed, MODELLER optimizes the model structure by running molecular dynamics simulation. The loops connecting the alpha helical domains (or beta sheet domains) of proteins are flexible, and therefore especially difficult to crystallize. MODELLER builds the loops by calculating a pseudo-energy function of distance and dihedral terms from CHARMM force field, as well as spatial restraints based on the known protein structures [98]. It then it optimizes this energy function using conjugate gradient method and molecular dynamics with simulated annealing [93,98].

2.1.4. Evaluating the Model

As the sequence identity increases between the target and the template(s), the accuracy of the predicted structure increases. If the sequence identity is less than 30%, the predicted structure can be unreliable [93,98]. To assess the model quality, MODELLER calculates two quantities: the objective function measuring how well the spatial restraints are satisfied and the discrete optimized protein energy (DOPE) score based on a statistical potential as a function of atomic distances [99]. Lower values in both quantities correspond to more accurate predictions of the structure. In addition, a predicted model should be consistent with the known experimental observations of the target protein.

2.2. Molecular Dynamics

Molecular simulation techniques are fundamental tools for understanding and predicting the properties, structures and functions of molecular systems. They are particularly crucial for studying complex systems, interpreting experimental data via the motions of molecules, and quantitatively predicting molecular properties [104]. For example, a protein structure should be considered only a snapshot of the protein under the crystallization conditions; by itself, the protein structure is not enough to understand how the protein functions. Since proteins are dynamic polymers made of amino acids, it is essential that the dynamics of a protein structure be investigated in order to understand its function or to predict its properties.

The idea behind any molecular simulation technique is to build a particle-based model of the system of interest, propagate the system deterministically or probabilistically, and then generate the evolution of this system over the time frame of the simulation (i.e. generate a trajectory of the system where each frame (or snapshot) is a configuration of its particles) [104]. If the system of interest is propagated deterministically using Newton's second law, the molecular simulation technique is known more specifically as molecular dynamics.

Molecular simulation methods can describe the particle-based model of a system using different theories. If Newtonian mechanics is used, the method uses a molecular mechanics description to represent the atoms of the simulation system. The method works under the Born-Oppenheimer approximation (the motion of atomic nuclei and electrons can be separated), so that the energy of a system in question can be written as a function of nuclear coordinates. In other words, the

motion of electrons is ignored. Generally, electrostatic interactions are described using partial atomic charges assigned to every atom in the simulation system. Therefore, molecular simulations cannot be used for estimating any property that depends on the electronic distribution of a molecule such as electronic transitions or proton transfer [105]. Additionally, in such simulations, pH refers to the selection of fixed protonation states [104]. In contrast, the quantum mechanical description of any system is of high accuracy and involves the explicit representation of electrons. However, it requires several approximations and few empirical parameters to calculate the electronic structure of the molecules in the system. Therefore, it is more computationally expensive. Another drawback of using the quantum mechanical description of a system is its size limitation: quantum mechanical simulations can be performed for small systems (roughly hundreds of atoms) whereas classical mechanical representation of a molecular system, such as in molecular dynamics, allows us to study larger systems (roughly hundreds of thousands of atoms) [104].

2.2.1. Equations of Motion

Molecular dynamics uses Newton's second law to generate a trajectory of the biomolecular system of interest – a movie in atomic resolution. At each snapshot of this movie, the positions, velocities and forces acting on each atom in the biomolecular system are computed. Since atoms are classically modelled under the Born-Oppenheimer approximation, measurable observables must be expressed as a function of the positions and velocities (or momenta) of the atoms in the system [106].

To start a molecular dynamics simulation, an initial structure (i.e. the coordinates of all atoms) of the system is needed. The initial velocities of the atoms are assigned randomly from a Maxwell distribution in such a way that the total momentum of the system is zero. The velocities (v) of all the atoms are used for calculating an instantaneous temperature of the system:

$$k_B T(t) = \sum_{i=1}^N \frac{m_i v_i^2(t)}{N_f} \quad (1)$$

The velocities ($v_i(t)$) are adjusted so that the instantaneous temperature ($T(t)$) matches the desired temperature [106]. In Equation 1, k_B , N_f and m_i represent the Boltzmann constant, the number of

atoms in the simulation system and the mass of the i th atom, respectively. Newton's second law is employed to calculate the force (F_i) acting on the atom i and the potential energy function (U).

$$F_i = m \frac{\partial^2 r_i(t)}{\partial t^2} = -\frac{\partial U}{\partial r_i} \quad (2)$$

For large systems composed of more than three interacting particles without constrained degrees of freedom, there is no analytical solution to the equations of motion [104,106]. Therefore, a numerical integration of the equations of motion is required. Numerical integration can be thought as of taking small, discrete steps in time. The most widely used integrators are the Velocity Verlet or Leapfrog algorithms which generate a numerical solution to the equations of motion [105,107]. The numerical integration requires a small time step (Δt) [107]. At each time step, the forces acting on each atom are calculated again; and new positions and velocities are updated accordingly.

Molecular dynamics simulations of biomolecular systems are often performed at a constant pressure and temperature (in the NPT ensemble) to mimic the conditions of a laboratory experiment. Throughout a simulation, barostat and thermostat algorithms are employed to keep pressure and temperature constant. For example, NAMD, one of the most widely used molecular dynamics software, uses the Langevin piston Nosé-Hoover method in which the pressure and temperature of the simulation system are fixed by adjusting the volume of the simulation box and rescaling all atomic coordinates and velocities [108,109]. To avoid the boundary effect caused by the finite size of the simulation cell, periodic boundary conditions are applied: if an atom leaves the simulation cell from one side, the same atom appears from the opposite side of the simulation cell (see Figure 2.1). With periodic boundary conditions, the simulation of a small system provides a good estimation of a larger bulk phase's behavior [104]. To reduce the computational cost, periodic boundary conditions are often employed with a cut-off distance for non-bonded interactions. Generally, the cut-off distance is chosen to be smaller than half of the length of the simulation box in any dimension [104–106].

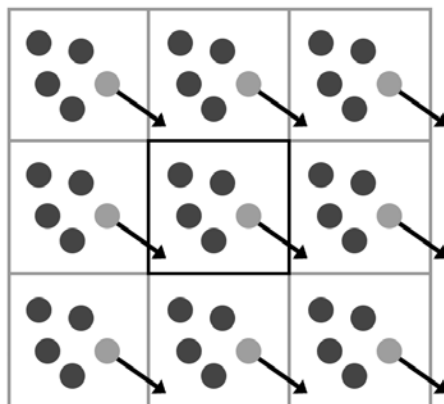


Figure 2.1. Periodic boundary conditions are shown for a simple two-dimensional system. The simulation system, shown in the center, is a sub-system among an infinite, identical systems. When an atom leaves the simulation box, the same atom enters the simulation cell from the opposite side.

2.2.2. Force Fields

Molecular mechanics models each atom in the simulation system as a hard sphere that feels forces which depend on the atom's position and its interaction with its environment. This approach requires a set of parameters, known as a force field, to describe the bonded and non-bonded interactions of the simulation system. Force fields are generated semi-empirically from electronic structure calculations and experimental data on small molecules [105]. An appropriate force field must be chosen in order to calculate the potential energy function (U) of a simulation system as a function of atomic positions. At each time step t , the potential energy function is computed as a summation of all bonded and non-bonded energy terms and is used to calculate the forces acting on each atom in the simulation system.

Most force fields describe the bonded interactions (the interactions within a molecule) in terms of bond stretching (U_{bonds}), angle fluctuations (U_{angles}), and rotations about single bonds ($U_{\text{dihedrals}}$). Depending on the choice of force field, different functional terms might be included in the potential energy function of a simulation system. For example, the CHARMM force field possesses an additional two terms for describing the bonded interactions: the impropers term representing the changes in energy due to the out of plane bending and the Urey-Bradley term restraining the changes in the distance between two atoms separated by two bonds [110].

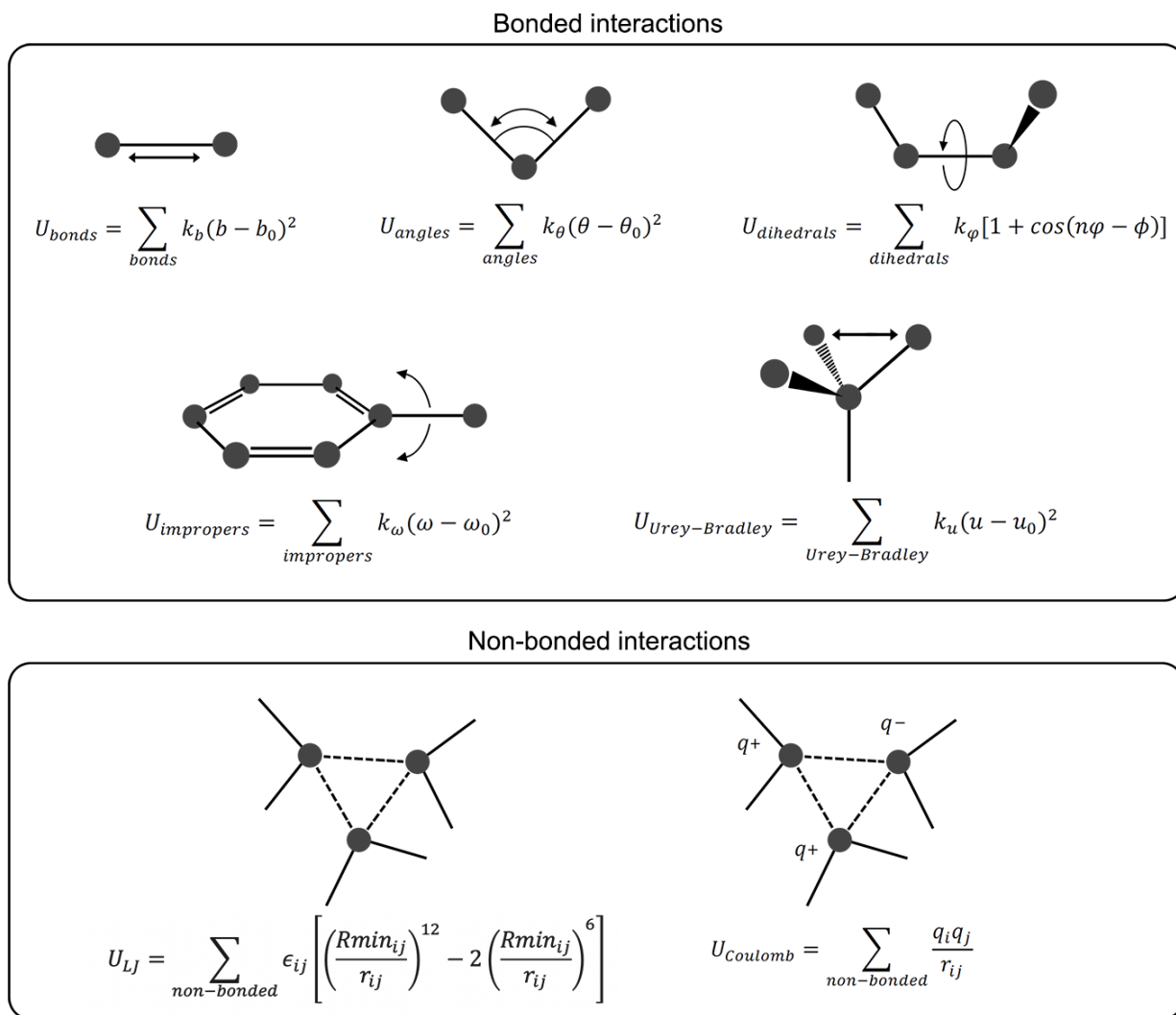


Figure 2.2. Bonded and non-bonded interaction terms in the CHARMM36 force field. Changes in energy due to bond stretching (U_{bonds}); valence angles (i.e. angles between three bonded atoms) (U_{angles}); out-of-plane bending ($U_{impropers}$); and changes in the distance between two atoms separated by two bonds ($U_{Urey-Bradley}$) are described using harmonic potentials. In the formulas given for each energy term, k represents the force constant whereas b_0 , θ_0 , ω_0 and u_0 show equilibrium bond length, equilibrium valence angle, equilibrium improper angle and equilibrium Urey-Bradley distance, respectively. For example, in the U_{bonds} term, the deviations from the equilibrium bond length for each possible atom pair cause an energy penalty that depends on the force constant defined for that atom pair (k_b). The dihedral energy term, $U_{dihedrals}$, describes changes in energy due to rotations around bonds. In this term, k_ϕ is the force constant; n is the multiplicity of the function; ϕ is the dihedral angle; and ϕ is the phase shift. Non-bonded interactions are represented by two terms: U_{LJ} and $U_{Coulomb}$. In the former, ϵ_{ij} and $Rmin_{ij}$ are atomic Lennard-Jones parameters: ϵ_{ij} is the depth of the potential well and $Rmin_{ij}$ is the distance between the atom pair where the potential is minimum. In the latter, q_i and q_j represent the partial atomic charges of the atom i and j . In both terms, r_{ij} represents the distance between the atom pair. CHARMM36 force field was used in all simulations presented in this thesis.

Non-bonded interactions are considered in terms of van der Waals and Coulomb potentials. Van der Waals attraction forces (also known as London dispersion forces) and repulsion forces are modelled using a 12-6 Lennard-Jones potential term whereas a Coulomb potential is used to compute electrostatic interactions. Force fields calculate electrostatic interactions using the constant, partial atomic charges assigned to all atom types unless otherwise stated. Non-bonded interactions, by definition, are computed for atom pairs separated by at least three bonds [110,111]. To calculate the Lennard-Jones potential between two different atom types, Lorentz-Berthelot combining rules are employed [111].

$$\epsilon_{ij} = \sqrt{\epsilon_i \epsilon_j} \qquad Rmin_{ij} = \frac{Rmin_i + Rmin_j}{2} \qquad (3)$$

Here, ϵ_{ij} and $Rmin_{ij}$ represent the energy and size parameters of the i th and j th atoms. The former is the well depth that can also be thought as a measure of how strongly the two atoms attract each other. The latter is the distance at which the interaction potential between the two atoms is minimum.

2.3. Enhanced Sampling Methods in Molecular Dynamics

Molecular dynamics has been a popular technique for structural and functional studies of biomolecular systems including protein folding [112], protein-protein interactions [113] and drug design [114]. The molecular dynamics technique, by itself, relies on the intrinsic sampling ability of the thermal motion of molecular systems at the temperature at which the simulation is run. Since biomolecular systems often possess a large number of degrees of freedom, and therefore complex energy landscapes, many biochemical processes involving these systems can only be accessible at long time scales (microseconds). The conformational transitions underlying such processes are often not observed during the microsecond timescales of molecular dynamics simulations [115]. Therefore, biomolecular systems with complex energy landscapes are generally studied using molecular dynamics combined with an enhanced sampling method. For example, a sufficient sampling of the relevant portion of the energy landscape of the system under investigation is needed to study ion permeation, and therefore the sampling of a molecular dynamics simulation, to study ion permeation, must be improved with an enhanced sampling method.

In Chapter 4, the ion permeation studies of Orai calcium channels were done by performing molecular dynamics simulations enhanced with umbrella sampling and the free energy profiles are generated using the weighted histogram analysis method (WHAM). Umbrella sampling was chosen among several methods because it is efficient and easy to implement [116,117]. Section 2.3.2 presents these two methods, umbrella sampling and WHAM, in detail. In Chapter 5, the free energy calculation for the loop connecting the transmembrane helix XII to the cytoplasmic C-terminal domain of the ProP transporter in solution was performed using the adaptive biasing force (ABF) method. The details of the ABF method are presented in Section 2.3.3.

2.3.1. Free Energy Calculations

Free energy calculations are crucial to grasp the physics behind almost every biochemical process, and are widely used in several research areas including protein folding, drug design and assembly of membrane proteins [115,118]. Several biochemical quantities, including binding, equilibrium constants, and solubilities, can be computed using the free energy of a system [118]. In particular, free energy can be useful for (1) understanding how likely it is for a system to choose a particular state; (2) predicting how a biochemical process will proceed; (3) probing the experimentally unavailable states of the system; and (4) understanding the biochemical process of interest at the atomic level [119,120].

In the canonical (NVT) ensemble, where the number of particles in the system (N), volume (V) and temperature (T) are kept constant, the free energy (F) of a system of N particles can be written as a function of the positions ($\vec{r}_N = \vec{r}_1, \vec{r}_2, \dots, \vec{r}_N$) and momenta ($\vec{p}_N = \vec{p}_1, \vec{p}_2, \dots, \vec{p}_N$) of all particles in the system:

$$F = -k_B T \ln \left(\frac{1}{N! h^{3N}} \iint e^{-H(\vec{r}^N, \vec{p}^N)/k_B T} d\vec{r}^N d\vec{p}^N \right) \quad (4)$$

Here, k_B and h are Boltzmann's and Planck's constants, respectively. h^{3N} is introduced as the factor of proportionality to retrieve the correct correspondence with the high-temperature quantum-mechanical prediction while the $N!$ factor is necessary for indistinguishable particles [121]. H represents the Hamiltonian, the total energy of the system in a given set of coordinates and momenta (\vec{r}^N, \vec{p}^N). In the isobaric-isothermal (NPT) ensemble, the thermodynamic potential is the Gibbs free energy (G) defined as:

$$G = F + PV = U + PV - TS \quad (5)$$

where P , $(U + PV)$ and S denote pressure, enthalpy and entropy, respectively. This distinction is not of importance since the different ensembles (NVT , NPT , $N\mu T$, etc.) are macroscopically equivalent for equilibrium states in the thermodynamic limit of N as the volume of the system is large ($V \rightarrow \infty$). For macroscopic systems, deviations from the thermodynamic limit are hence negligible because they scale as $\sim 1/\sqrt{N}$ [122]. In other words, the difference between F and G is mostly irrelevant, since biomolecular systems are not diluted [123].

The $6N$ -dimensional integral makes the calculation of the free energy of a system extremely difficult since this integrand is always positive, and its logarithm is a monotonically increasing function [120]. In practice, molecular dynamics-based methods are used for the computation of the free energy differences (ΔF) between two states of a system instead of the absolute free energy. For any biomolecular system, the free energy difference between two states of interest can be calculated from the probability of finding the molecular system of interest in different states over ensembles of atomic configurations [120]. Even though a molecular dynamics simulation can generate such ensembles for any biomolecular system, it must be combined with an enhanced sampling method due to the intrinsic difficulty of calculating the entropy. Internal energy and enthalpy can be estimated from unbiased molecular dynamics simulations relatively better compared to entropy because both are mostly contributed by low energy regions, whereas the estimation of entropy requires broader sampling of the configuration space [124]. After generating the simulation trajectory (i.e. a sequence of conformations of the biomolecular system), the free energy difference (ΔF_{AB}) can be estimated by simply counting the number of configurations in the corresponding states:

$$\Delta F_{AB} = -k_B T \log \frac{N_A}{N_B} \quad (6)$$

Here, N_A and N_B represent the count of how many times configuration A and B have been explored, respectively. A and B can also correspond to the different conformations of the same biomolecular system where the accessible conformational space is restricted in the desired regions using a set of constraints [119].

2.3.2. Umbrella Sampling and Weighted Histogram Analysis Method

Low energy regions can be sampled using unbiased molecular dynamics simulations (i.e. Newton's second law is employed without biasing the sampling). However, the configurational space might be problematic to sample even for simple systems. As mentioned earlier, molecular dynamics is biased to improve the sampling of the relevant regions of a configurational space. The enhanced sampling method is known as umbrella sampling when applied bias is a harmonic potential – because of its umbrella-like shape. In this method, the bias is used to accelerate the sampling of a reaction coordinate that reveals the molecular mechanism underlying the process of interest. A reaction coordinate, often referred to as a collective variable in molecular dynamics, is a geometric parameter such as the distance between atoms or groups of atoms, bond length or dihedral angle, and therefore depends on atomic coordinates.

The relevant region is defined in terms of a reaction coordinate (ξ), therefore can be written as a function of atomic coordinates, and divided into M individual windows, each being a molecular dynamics simulation combined with umbrella sampling. In each simulation (i.e. window), a bias potential (W) is added to the potential energy function of the biomolecular system in order to center the reaction coordinate at a specific value, known as the window center (ξ_{center}) [116]. The total of M windows must cover the range of the reaction coordinate that is relevant to the process of interest. The values that the reaction coordinate can take within the relevant range must be sampling efficiently in order to obtain a reasonable estimation of the free energy profile as a function of the reaction coordinate. For the window i , the bias potential can be written as follows:

$$W_i(\xi) = \frac{1}{2} k (\xi - \xi_{\text{center},i})^2 \quad (7)$$

Here, W_i represents the bias potential of the window i , added to the potential energy function (U) of the biomolecular system obtained using a force field. Also, k , ξ , and $\xi_{\text{center},i}$ denote the force constant, the instantaneous value of the reaction coordinate and the fixed value of the reaction coordinate (i.e. the center of the window i), respectively.

From each window, the normalized histogram of the reaction coordinate is computed. These histograms are, in fact, the biased probability distribution functions of the reaction coordinate

$\{\rho_{b,1}(\xi), \rho_{b,2}(\xi), \dots, \rho_{b,M}(\xi)\}$ [116,117]. Here, the subscript b represents the *biased* distribution while $\rho(\xi)$ and M denote the probability distribution of the reaction coordinate (ξ) and the number of windows covering the relevant range of this reaction coordinate.

The weighted histogram analysis method (WHAM) uses the biased probability distribution of the reaction coordinate ($\rho_{b,i}(\xi)$) to obtain the unbiased probability distribution of the reaction coordinate, $\rho_{u,i}(\xi)$ [123]:

$$\rho_{u,i}(\xi) = e^{\beta[W_i(\xi)-f_i]} \rho_{b,i}(\xi) \quad (8)$$

Here, f_i denotes the free energy emerging from the bias potential (W_i). The total unbiased distribution of the reaction coordinate, $\rho_o(\xi)$, can be computed as a linear combination of the unbiased probability distributions obtained from each window. Hence, this method requires a sufficient overlap between the histograms of the reaction coordinates from the consecutive windows [116,117].

$$\rho_o(\xi) = C \sum_{i=1}^M p_i(\xi) \rho_{b,i}(\xi) \quad (9)$$

Here, C and p_i represent the normalization constant and the weight, respectively. The summation of all weights from the individual windows has to be 1. These values are chosen in a way that the statistical error of the total unbiased probability distribution is minimized [117].

$$\frac{\partial(\sigma^2[\rho_o(\xi)])}{\partial p_i} = 0 \quad (10)$$

This condition allows the total unbiased probability distribution to be written in the following form:

$$\rho_o(\xi) = C \sum_{i=1}^M \frac{n_i}{\sum_{j=1}^M n_j e^{-\beta(W_j(\xi)-f_j)}} \rho_{b,i}(\xi) \quad (11)$$

where n_i denotes the length of the window i . The f_i values are assumed to be known, and therefore the WHAM method estimates them in a self-consistent manner [117]. The free energy as a function of the reaction coordinate can be estimated solving the following equation:

$$e^{-\beta f_k} = \int d\xi e^{-\beta W_k(\xi)} \rho_o(\xi) = C \int d\xi \frac{\sum_{i=1}^M n_i e^{-\beta W_k(\xi)}}{\sum_{j=1}^M n_j e^{-\beta [W_j(\xi) - f_j]}} \rho_{b,i}(\xi) \quad (12)$$

Since both sides of this equation involve the set of free energy parameters $\{f_k\}$, it needs to be solved iteratively. The solution starts with an initial set of guessed values for free energy parameters, $\{f_i^0\}$, and this set of guesses is used for computing the new set of guesses $\{f_i^1\}$. The iterative solution continues until the result is converged [117]. Thus, combining all the information coming from individual windows, WHAM constructs an optimal estimate of the unbiased distribution function of the reaction coordinate, and therefore the free energy as a function of this reaction coordinate.

In this thesis, umbrella sampling and WHAM are combined to generate free energy profiles of the translocation of ions through Orai calcium channels. To understand the gating mechanism and the selectivity of an ion channel, atomic details provided by unbiased molecular dynamics simulations might not be enough since the sampling of the conformational space of this system relies on the intrinsic dynamics of the system at the simulation temperature. The permeant ion might get stuck in a local free energy minimum and the thermal motion of the molecular systems might not be enough for the ion to overcome that barrier during the time of the simulation. However, understanding free energy change due to ion permeation requires sufficient sampling of the reaction coordinate – the position of the permeant ion along the pore axis. All the relevant values of this reaction coordinate need to be sampled very well in order to understand the change in free energy as a function of this parameter.

Figure 2.3 represents the necessary steps for modeling ion permeation through the permeation pathway of an ion channel. First, the reaction coordinate must be chosen. For ion permeation calculations using an enhanced molecular dynamics method like umbrella sampling, the reaction coordinate is often the position of the permeant ion along the pore axis (Figure 2.3A). Next, a relevant range of the reaction coordinate must be chosen. The permeant ion has to be sampled through the whole permeation pathway (Figure 2.3B). Then, individual molecular dynamics simulations are performed. In each simulation, the permeant ion is constrained at a specific position along the permeation pathway by a harmonic bias potential. The idea is to force the permeant ion using a harmonic bias potential so that it samples a specific portion of the ion pore at each window. The simulation trajectories are then used for computing the histogram of the

permeant ion's position, known as the biased probability distributions of the reaction coordinate. Finally, the weighted histogram analysis method estimates the unbiased probability distribution of the reaction coordinate and optimizes the free energy estimation by overlapping the free energy parameters calculated for each window. The result is the free energy profile along the ion position, describing the average forces acting on the permeant ion in the system.

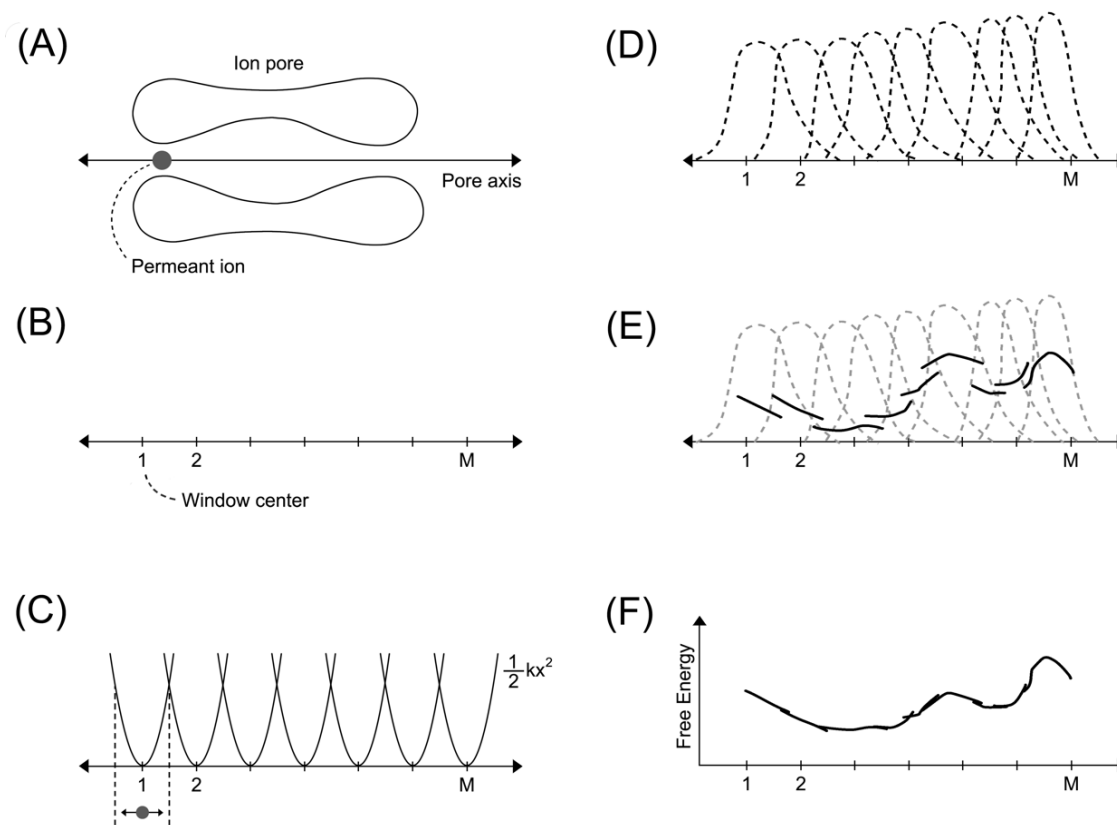


Figure 2.3. The diagram of the steps necessary for the calculation of the free energy profile of ion translocation using umbrella sampling and WHAM. (A) Step 1: The choice of a reaction coordinate. (B) Step 2: Dividing the relevant range of the reaction coordinate into M windows. (C) Step 3: The individual bias potentials centered at each defined window center. (D) Step 4: The bias probability distributions of the reaction coordinate. (E) Step 5: Generation of free energy parameters by WHAM. (F) Step 6: A sufficient overlap of the biased probability distribution functions is necessary for the estimation of free energy.

2.3.3. Adaptive Biasing Force Method

The adaptive biasing force (ABF) method is an alternative to the umbrella sampling technique and is used to estimate the free energy profile of a reaction coordinate. This method enhances the sampling of a reaction coordinate adaptively; the mean force along the reaction coordinate is

computed and canceled out by an equal and opposite biasing force. This biasing force allows the system to escape from the corresponding free energy well [125,126]. It fundamentally turns the dynamics of the reaction coordinate into a random walk with zero mean force. Only the fluctuating part of the instantaneous force is exerted along the reaction coordinate [126]. Therefore, the adaptive biasing force overcomes the roughness of the system's free energy and samples the free energy surface along the reaction coordinate uniformly [125,126].

The ABF method assumes the reaction coordinate (ξ) as fully unconstrained. It continuously explores the complete range of the reaction coordinate, as set by the user, throughout the simulation. This range is divided into small bins of width ($\Delta\xi$). The instantaneous force exerted on the reaction coordinate is sampled in the different bins until a threshold of the number of samples, also set by the user, is obtained. Then the ABF algorithm applies the adaptive biasing force on the reaction coordinate. The free energy along the reaction coordinate ($F(\xi)$) is calculated from the instantaneous force exerted along the reaction coordinate ($f(\xi)$).

$$\langle f(\xi) \rangle = - \frac{dF(\xi)}{d\xi} \quad (13)$$

Here, the brackets $\langle \rangle$ denote the mean average of the instantaneous force generated over the course of the simulation [127]. The convergence of this calculation is significantly affected by the coupling of the reaction coordinate to other degrees of freedom. In the case of slowly relaxing degrees of freedom, the user should set a large threshold for the number of samples to be accumulated before applying the adaptive biasing force onto the reaction coordinate [126].

In this work, the ABF method is utilized to sample the accessible conformations of the loop of the ProP transporter connecting the cytoplasmic domain to the transmembrane helix XII. The ABF method was particularly chosen since it is easy to set up and converges very well for systems in which the reaction coordinate is not coupled to a slowly relaxing degree of freedom.

Chapter 3. Structural dynamics of Orai channels

3.1. Abstract

Depletion of calcium (Ca^{2+}) stores in the endoplasmic reticulum causes Ca^{2+} influx in many non-excitable cells through the pores formed by Orai proteins. These channels generate highly selective Ca^{2+} currents with extremely low permeation rates. Although studies in the literature suggest that the active form of Orai channels could be either tetrameric or hexameric, the focus in the field shifted towards the hexameric assembly after the *Drosophila melanogaster* Orai protein was crystallized as a hexamer. Several studies have identified mutations within the transmembrane domains of Orai channels that can alter channel gating and selectivity, however both mechanisms have not been fully understood yet. A recent hypothesis on the gating mechanism of the Orai channel is based on the rotation of pore-forming helices as a result of the gating signal by STIM proteins relayed along the contacts within the channel's other transmembrane helices. Combined with the unusual features of the Orai pore, existing data in the literature points out the importance of residue-residue contacts and pore dynamics in understanding the function, selectivity and activation of these channels. Here, we perform molecular dynamics simulations of the model structures of the hexameric and tetrameric Orai channels in the closed and open conformations. The open conformation is induced by a rotation of the pore-forming helices. We examine the residue-residue contacts and the dynamics of the pore-forming helices in order to compare the two multimeric states of Orai proteins. Our results demonstrate that, in the closed conformation, the tetrameric Orai channel retains most of the contacts that exist in the hexamer. The rotation of pore-forming helices increases the contacts between the adjacent subunits in the tetrameric channel whereas it slightly decreases the number of stable contacts in the hexameric channel. The most pronounced alteration caused by the helix rotation is the increase in pore hydration. Overall, the study suggests that the hexamer pore — more hydrated compared to the tetrameric pore— might act as a better mediator for permeant Ca^{2+} ions since the pore is wide enough to permeate Ca^{2+} ions with little or no perturbation to their first hydration shells.

3.2. Introduction

In non-excitabile cells, Orai proteins form the pore subunits of calcium-release activated calcium (CRAC) channels that open in response to depletion in the calcium (Ca^{2+}) stores of the endoplasmic reticulum. Orai channels are gated by STIM proteins – the Ca^{2+} sensors of the endoplasmic reticulum. STIM and Orai proteins are dynamically coupled with each other [36,68,128]: STIM proteins not only multimerize Orai proteins but also open the Orai pore and alter its Ca^{2+} selectivity, whereas Orai proteins form the permeation pathway for Ca^{2+} ions. Orai channels contribute to several cellular functions including muscle contraction, immune activation and proliferation [28,129]. Therefore, mutations in Orai channels are implicated in autoimmunity, skin and tooth defects, severe immunodeficiency, thrombocytopenia and tubular aggregate myopathy [73,76,130].

The crystal structures of the *Drosophila melanogaster* (*D. melanogaster*) Orai protein [11,57] as well as mutagenesis studies [55,67,68] provided strong evidence that Orai proteins, in their active form, are hexameric channels organized as a trimer of dimers. However, the possibility of different existing multimeric states should be kept in mind [131], since several studies have identified a tetrameric assembly of Orai proteins as the active, calcium-selective Orai channel [42–44,50,52,53,132,133]. In one study by Cai et al., store-operated Ca^{2+} entries were detected using different Orai1 concatemers, including dimers, tetramers and hexamers [55]. These concatemers are believed to assemble into larger units and reproduce the architecture of the functional Orai channel. Cai et al. replaced specific subunits in Orai1 tetramers with a pore-inactive mutation E106A (corresponding to E178A in *D. melanogaster* Orai) and concluded that the Orai channel function is recovered from the assembly of multiple N-terminal dimers [55]. Most of other experimental studies simply shifted their focus from tetramer to hexamer after the publication of the crystal structure of the *D. melanogaster* Orai protein. None of the computational studies addressed the presence of different multimeric states of Orai channels.

The Orai protein is composed of four transmembrane helices (TM1 to TM4) and an extension helix named TM4-extension (see Figure 1.3). The crystal structure of *D. melanogaster* Orai channel revealed a hexameric assembly of Orai proteins. In this channel, a ring of six TM1 helices creates a central ion pore. A second layer of transmembrane helices are formed by the TM2/3 helices surrounding the pore-forming TM1 helices. Then the TM4 helices, building the

outmost layer, bring in a three-fold symmetry to the hexameric Orai channel: the TM4-extension helix of an Orai protein (subunit A) extends toward the cytosol whereas in the next Orai protein (subunit B) the TM4-extension helix wraps the adjacent Orai subunit (see Figure 1.3 C and D). At the extracellular side, the pore begins with six glutamate residues (E178) from the TM1 helices. These residues are named the selectivity filter as they are thought to be responsible for the calcium selectivity of Orai channels [11]. Following the selectivity filter, a hydrophobic part that is lined by the residues V174, F171 and L167 extends the pore for three helical turns toward the cytosol (see Figure 1.3E). This hydrophobic part of the Orai channel is likely to play a key role in lowering the single-channel calcium flux ($<10^4$ ions per second) [131]. Interestingly, the hydrophobic part is followed by another three helical turns lined with three basic residues. Here, the residues K163, K159 and R155 suggest a local concentration of positive charges within this cation channel. The basic part of the Orai channel is likely to be stabilized by anions from the cytoplasm [11].

The crystal structure of the *D. melanogaster* Orai protein provides a starting point for molecular modeling studies that can offer atomic-level insights on the structural dynamics of Orai channels. It is vital to understand the dynamics of these channels in terms of residue-residue contacts since mutagenesis studies showed that mutations in the TM2/TM3 helices alter the gating of Orai channels [67,68,134]. From these studies, the following hypothesis on the gating mechanism emerged: STIM proteins bind to the cytoplasmic part of the Orai channel and generate a gating signal that is relayed along the non-pore-lining residues to the pore [67,68,134,135]. The mutations in the pore-forming TM1 helix also affect the gating and ion selectivity of these channels. For example, E178A [136] and K163W (R91W in *H. sapiens* Orai1) [53] mutants were identified as non-conducting channels, while V174A (V102A in *H. sapiens* Orai1) [137] and F171Y (F99Y in *H. sapiens* Orai1) [67] mutations caused the channel to be constitutively conducting. Recent studies [36,67,68] suggested that the binding of STIM opens the Orai pore by rotating the pore-forming helices of the channel. Taken together, the current studies in the literature do not provide direct evidence of why an Orai tetramer would not function; how the structural dynamics of Orai hexamers are different compared to Orai tetramers; and if the rotation of pore-helices would alter the dynamics of these channels at atomic detail.

The present set of molecular dynamics simulations probes the structural dynamics of the hexameric and tetrameric assemblies of Orai proteins since they are the most widely proposed multimeric states for the active form of the Orai channel. In order to compare the structural dynamics of these channels, we first used homology modeling and built a model structure of the Orai tetramer based on the hexameric Orai crystal. In addition, we generated the hexameric and tetrameric Orai model structures with rotated pore-forming helices in order to (1) investigate how helix rotation affects the structural dynamics of both Orai multimers and (2) whether helix rotation can open the Orai pores. We performed molecular dynamics of both Orai multimers in the closed state (based on the Orai crystal structure) and open state (with rotated pore-forming helices) to compare the structural differences between these multimers at atomic resolution. To compare these multimers, residue-residue contacts and pore structures were studied since both are crucial for understanding the function of these channels: permeating Ca^{2+} ions into the cell with extremely high selectivity and extremely low permeation rate.

3.3. Computational Details

3.3.1. Modeling of the Orai Channels

We built a model structure of the Orai hexamer using the crystal structure of the *Drosophila melanogaster* Orai protein (Protein Data Bank ID: 4HKR) [11] as a template. MODELLER [97] is used to add the missing side chains and loops connecting the transmembrane helices that were unresolved in the crystal structure. A homology model of the Orai tetramer is then generated by using the model structure of the Orai hexamer as a template. More specifically, we built the tetramer structure by transforming the cylindrical coordinates (r, θ, z) of four adjacent units of the hexamer to $(r, 6\theta/4, z)$, resulting in a fourfold symmetry in the TM1-TM4 helices and twofold symmetry in the TM4-extension helices. The open conformations of the Orai hexamer and tetramer are built by rotating the pore-forming, TM1 helices (formed by residues W144 to E178) of the initial model structures of hexameric and tetrameric Orai assemblies. Each TM1 helix was rotated around the z-axis (the pore axis) by 20° in the counter clockwise direction.

3.3.2. Simulation Setup

In all Orai channels, H206 residues were protonated at their ϵ nitrogen atoms and E262 residues were neutralized. The default protonation states were kept for the other amino acids. Residues

between 133 and 306 were included in the system to exclude the TM4-extension helices that were expected to undergo large conformational changes [11]. The orientation of each Orai channel was aligned with respect to the membrane surface using the 4HKR entry in the Orientations of Proteins in Membranes (OPM) database [138]. Then, each channel was embedded in a pre-equilibrated, explicit 1-palmitoyl-2-oleoyl-phosphatidylcholine (POPC) membrane and solvated with a 150 mM NaCl solution using CHARMM-GUI [139,140].

The resulting simulation box for the closed Orai hexamer included 133 and 125 lipid molecules in the top and bottom leaflets respectively, and was solvated by 24212 water molecules, 75 sodium ions and 81 chloride ions. The total number of atoms in this system was 124110, contained in a hexagonal simulation box ($a = b = 117 \text{ \AA}$ and $c = 112 \text{ \AA}$). The closed Orai tetramer consisted of 128 lipid molecules in the top leaflet and 121 in the bottom, and was solvated by 20896 water molecules, 66 sodium ions and 70 chloride ions. The total number of atoms in the tetrameric Orai system was 107354, in a rectangular simulation box with a dimension of $106 \text{ \AA} \times 106 \text{ \AA} \times 107 \text{ \AA}$. The extra chloride anions were added to neutralize each system.

The open Orai hexamer system contained a total of 140261 atoms in a hexagonal simulation box ($a = b = 117 \text{ \AA}$ and $c = 127 \text{ \AA}$), which included 133 lipid molecules in the top leaflet, 125 lipid molecules in the bottom leaflet, 29593 water molecules, 79 sodium ions and 85 chloride ions. Finally, the rectangular simulation box for the open Orai tetramer channel was $105 \text{ \AA} \times 105 \text{ \AA} \times 122 \text{ \AA}$ and included 128 lipids in the top leaflet, 121 lipids in the bottom leaflet, 26081 water molecules, 70 sodium ions and 74 chloride ions. The resulting simulation system was composed of 122917 atoms.

We used the CHARMM36 force field [111] and TIP3P water model [141] to describe the intra- and inter-molecular interactions in the simulation systems. The temperature was kept constant at 303.15 K using Langevin dynamics, with a coupling coefficient of 1 ps^{-1} , and the pressure was also kept constant at 1 atm using a Nosé-Hoover Langevin piston with a period of 50 fs and a decay of 25 fs [108,109]. All bonds involving hydrogen atoms were constrained using the SHAKE/RATTLE algorithm [142]. Nonbonded interactions were calculated using particle mesh

Ewald [143] and the recommended CHARMM cut-off scheme[144]. The simulations were run using NAMD 2.9 [145].

The simulation systems were relaxed in the NVT ensemble for 0.67 ns by using a modified version of equilibration steps suggested by Jo and coworkers [140]. In addition, we added (1) the harmonic restraints on the dihedral angles of residues 144 to 178 (with a force constant of 500 kcal/mol) and (2) the restraints on the bond distances of atoms involved in forming hydrogen bonds found in the initial structure to their initial values (with a force constant of 1 kcal/mol/Å²). The list of hydrogen bonds constrained can be found in Table 3.1.

Table 3.1. Hydrogen bonds constrained during the equilibration phase

Residue 1	Atom 1	Residue 2	Atom 2
E262	OE2	T199	OG1
H206	ND1	S165	OG
W248	NE1	S161	OG
C267	SG	T200	OG1

After the relaxation in the NVT ensemble, we continued to equilibrate the systems, in the NPT ensemble, for 6 ns with the dihedral angle and hydrogen bond constraints. The harmonic restraints on the bond distance of the atoms forming hydrogen bonds were removed after 2 ns, and the harmonic restraints on the dihedral angles of TM1 residues (144 to 178) after 6 ns. Then, the closed Orai hexamer and tetramer systems were simulated for an additional 1000 ns in the NPT ensemble, whereas the open Orai hexamer and tetramer channels were simulated for 500 ns without any constraints. Only the second half of the production steps (500 ns for the closed Orai channels and 250 ns of the open Orai channels) were analyzed. The analysis involved several programs: HOLE [146], the Bio3D [147] package in R, the MDAnalysis [148,149] package in Python, and VMD [150]. The snapshots of the structures of Orai channels were taken using VMD; the graphs were plotted in R, mostly with the ggplot2 package [151].

3.4. Results and Discussion

3.4.1. Structural Stability of the Closed and Open Orai Channels

The model structures of the Orai hexamer and tetramer, after being embedded in a pure 1-palmitoyl-2-oleoyl-phosphatidylcholine (POPC) bilayer and solvated in a 150 mM NaCl solution, were relaxed for ~7 ns and simulated without any constraints for 1000 ns. These models are built based on the crystal structure of the *D. melanogaster* Orai protein (PDB ID: 4HKR) [11], and therefore their pores are presumed to be in a closed state. Figure 3.1A and 3.1B show the closed hexameric and tetrameric Orai channels. The root-mean-square deviation (RMSD) of backbone atoms in the transmembrane helices can be used as a measure of structural integrity. The RMSD of the backbone atoms was 2.4 Å for the closed hexamer and 3.9 Å for the closed tetramer. For the hexamer, the RMSD was calculated with respect to the crystal structure, and for the tetramer it was calculated with respect to the initial homology model. The higher RMSD values for the tetramers reflect the fact that the radius of the TM1 helix bundle contracts by about 1.5 Å during equilibration. The transmembrane α -helices remain stable in all simulation systems.

3.4.2. Contacts within the Closed Orai Channels

To examine the packing of helices in the closed Orai multimers, contacts between the transmembrane domains were calculated: side-chain contacts, hydrogen bonds and salt bridges. These contacts are important to examine not only for analyzing the helical packing of the Orai multimers, but also a measure of their functionality, since the contacts between the transmembrane domains were suggested to be implicated in Orai gating [64,68]. First, we calculated the residue-residue contacts by taking the side-chain atoms into account. Since our aim was to compare the Orai hexamers and tetramers, an average contact probability map per dimer was computed for each multimer, providing an opportunity of direct comparison (see Figure 3.2). A contact probability map is calculated as the sum of contact matrices divided by the number of snapshots taken from the simulation trajectory. It is composed of all the possible residue pairs and each position (i, j) represents the fraction of simulation time during which the corresponding pair of residues i and j is in contact. A residue pair is assumed to be in contact if the distance between any non-hydrogen side-chain atoms is shorter than 5 Å. At each frame, the position (i, j) of the contact matrix takes the value of 1 if the residues i and j form a contact, or 0

if they are not in contact. Finally, the contact matrices for all simulation frames are summed up and divided by the number of frames in order to generate the contact probability maps.

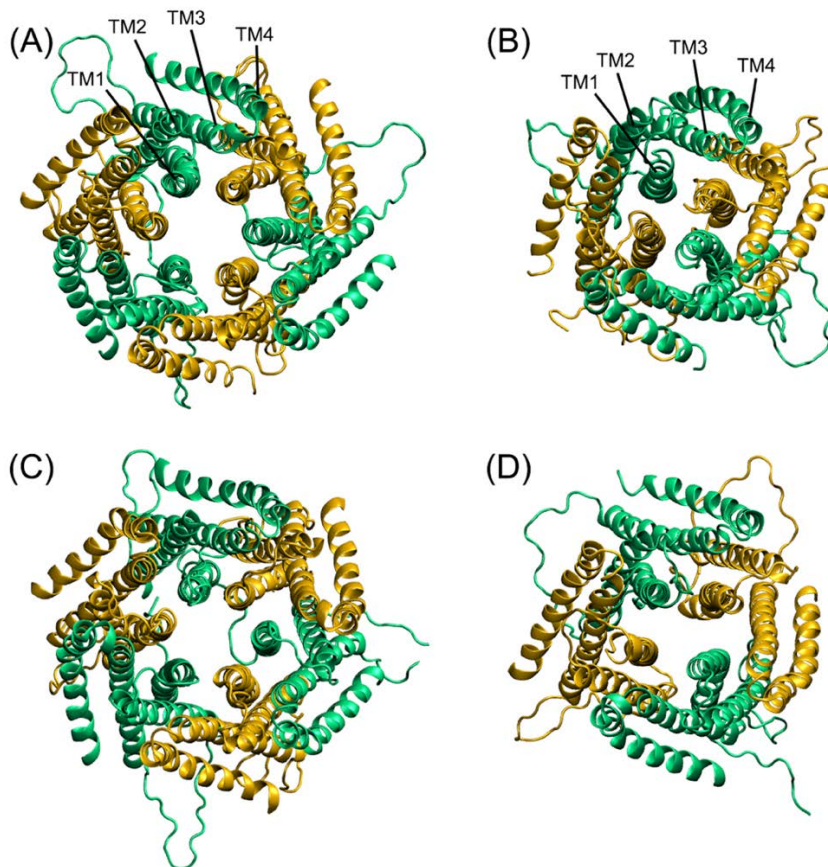


Figure 3.1. Top view of the (A) closed hexamer, (B) closed tetramer, (C) open hexamer and (D) open tetramer channels at the end of 7 ns. The subunits A and B of each dimer are represented in yellow and green, respectively. The hexamer and tetramer channels possess a sixfold and fourfold symmetry, since they only include the helices TM1 to TM4 from each subunit, not the TM4-extension helices. These helices are excluded from our models since they are expected to undergo large conformational changes during gating [11,152] and it would be difficult to sample their conformations using molecular dynamics simulations.

Throughout the simulations, the closed hexamer maintains a total of 676 ± 6 intra- and inter-monomer contacts per monomer (mean \pm standard deviation) and the closed tetramer 639 ± 6 contacts. These include all instantaneous contacts, counted from all individual monomers, averaged through the whole simulation trajectory without a cut-off for the probability of contact. Then, we focused on analyzing a subset of these contacts that, on average, are present in all the monomers and are formed for at least 25% of the simulation time – significant contacts. Figure

3.2 shows the contact probability maps of these resulting contacts, reduced to a dimer of the Orai hexamer and of the tetramer. In these maps, the diagonal quadrants represent intra-monomer contacts – formed by residues belonging to the same monomer – whereas the off-diagonal quadrants show inter-monomer contacts – formed by residues belonging to two adjacent monomers.

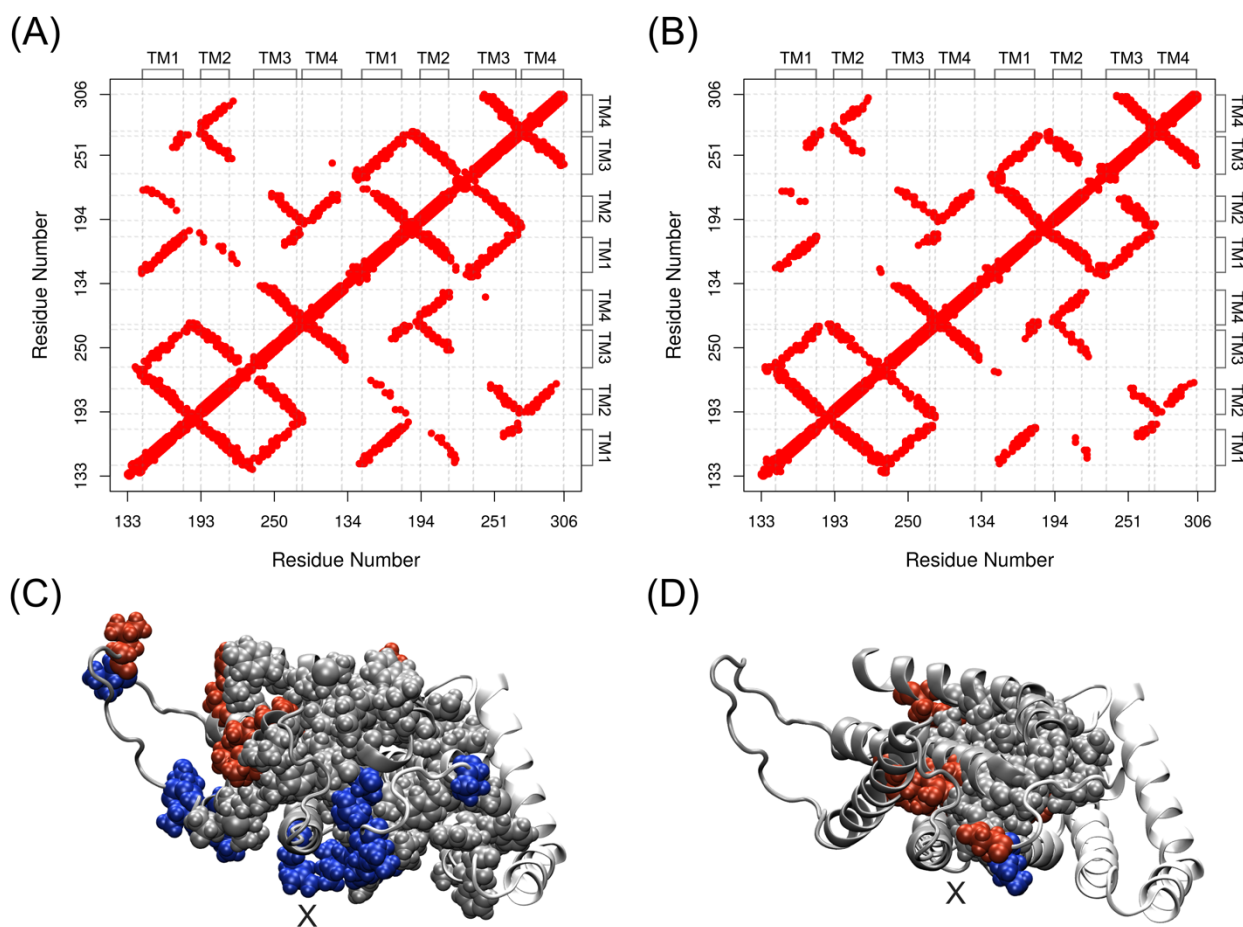


Figure 3.2. Contact probability maps of the closed (A) hexamer and (B) tetramer Orai channels. These maps were averaged through the last 500 ns of the production trajectories by using one frame for every 0.01 ns. Then the maps were reduced to contact frequency maps of a dimer averaged over possible pairs of subunits from the Orai channels. Both axes show the residue numbers and the labels specifying the residues corresponding to the TM1-TM4 helices. The cut-off probability was set to 25% of the simulation time. The top view of a representative dimer shows the residues involved in forming the (C) intra-monomer and (D) inter-monomer contacts. The residues forming contacts in both Orai multimers are colored in gray whereas the residues forming contacts only in the hexamer or only in the tetramer are colored in red or blue, respectively. The “X” symbol represents the permeation axis.

In both multimers, most of the stable contacts are intra-monomer contacts. Among these contacts, the ones formed by the residues from the same transmembrane helices only point out the structural integrity of an individual helix. We deemed them not relevant for evaluating the helical packing and excluded them from further analysis. The same applies to the contacts involving the residues from the loops connecting the transmembrane helices. Therefore, after these exclusions, we identified that the hexamer and tetramer possess, respectively, an average of 139 and 137 significant intra-monomer contacts per monomer that have at least 25% probability of formation (see Table 3.2). The tetramer has more contacts located between TM1-TM2 and TM1-TM3 than the hexamer. Conversely, in the TM2-TM3 and TM3-TM4 regions, the hexamer has more stable contacts than the tetramer. The second layer TM helices of the tetramer forms more intra-monomer contacts with the pore-forming TM1 helices, while in the hexamer, the second layer of helices (TM2/TM3 ring) maintains more contacts with the outer TM4 helices compared to those found in the tetramer. The most significant difference is in the TM2-TM3 contacts; the hexamer possesses more intra-monomer contacts within the second layer of helices. The overall number of intra-monomer contacts per monomer in both multimers is comparable. In addition, TM2 and TM3 helices of the tetramer are slightly more tilted than those of the Orai hexamer. On one hand, the hexamer has an average tilt angle (with respect to the membrane normal vector) of 21° for TM2 and of 26° for TM3. Both of these values have a standard deviation of 7° throughout the simulation. On the other hand, the tilt angle was $29^\circ \pm 8^\circ$ for TM2 and $30^\circ \pm 8^\circ$ for TM3 in the tetramer.

Table 3.2. Significant intra-monomer contacts per monomer (inter-monomer contacts per interface) in the closed Orai multimers

Region	Closed hexamer		Closed tetramer	
	Intra-monomer	Inter-monomer	Intra-monomer	Inter-monomer
TM1-TM1	Excluded	54	Excluded	38
TM1-TM2	37	9	42	3
TM1-TM3	27	14	32	13
TM2-TM3	33	23	25	18
TM2-TM4	0	22	0	23
TM3-TM4	42	0	38	0
Total	139	122	137	95

In Figure 3.2, the off-diagonal quadrants of the contact probability maps show 216 significant inter-monomer contacts (>25% probability) maintained by the hexamer and 164 by the tetramer throughout the simulations. Among them, 122 contacts are formed by the residues belong to the transmembrane alpha helices in the hexamer and 95 of them in the tetramer (see Table 3.2). These contacts are formed by residues located in the TM1-TM1, TM1-TM2, TM1-TM3, TM2-TM3 and TM2-TM4 interfaces (see Figure 3.2). As done for the intra-monomer contacts, the inter-monomer contacts are calculated as the average contacts for all possible helix-helix combinations. For example, TM1-TM2 inter-monomer contacts include the contacts between the TM1 helix from the subunit A and the TM2 helix from the subunit B as well as the contacts between the TM2 from the subunit A and TM1 from the subunit B. As opposed to comparable number of total intra-monomer contacts found in both multimers, the average number of inter-monomer contacts per interface is different. The Orai hexamer maintains more stable contacts in the TM1-TM1, TM1-TM2, TM1-TM3, and TM2-TM3 interfaces, while the Orai tetramer preserves one more stable contact in the TM2-TM4 interfaces. The closed tetramer forms fewer and more short-lived inter-monomer contacts in the TM1-TM2/3 helices in which its average number of intra-monomer contacts is more compared to the closed hexamer. Regardless of the multimeric state, TM3-TM4 helices of Orai proteins form stable intra-monomer contacts yet no inter-monomer contacts, while TM2-TM4 helices maintain stable inter-monomer contacts and no intra-monomer contacts. This indicates that, while the total number and probability vary, both multimers possess significant contacts between the same helices.

As a more specific measure of contact, we use hydrogen bonds: weak electrostatic interactions between a proton in one residue (donor) and an electronegative atom in the other (acceptor). We set the distance cut-off to 3.0 Å between the acceptor and donor atoms, and the angle cut-off to 120° between the atoms forming a hydrogen bond. The hydrogen bonds formed within the residues are excluded in order to examine the communication between residues. The calculation includes the backbone-to-backbone, backbone-to-sidechain and sidechain-to-sidechain hydrogen bonds between a residue pair. Throughout the simulations, the closed hexamer maintains an average of 226 (with a standard deviation of 3) hydrogen bonds per monomer while the closed tetramer preserves 220 (with a standard deviation of 4) hydrogen bonds per monomer.

Salt bridges – electrostatic contacts between oppositely charged residues – were also analyzed, since TM1 and TM3 helices include acidic and basic residues that could potentially interact. We first identified the salt bridges using a distance cut-off of 5.0 Å between the atoms capable of forming a salt bridge and then we calculated the fraction of simulation time the distance between these atoms being smaller than 5.0 Å – the probability of formation for each identified salt bridge. While calculating the probability of formation, the number of monomers was taken into account. If a salt bridge is observed, with a probability of 1, only in three monomers of the Orai hexamer, the probability of formation of that salt bridge is 0.5.

The hexamer maintains ten intra-monomer salt bridges (see Figure 3.3A). However, half of these interactions have low probabilities and occur in less than three monomers. The strongest intra-monomer salt bridges are found between the lysine residues of TM1 (K150 and K157) and the glutamate residues of TM3 (E238 and E245). These interactions are found in all six monomers of the hexamer, with short average distances (≤ 5 Å) throughout the simulation, pointing out at symmetric contacts within the channel subunits. The residues K157-E245 also form a salt bridge in our initial model based on the crystal structure and therefore likely to be formed in the crystal structure. As it is, these salt bridges are not present in the crystal structure; since the resolution of the crystal structure is low (3.35 Å) [11], the side chains of some residues, including K157, are not resolved.

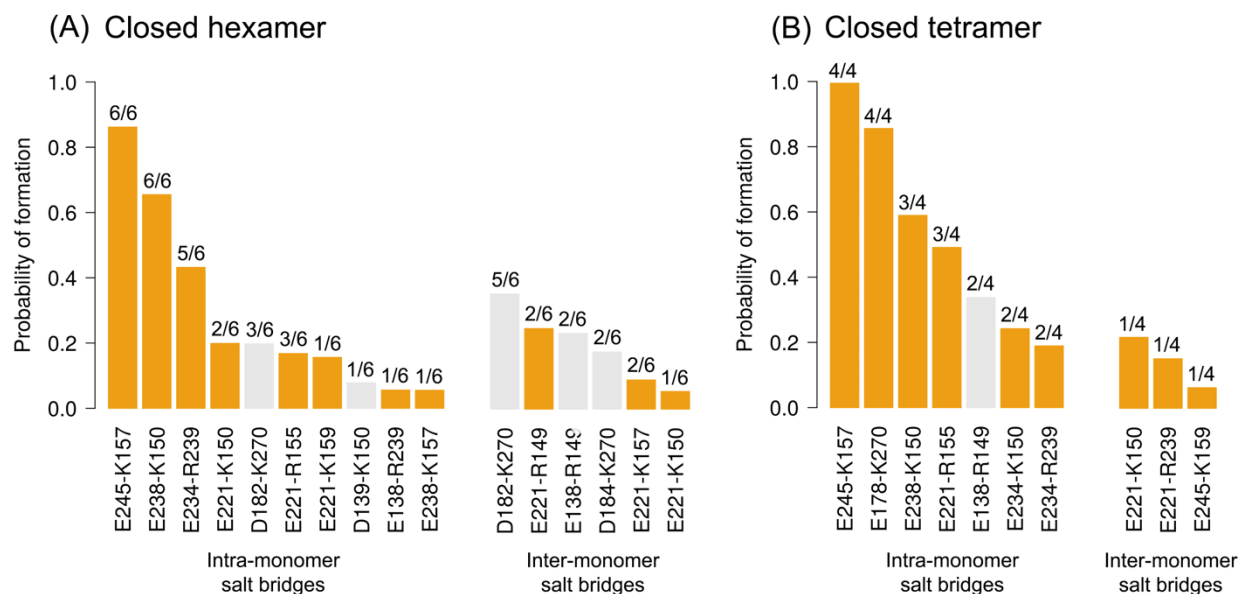


Figure 3.3. Salt bridges of the closed (A) hexameric and (B) tetrameric assemblies of Orai proteins. The probability of formation was calculated the fraction of simulation time during which the length of the salt bridge is ≤ 5 Å. The analysis was done using the last 500 ns of the production trajectories of the closed Orai multimers. The gray bars denote salt bridges involving at least one loop residue whereas the orange bars represent the salt bridges formed by residues from the transmembrane helices. The number, given for each bar, shows the number of occurrences of the salt bridges out of six monomers of the hexamer channel and out of four monomers of the tetramer channel.

The tetramer forms seven intra-monomer salt bridges throughout the simulation (see Figure 3.3B). Only one of these interactions occurs between a loop residue and a TM1 residue, the rest is formed between TM1-TM3 helices. Among the intra-monomer salt bridges, E245-K157 is the strongest in both structures and E238-K150 shows comparable strength (around 60%). These symmetric and frequent salt bridges between TM1 and TM3 helices of the tetramer seem to cause TM3 helices to have slightly larger tilt angles compared to those in the hexamer. As a result, the tetramer maintains two intra-monomer salt bridges between TM1-TM3 helices: E178-K270 and E211-R155 that are not present in the hexamer. The salt bridge between E178-K270, consistently formed in all monomers of the tetramer, is particularly interesting since it involves the selectivity filter residue (E178). A salt bridge involving the side chains of the selectivity filter could reduce the binding affinity to Ca^{2+} ions. The tetramer also has more hydrophobic contacts between TM1-TM3 compared to the hexamer (see Table 3.2). Instead, the TM3 helices of the hexamer maintain an intra-monomer salt bridge within themselves (between E234-R239) which are much weaker in the tetramer.

Both closed channels maintain three inter-monomer salt bridges formed by residues from the same transmembrane helices (TM1-TM3), excluding the ones involving loop residues. The tetramer has a salt bridge between TM3-TM3 helices from adjacent monomers, whereas the other two are formed between TM1-TM3 in both multimers. These stable inter-monomer salt bridges occur in one monomer pair in the tetramer, while two of them were formed between two monomer-monomer pairs in the hexamer (see Figure 3.3). Nevertheless, neither of the multimers maintains these interactions between all possible monomer pairs. In addition to these salt bridges, the closed hexamer has inter-monomer salt bridges between the loop residues (E138, D182 and D184) and TM1/TM3 residues among which the most frequent one is formed by the residues D182 and K270. Throughout the simulation, there were instances where a salt bridge between E178-K270 is formed. However, this instantaneous interaction results in an average distance that is larger than 8 Å throughout the simulation. This indicates that the E178 residues are likely to interact with salt cations in the hexamer since K270 residues form salt bridges with D182 residues more frequently.

3.4.3. Pore Structures of the Closed Orai Channels

In addition to residue-residue contacts, the structure of the Orai pore is crucial in terms of the channel function. Figure 3.4A shows the number densities of salt ions and water within a radial distance of 10 Å from the pore center. The E178 residues in the hexamer create a local concentration of sodium ions at the pore entrance. However, there are fewer sodium ions at the extracellular mouth of the tetrameric pore. In the extracellular half of the pore ($0 \text{ \AA} < z < 25 \text{ \AA}$) within a radial distance of 10 Å from the pore center, the hexamer has 5.7 ± 0.83 (mean \pm standard deviation) sodium ions throughout the simulations, while the tetramer has 2.2 ± 0.72 . This is expected considering the presence of salt bridges between E178 and K270 residues in the tetramer. Since the E178-K270 salt bridge is frequently formed in the tetramer, the sodium affinity is weaker and contributed mostly by the loop residues Q180, D182 and D184.

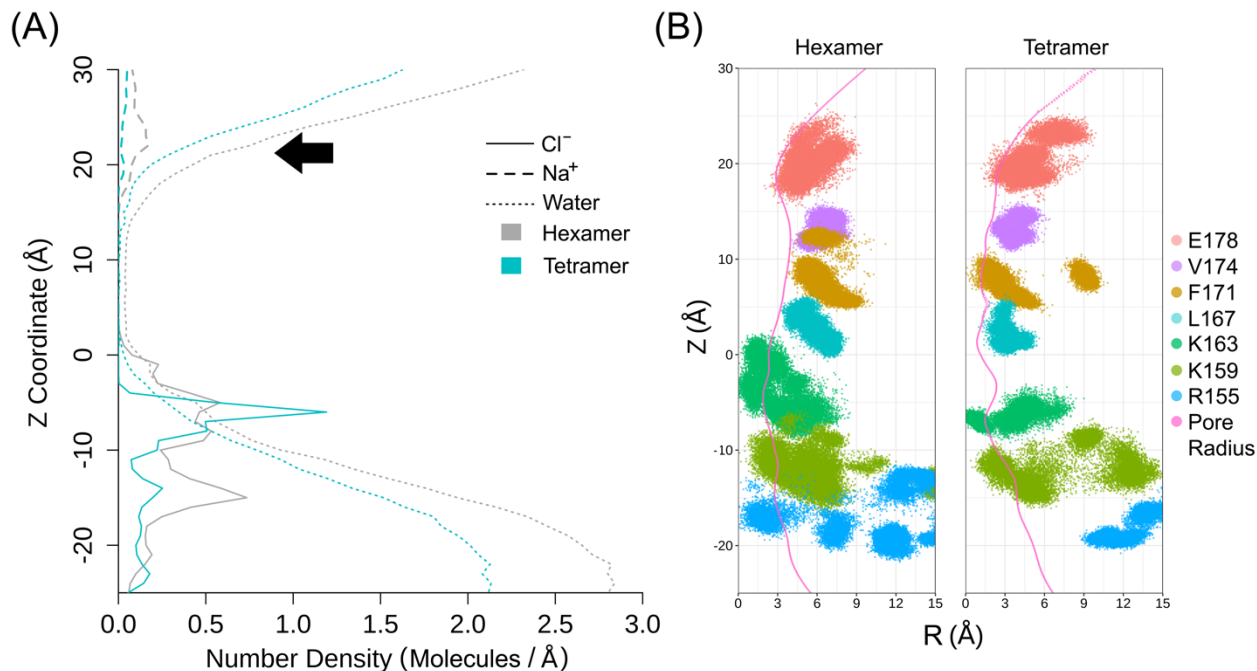


Figure 3.4. (A) Density profiles of salt ions (Cl^- and Na^+) and water molecules along the pores of the closed Orai multimers. The number density was calculated as the number of molecules within a cylindrical slice along the pore axis (of radius 10 \AA and height 1 \AA). The black arrow shows the Ca^{2+} position found in the crystal structure of Orai mutant, K163W [11]. (B) Distribution of the geometric center of the sidechain atoms of the pore-lining residues E178 (CD, OE1 and OE2 atoms), V174 (side-chain heavy atoms), F171 (CE2, CG and CZ atoms), L167 (side-chain heavy atoms), K163 and K159 (NZ atoms), R155 (NE, NH1 and NH2 atoms) and the average value of the pore radius along the pore axis in the hexamer and tetramer channels. The z coordinate is along the pore axis, with $z = 0$ \AA corresponding to the center of the lipid bilayer. Analysis was done using the last 500 ns of the production trajectories.

In both channels, the basic part of the pore attracts chloride ions. In the cytoplasmic part of the pore ($-25 \text{\AA} < z < 0 \text{\AA}$) within a radial distance of 10 \AA from the pore center, the average number of chloride ions is 12.2 (with a standard deviation of ± 0.91) for the hexamer and 7.3 ± 0.75 for the tetramer throughout the simulations. In the case of hexamer, these anions seem to be more fluctuational, interacting with the side-chains of basic residues which sampled a larger area within the pore (see Figure 3.4B). The density profile of chloride ions in the tetrameric pore, on the other hand, is more pronounced; they interact strongly with the K163 residues, therefore causing these residues to stay around $z = -5 \text{\AA}$ throughout the simulation. In three monomers of the tetramer channel, the R155 side-chains adopted a conformation pointing away from the pore, forming an intra-monomer salt bridge with the E221 residue from the TM3 helix and hence

spanning a smaller area within the pore. As a result, the tetrameric pore shows a lower density of chloride ions at $z = -15 \text{ \AA}$ in comparison to the hexamer channel.

Figure 3.4 shows that the tetramer channel creates a tighter packing in the hydrophobic part of the pore, causing a pore radius that is smaller compared to that of the hexamer channel. The hexameric channel possesses a few water molecules within the hydrophobic part of its pore. Yet, no spontaneous translocation of any ion was observed through the simulation, implying that the hydrophobic part of the hexameric pore still creates an energy barrier against ion permeation. In the case of the closed tetramer, the pore does not have water molecules in its hydrophobic part. These results suggest that the Orai hexamer and the Orai tetramer model built based on the hexameric crystal structure are in a closed conformation. In both channels, the location of salt ions within the pore seem to agree well with the expectations arose from the crystal structure of the Orai protein [11]: the negatively charged residues at the extracellular mouth of the pore attract sodium ions whereas the local concentration of positive charges from the basic residues are stabilized by chloride ions.

3.4.4. Can a TM1 Helix Rotation Open Orai Channels?

Recent studies implied that STIM opens the Orai pore by inducing a rotation of the pore-forming helices [36,67,68]. We use the term “open” for these channels with rotated TM1 helices. However, we do not expect this “induced” helix rotation to fully represent the conformational change STIM would cause through gating since the selectivity and gating of Orai channels are coupled. The models for the open Orai hexamer and tetramer channels were embedded in a pure POPC bilayer and solvated in a 150 mM NaCl solution. Then, we performed molecular dynamics simulations of these channels for 500 ns, after ~ 7 ns of equilibration as explained in the Methods section (see Figure 3.1). The RMSDs of the backbone atoms in the transmembrane domains were calculated based on the initial structures of the channels in order to assess whether the current simulations reached a stable conformation. It was calculated to be 2.4 \AA for the open Orai hexamer and 4.4 \AA for the open Orai tetramer. The RMSD of the hexamer remained the same after the helix rotation whereas it increased by 0.5 \AA in the tetramer due to the orientation change in its TM3 helices. The alpha-helices remained stable through the simulations. The analysis done for the closed Orai multimers was repeated for the new set of simulations in order to examine the changes helix rotation induced in both structures.

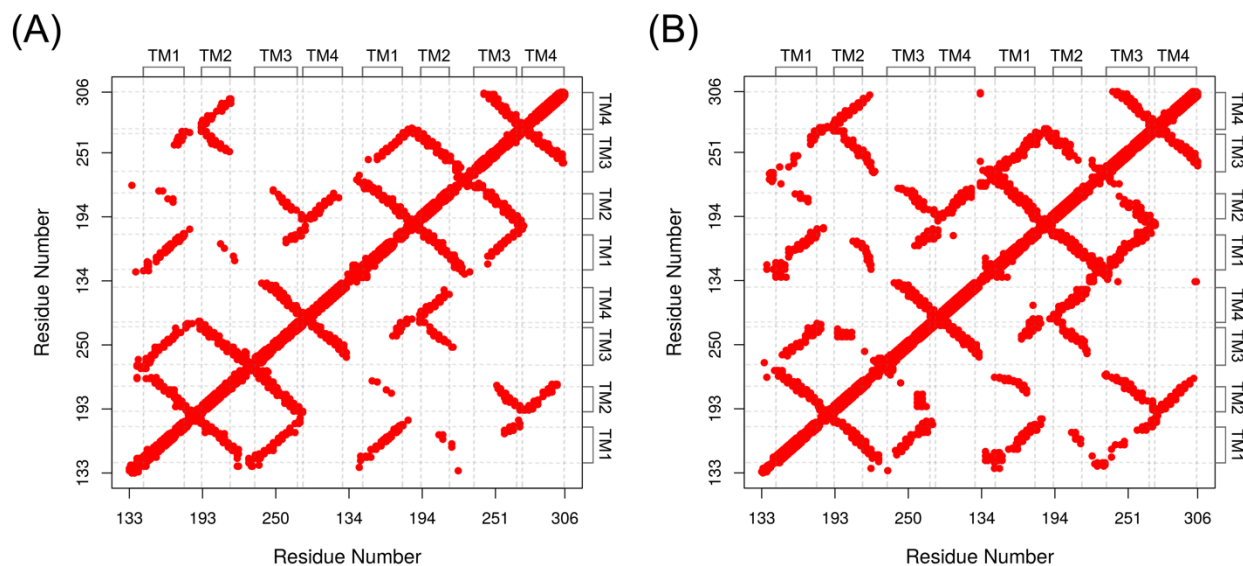


Figure 3.5. Contact probability maps of the open (A) hexamer and (B) tetramer Orai channels. These maps were averaged through the last 250 ns of the production trajectories by using one frame for every 0.01 ns. Then the maps were reduced to contact frequency maps of a dimer averaged over possible pairs of subunits from the Orai channels. Both axes show the residue numbers and the labels specifying the residues corresponding to the TM1-TM4 helices. The cut-off probability was set to 25% of the simulation time.

Upon helix rotation, the new set of analysis for side-chain contacts revealed that the hexamer loses contacts while the tetramer retains a similar number. Compared to 676 ± 6 contacts per monomer observed in the closed hexamer, the open hexamer maintains an average of 375 ± 4 contacts per monomer. Conversely, the Orai tetramer shows almost no change in the amount of contacts when opened: the tetramer with rotated TM1 helices preserves an average of 619 contacts (± 7) per monomer which is 20 contacts fewer compared to those calculated for the closed tetramer. These include all instantaneous contacts, counted from all individual monomers, averaged through the whole simulation trajectory without any cut-off for the probability of contact. Similar to our approach for the closed multimers, we focused on analyzing a subset of these contacts that, on average, are present in all the monomers and are formed for at least 25% of the simulation time. Figure 3.5 shows the contact probability maps of these resulting contacts, reduced to a dimer for both the open hexamer and tetramer.

As seen from the difference in density of the data points between Figure 3.2A and 3.5A, the average number of contacts significantly decreased in the hexamer due to the helix rotation. Then we identified the significant intra- and inter-monomer contacts by excluding the contacts

formed in the same transmembrane helices and those involving loop residues. The open hexamer possesses 119 intra-monomer and 88 inter-monomer contacts in the open hexamer (see Table 3.3). These contacts are 56 and 61 fewer, respectively, compared to those of the closed Orai hexamer. The open tetramer maintains 175 intra-monomer and 149 inter-monomer contacts. Interestingly, the former is 38 and the latter is 54 more compared to what we observed in the closed tetramer (see Table 3.2 and 3.3). Even though the helix rotation causes a significant change in the number of intra- and inter-monomer contacts in both multimers, the same secondary structure elements remain in contact, indicating that both structures can sustain the helix rotation.

Table 3.3. Significant intra-monomer contacts per monomer (inter-monomer contacts per interface) in the open Orai multimers

Region	Open hexamer		Open tetramer	
	Intra-monomer	Inter-monomer	Intra-monomer	Inter-monomer
TM1-TM1	Excluded	34	Excluded	49
TM1-TM2	36	5	52	13
TM1-TM3	17	13	58	21
TM2-TM3	29	17	22	31
TM2-TM4	0	19	0	35
TM3-TM4	37	0	43	0
Total	119	88	175	149

Upon helix rotation, the hexamer loses intra-monomer contacts in all regions: TM1-TM2, TM1-TM3, TM2-TM3 and TM3-TM4. However, the number of intra-monomer contacts of the open tetramer significantly increases in all regions except the TM2-TM3 regions in which it decreases by three contacts per monomer in comparison to the closed conformation. Interestingly, the open tetramer maintains significantly more intra-and inter-monomer contacts between TM1-TM3 compared to its closed conformations and open hexamer, whereas the hexamer loses 10 intra-monomer contact per monomer between in the same region upon helix rotation. The open hexamer also maintains fewer intra- and inter-monomer contacts between its TM2-TM3 helices compared to its closed conformation. The helix rotation causes opposite but pronounced changes in contacts between TM2 and TM3 helices of both multimers. In the tetramer, helix rotation causes TM2 helices to lose contacts with TM3 helices within the same monomers and to gain

more contacts with TM3 helices from the adjacent monomers. However, in the hexamer, the number of both intra- and inter-monomer contacts between TM2 and TM3 helices decreases upon the helix rotation. The orientations of TM3 helices are also different in the open Orai multimers. The decrease is more significant for the TM3 helix that showed an average tilt angle of 19° with a standard deviation of $\pm 7^\circ$ in the open tetramer, as opposed to 30° calculated for the closed tetramer. In the open hexamer, the average tilt angle was $25^\circ \pm 6^\circ$ for TM3 much closer to the one calculated for the closed hexamer ($26^\circ \pm 7^\circ$).

Throughout the simulations, the hexamer maintains 168 inter-monomer contacts (>25% probability) per interface whereas the tetramer preserves 318. Among them, 88 contacts per interface are formed by the residues belonging to the transmembrane alpha helices in the open hexamer and 149 inter-monomer contacts in the open tetramer. On one hand, the most pronounced decrease in the number of inter-monomer contacts is found in the TM1-TM1, TM1-TM2 and TM2-TM3 regions of the open hexamer compared to its closed conformation. On the other hand, the open tetramer possesses notably more inter-monomer contacts between all domains compared to its closed conformation. Helix rotation causes most significant differences in two regions in the tetramer: (1) TM1-TM2 and TM1-TM3 helices form more intra- and inter-monomer contacts and (2) TM2-TM3 helices form fewer intra-monomer and more inter-monomer contacts compared. In other words, the transmembrane helices in the tetramer form tighter contacts in the open state compared to all other cases – the open/closed hexamer and closed tetramer.

The average number of hydrogen bonds within both open channels does not vary significantly compared to those calculated from the simulations of the closed channels. The open hexamer maintains 225 ± 3 hydrogen bonds per monomer, while the open tetramer preserves 210 ± 4 hydrogen bonds per monomer on average. Noticeably, upon pore opening, all salt bridges are weaker regardless of the multimeric state of the structures due to presence of more water molecules in the pores. Upon helix rotation, the hexamer and tetramer maintain 7 and 6 intra-monomer salt bridges, respectively (see Figure 3.6). They share intra-monomer salt bridges between E178-K270, E245-K157 and E238-K150 residues. Most intra-monomer salt bridges of the open hexamer channel involve the loop residues. A particularly important salt bridge in the hexamer, formed between the selectivity filter (E178) and K270 residues, is maintained in two

monomers of this structure throughout the simulation time (see Figure 3.6A). One K270 residue in the open hexamer also form a weak intra-monomer salt bridge with the D184 residue as opposed to five intra-monomer salt bridges (between K270 and D182) maintained in its closed conformation. In addition, an intra-monomer salt bridge between E234-R239 is present only in the hexamer. The TM3 residues of the open tetramer form significantly more intra-monomer side-chain contacts with the TM1 residues and inter-monomer side-chain contacts with the TM1 or TM2 residues. As a result, the tetramer does not possess this salt bridge within its TM3 helices. On the other hand, the tetramer maintains a weak, intra-monomer salt bridge between E221-R155 residues that do not form in the hexamer. The E221 residues form inter-monomer salt bridges with R149 residues in both open multimers.

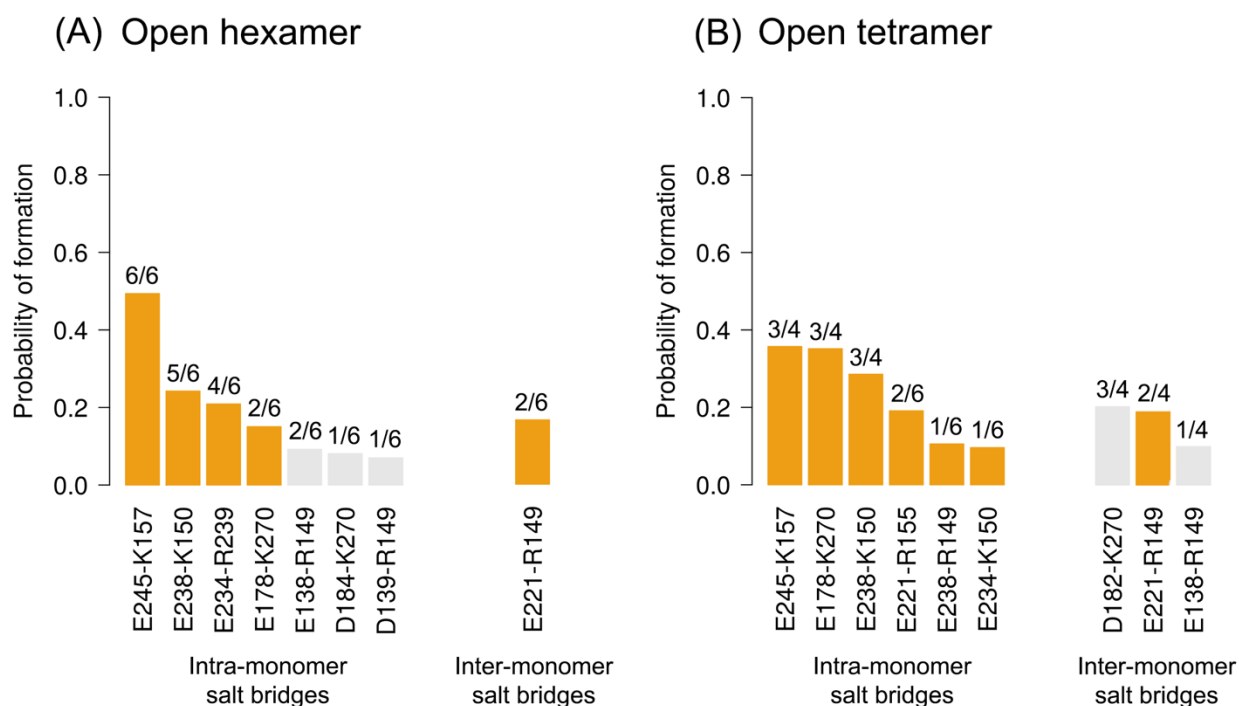


Figure 3.6. Salt bridges of the open (A) hexameric and (B) tetrameric assemblies of Orai proteins. The probability of formation was calculated the fraction of simulation time during which the length of the salt bridge is ≤ 5 Å. The analysis was done using the last 250 ns of the production trajectories of the open Orai multimers. The gray bars denote salt bridges involving at least one loop residue whereas the orange bars represent the salt bridges formed by residues from the transmembrane helices. The number, given for each bar, shows the number of occurrences of the salt bridges out of six monomers of the hexamer channel and out of four monomers of the tetramer channel.

Due to the helix rotation, E178 residues start to interact more with K270 residues in the open hexamer. This would lower the number of salt ions interacting with the selectivity filter in the hexamer compared to its closed conformation. Interestingly, the tetramer loses one of its E178-K270 salt bridges upon pore opening. Instead, it maintains three stable inter-monomer salt bridges between D182-K270, meaning that K270 residues interact with both E178 and D182 (see Figure 3.6B). Although weak compared to its closed conformation, the probabilities of salt bridges in the tetramer are overall higher than those of the open hexamer.

Finally, Figure 3.7A shows the densities of salt ions and water molecules within the pores of the open hexamer and tetramer channels. Both open multimers shows an affinity to sodium ions at the extracellular mouth of the pore. In the extracellular half of the pore ($0 \text{ \AA} < z < 25 \text{ \AA}$) within a radial distance of 10 \AA from the pore center, the average number of sodium ions is 4.9 ± 0.88 for the open hexamer (one less than for the closed hexamer) and 3.4 ± 0.71 for the open tetramer (one more than for the closed tetramer). This is due to the K270 salt bridges being shared by E178 and D182 residues in the open tetramer and the formation of two E178-K270 salt bridges, after the helix rotation, in the open hexamer. In the cytoplasmic part of the pore ($-25 \text{ \AA} < z < 0 \text{ \AA}$) within a radial distance of 10 \AA from the pore center, the average number of chloride ions is not significantly altered by the helix rotation in both multimers; the open tetramer still has 7.4 ± 0.79 chloride ions whereas the open hexamer interacts with 11.4 ± 0.39 chloride ions (one less compared to its closed conformation). Even though the location of the chloride ions changes as a result of the helix rotation, the average number of chloride ions attracted was comparable in both Orai multimers. Chloride ions within the basic part of the open tetrameric pore are more dynamic compared to those in the closed tetramer, keeping the basic residues less rigid. In the open hexameric pore, the chloride ions are mostly located between the residues R155 and K159.

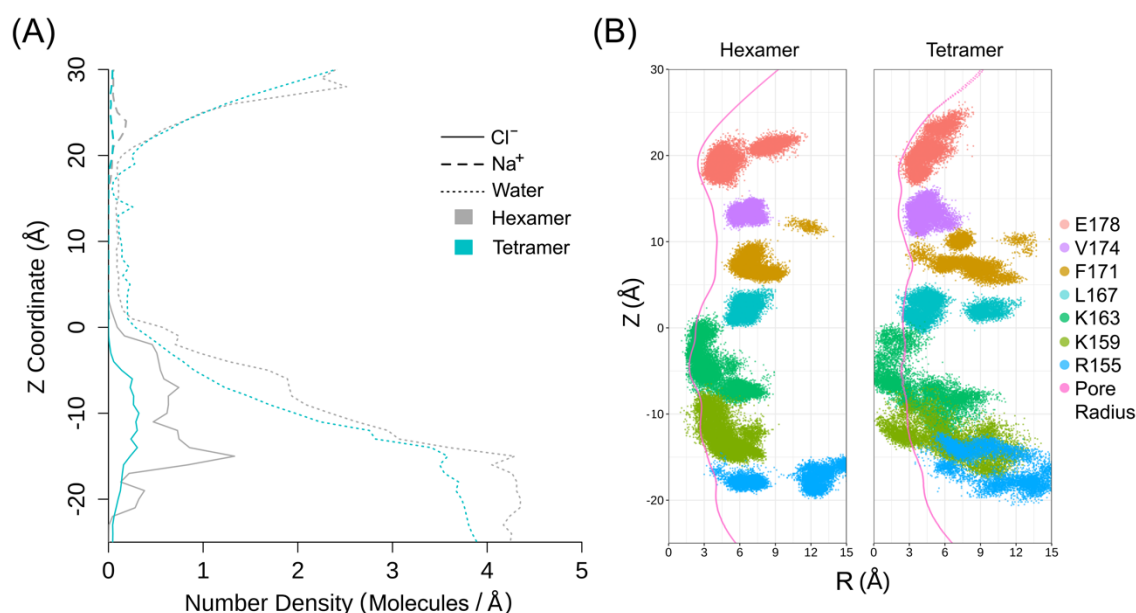


Figure 3.7. (A) Density profiles of salt ions (Cl^- and Na^+) and water molecules along the pores of the open Orai multimers. The number density was calculated as the number of molecules within a cylindrical slice along the pore axis (of radius 10 Å and height 1 Å). (B) Distribution of the geometric center of the sidechain atoms of the pore-lining residues E178 (CD, OE1 and OE2 atoms), V174 (side-chain heavy atoms), F171 (CE2, CG and CZ atoms), L167 (side-chain heavy atoms), K163 and K159 (NZ atoms), R155 (NE, NH1 and NH2 atoms) and the average value of the pore radius along the pore axis in the open hexamer and tetramer channels. The z coordinate is along the pore axis, with $z = 0$ Å corresponding to the center of the lipid bilayer. Analysis was done using the last 250 ns of the production trajectories.

Helix rotation significantly increases the stability of water molecules inside the pore for both open multimers. Since the pore radius of the hydrophobic part of the pore increases due to the helix rotation, both multimers possess more water molecules within their pores (see Figure 3.7). It is a more pronounced increase in the tetramer. The tetrameric pore is widened by about 1.5 Å in the hydrophobic part since the pore-lining residues (V174, F171 and L167) are relatively more flexible, sampling more area within the pore, compared to its closed conformation (see Figure 3.7B). Hence, these residues are more rigid compared to those in the closed hexamer channel. All of these imply that helix rotation makes the tetrameric pore more hydrated and flexible surrounded by transmembrane helices that form strong inter-monomer contacts. In the case of the Orai hexamer, helix rotation causes both residue-residue contacts and sodium concentration in the pore entrance to decrease.

3.5. Conclusion

We performed molecular dynamics simulations of the hexameric and tetrameric Orai structures. The hexamer structure is the crystal structure from the *D. melanogaster* Orai protein, while the tetramer model is built based on the hexameric structure. Both multimers maintain stable side-chain contacts, hydrogen bonds and salt bridges. The closed tetramer retains most of the contacts present in the closed hexamer. However, the hexamer maintains 27 more significant, inter-monomer contacts and 2 more salt bridges involving the residues belonging to transmembrane helices. Yet the salt bridges in the closed tetramer are found to have higher probabilities of formation, indicating that electrostatic interactions are maintained better compared to those identified in the closed hexamer. By analyzing their pore structures, we confirmed that these multimers form stable pores in a closed state as suggested in other studies [11,58]. The Orai tetramer has a more tightly-packed hydrophobic part within its pore that keeps the permeation pathway less hydrated compared to the hexamer. The closed Orai hexamer attracts more sodium channels in its pore entrance due to the fact that the selectivity filter residues (E178s) do not involve in forming salt bridges – which is not the case for the closed tetramer. Our results imply that, in terms of residue-residue contacts and pore dynamics, there is no direct evidence for eliminating the tetramer from being the active Orai channel, drawing attention once more to the studies suggesting that the Orai tetramer is the functional form of the channel [42–44,50,52,53,132,133].

Then, we tested if the pores of these multimers can be opened by a rotation of their pore-forming helices. This hypothesis is particularly interesting since it not only suggests that the hydrophobic gating of the Orai channel occurs through pore hydration induced by helix rotation, but also can possibly explain how the ion selectivity and gating of the channel are coupled [67,68,128]. The conformational changes necessary for pore opening, induced by STIM, are expected to be transmitted through contacts between the transmembrane domains [64,67,68,128]. Since the tetramer retains most of the structural features of the hexamer, we built the open structures of both multimers by rotating their pore-forming helices and performed molecular dynamics simulations to examine the effects of helix rotation. Although both structures can sustain the conformational changes due to the helix rotation, their responses are different. On one hand, the hexamer possesses 21% fewer stable contacts when opened. The decrease in the number of

contacts is observed for both intra- and inter-monomer contacts, as well as for the salt bridges. On the other hand, both types of contacts in the tetramer are increased by 39% upon helix rotation, while the salt bridges become less frequent. A noteworthy change in the salt bridges involves the K270 residues of the open tetramer. They are found to form salt bridges both with E178 and D182 residues, as opposed to only E178 residues in the closed conformation. As a result, the selectivity filter of the open tetramer attracts slightly more salt cations compared to its closed conformation. In addition to the changes in contacts, the number of water molecules in the pores of both assemblies is increased upon opening the channel through a rotation of the TM1 helices.

As a whole, this study demonstrates that the tetrameric assembly of Orai proteins displays residue-residue contacts and pore dynamics comparable to those of the hexameric assembly, and therefore stands as a reasonable candidate for store-operated calcium entry. Our results not only show that helix rotation increases the pore hydration, but also support two observations from functional studies of Orai mutants. The residue-residue contact analysis presented here shows that both Orai multimers maintain stable contacts between TM1 and TM2/TM3 helices. These contacts are particularly important for the channel activation as indicated by the mutagenesis data of Yeung et al. [68]. In their study, Yeung et al. [68] demonstrated that disrupting the contacts between TM1 and the TM2/3 ring destabilizes the gating of Orai channels by STIM1 proteins. In addition, our results show significant displacement in the F171 residues radially away from the pore center, increasing the pore hydration. This is also in line with another study in which Yamashita et al. [67] have studied various Orai mutants both experimentally and computationally. They concluded that STIM induced a helix rotation in the pore-forming helices of Orai proteins to increase pore hydration in the Orai pore by displacing the F171 residues (F99 in *H. sapiens* Orai1) away from the pore axis [67].

Recent studies [64,68] point out the importance of the contacts between the Orai transmembrane domains for channel activation. The presence of a hydrophobic part of the Orai pore also hints at a hydrophobic gating mechanism, as suggested by both experimental and computational studies [58,67,68,128,151]. The most recent hypothesis for hydrophobic gating is the rotation of pore-forming helices [67,68,128]. Our results support this by demonstrating that the most pronounced effect of helix rotation is the increase in pore hydration in both multimers. Readers should note

that we do not expect an induced rotation of pore-forming helices to replicate the gating by STIM proteins. This is particularly clear since channel activation depends on the number of STIM proteins bound to Orai proteins [29,36,67]. A more realistic exploration of these multimers as candidates of a highly calcium-selective channel would require a crystal structure of the Orai channel in an open conformation. Until it is determined, our study cannot rule out the Orai tetramer as a potential candidate of the active Orai channel.

Chapter 4. Origin of Ion Selectivity in Orai Channels

4.1. Abstract

In most animal cells, one of the most well-known mechanisms of calcium influx is the store-operated calcium entry that is mediated by calcium release-activated calcium (CRAC) channels. Orai proteins form the pore subunit of CRAC channels whereas STIM proteins activate the Orai pore after sensing the depletion of calcium stores in the endoplasmic reticulum. From a mechanistic viewpoint, three questions about CRAC channels remain unresolved regarding the channel selectivity, gating and multimeric state in its active form. We previously showed that the hexameric and tetrameric assemblies of Orai proteins form stable ion pores and comparable residue-residue contacts. The tetrameric Orai pore is narrower, hence less hydrated. Pore hydration increases in both channels due to the rotation of pore-forming helices which was recently proposed as the channel gating mechanism. Here, we used free energy calculations to further test the helix rotation as a possible mechanism for the channel gating. By performing molecular dynamics with umbrella sampling, we examined the permeation of single Na^+ , K^+ and Ca^{2+} ions through the pores of the hexameric and tetrameric Orai channels in the closed and open conformations. Our results demonstrated that Orai multimers do not show a significant selectivity of Na^+ against K^+ or vice versa. However, the oligomeric state of the Orai channel makes a difference in the case of Ca^{2+} : the size of the hexameric Orai pore is better adapted to the permeation of a fully hydrated Ca^{2+} ion than that of the tetramer pore.

4.2. Introduction

Calcium (Ca^{2+}) is a vital signalling messenger for several cellular functions such as muscle contraction, immune activation, and proliferation [27–29]. In most animal cells, intracellular Ca^{2+} concentration is tightly regulated by Ca^{2+} pumps in the plasma membrane and in the endoplasmic and sarcoplasmic reticulum membranes [27]. One well-known mechanism of Ca^{2+} influx is the store-operated calcium entry, mediated by calcium release-activated calcium (CRAC) channels. Ca^{2+} currents generated by CRAC channels have distinct characteristics: they correspond to low single-channel conductance, are highly selective against Na^+ and K^+ ions, are directly dependent on Ca^{2+} stores of the endoplasmic reticulum (ER), display inward rectification, and are independent of the membrane voltage [27,34,153,154]. Two proteins, Orai

and STIM (Stromal Interaction Molecule), have been identified as the molecular components of CRAC channels [30–33,35,155]. The plasma membrane protein, Orai forms the pore subunit of CRAC channels whereas the ER membrane resident STIM protein activates the Orai pore.

The pore formed by the assembly of Orai proteins presents an unusual environment for ion permeation. The crystal structure of *Drosophila melanogaster* (*D. melanogaster*) Orai, which shares 73% sequence identity with its human ortholog (Orai1), has revealed a channel formed of six Orai monomers, and an ion pore lined with both hydrophobic and basic residues [11] providing few opportunities for the permeating cation to directly coordinate the protein. This first crystal structure has challenged the established idea that the active form of the channel was a tetrameric assembly of Orai [43–50,156]. More recent studies [36,54,56] have also identified the functional Orai as a hexamer, or have detected store-operated calcium entries using different Orai1 concatemers, including dimers, tetramers and hexamers (likely assembling into hexamer-like channels) [55]. However, while the focus has shifted from the tetrameric to the hexameric channel, no studies have yet explained the functional differences between these multimeric states.

The crystal structure of *D. melanogaster* Orai has provided a starting point for several computational studies of Orai channels, focusing on their inhibition mechanism [60] and activation mechanism [59,63–66], or on their interaction with calmodulin [61,62]. Dong et al. [58] studied the general permeation characteristics of Na⁺ and confirmed that the hexamer crystal structure was closed. More recently, Yamashita et al. [67] and Yeung et al. [68] have experimentally and computationally investigated the wild-type Orai channel and its variants, and have proposed that STIM activates the Orai channel by inducing a rotation of its pore helices. Yamashita et al. [67] have also examined several Orai variants to identify the roles of the pore-lining residues in ion permeation, and have concluded that the helix rotation causes pore dilation in the hydrophobic region of the pore without substantively altering solvent-exposure of the residues lining the pore. Recent studies [36,67,68], showing the dynamic nature of ion gating and selectivity of Orai proteins, suggested that Orai pore can be opened through the rotation of its inner helices. This idea, which could explain how Orai's calcium selectivity is altered, is yet to be computationally explored. Additionally, none of the computational studies in the literature have investigated ion permeation along other Orai multimers such as the tetrameric assembly of

Orai proteins, despite that the tetramer was initially thought to be the active form of the CRAC channel [46] and has been reported in several experimental studies [42–45,47–50]. From a mechanistic viewpoint, three questions about CRAC channels remain unresolved: (1) What structural elements of the Orai pore are responsible for its ion selectivity? (2) What is the likely mechanism of gating in response to store depletion? and (3) Which multimeric state of Orai (tetramer or hexamer) is most likely functional?

In this paper, we studied the permeation of single Ca^{2+} , K^+ and Na^+ ions through the pores of *D. melanogaster* Orai channels using molecular dynamics simulations combined with umbrella sampling. Since various studies in the literature report different oligomeric states of Orai proteins including tetrameric [42,50] or higher-order stoichiometries [52,53], we compared the permeation along the pores of both hexameric and tetrameric Orai channels. We built a homology model of a tetrameric Orai channel from the hexameric crystal structure [11] and, according to the recent propositions of the gating mechanism [67,68], we modeled the open states of these multimers by rotating the pore-forming helices. These model structures were used to investigate the origin of ion selectivity of both the hexameric and tetrameric Orai assemblies in their open and closed conformations. Since the rotation of the pore-forming helices is suggested as a possible gating mechanism of Orai channels [67,68], it is crucial to examine how this conformational change affects the free energy profiles of ion permeation.

4.3. Computational Details

4.3.1. Modeling of the Closed and Open Orai Channels

The crystal structure of *D. melanogaster* Orai protein (Protein Data Bank ID: 4HKR) [11] was used as a template to generate the structure of the hexameric Orai channel with Modeller [97]. Based on the hexameric Orai channel, a homology model of the tetrameric assembly of Orai proteins were generated. Specifically, we built the tetramer structure by transforming the cylindrical coordinates (r, θ, z) of four adjacent units from the hexamer to $(r, 6\theta/4, z)$ so that the channel has a fourfold symmetry in the TM1-TM4 helices and twofold symmetry in the TM4-extension helices.

The open Orai structures were generated by rotating the pore-forming TM1 helices (formed by the residues 144 to 178) by 30° counter clockwise. For the simulations involving Ca²⁺ and K⁺ permeant ions, we added one permeant ion to the simulation box and the number of Cl⁻ ions was adjusted to neutralize the total charge of the systems.

4.3.2. Simulation Setup

Before setting up the Orai-membrane systems, we included the residues between 133 and 306; neutralized the N and C termini in all systems; and aligned the orientation of the Orai channels with respect to the membrane surface using Orientations of Proteins in Membranes (OPM) database [138] (entry 4HKR). Then, we used CHARMM-GUI [139,140] to embed each Orai channel in a simulation cell containing an explicit 1-palmitoyl-2-oleoyl-phosphatidylcholine (POPC) membrane and a 150 mM NaCl solution. H206 residues were protonated at their epsilon nitrogen atoms while the default protonation states were kept for the rest of the amino acids.

The hexameric Orai-membrane simulation systems included ~50 lipids at the top and bottom leaflets of the membrane, ~12000 water molecules, 29 Na⁺ ions, and 29 Cl⁻ ions. The total number of atoms was ~64000 in a hexagonal box for each hexameric simulation system. Similarly, the tetrameric Orai-membrane systems included ~50 lipids at the top and bottom leaflets of the membrane, ~10000 water molecules, 25 Na⁺ ions, and 25 Cl⁻ ions. The total number of atoms was ~53000 in a rectangular simulation box for each tetrameric simulation system.

The CHARMM36 force field [111] and TIP3P water model [141] were used. CHARMM36 is a classical force field that uses a set of non-bonded parameters to calculate non-bonded interactions. These non-bonded parameters were obtained by fitting quantum mechanical calculations to experiments in high dilution [157]. The experimental data often consists of single atom properties, including hydration free energies at infinite dilution [158]. General parameters developed based on such properties assume an ion to be in an “average” water environment, and therefore might not be capable of describing interactions involving ions and protein atoms. Unsurprisingly, our simulations involving the Ca²⁺ ion showed that the pair interaction between Ca²⁺ and carboxylate is extremely strong. Therefore, we repeated these simulations using a set of NBFIX parameters for the Ca²⁺-OAc⁻ (O on carboxylate) parameterized to fit well with the

experimentally measured osmotic pressures in physiologically relevant concentrations [157] (see the parameters listed in Table 4.1). Even though new parameters showed improvements in comparison to the CHARMM36 force field, we still observed an extremely strong binding of the Ca^{2+} ion to the glutamate side chains. This emphasizes the fact that it is challenging to generate a set of parameters that can capture the interactions involving a divalent ion in different environments (water and protein).

Table 4.1. NBFIX parameters used for interactions involving a Ca^{2+} ion

Atom pair	ϵ (kcal/mol)	σ (Å)
CAL-CLA	-0.134164	3.698
CAL-OCL	-0.120000	3.225
CAL-O2L	-0.120000	3.304
CAL-OC	-0.120000	3.190 [157]

Throughout the simulations, the temperature is kept constant at 303.15 K using Langevin dynamics with a coupling coefficient of 1 ps^{-1} [108]. Pressure is also kept constant at 1 atm using a Nosé-Hoover Langevin piston [109] with a piston period of 50 fs and a piston decay of 25 fs. All bonds involving hydrogen atoms are constrained using the SHAKE/RATTLE algorithm [142]. Nonbonded interactions are calculated using particle mesh Ewald [143] and the recommended CHARMM cut-off scheme [144]. The simulations are run using NAMD 2.12 [145] and data analysis is done using VMD [150] and MDAnalysis [148,149].

4.3.3. Molecular Dynamics Simulations of the Orai Channels

The simulation systems were relaxed using an adapted version of the relaxation steps in the NVT ensemble suggested by Jo and coworkers [140] for 0.67 ns. In addition to their scheme, the harmonic restraints on the dihedral angles of TM1 residues (144 to 178) (with a force constant of 500 kcal/mol), the harmonic constraints on the α -carbons of pore-lining residues (152, 155, 159, 163, 167, 171, 174, 178 with a force constant of $1 \text{ kcal/mol}/\text{Å}^2$) and the restraints on the bond distances of atoms involved in forming hydrogen bonds found in the initial structure to their initial values (with a force constant of $1 \text{ kcal/mol}/\text{Å}^2$) were added. The harmonic constraints on the α -carbons of pore-lining residues were kept through the simulations. Two of these constraints

(on the dihedral angles of TM1 residues and hydrogen bonds) were slowly removed within the first 6 ns in the NPT. After 2 ns, the harmonic restraints of the bond lengths of the atom pairs forming hydrogen bonds were removed (see Table 4.2). At the end of 6 ns, we removed the harmonic restraints on the dihedral angles of TM1 residues. The systems were simulated for 2 more ns in the NPT ensemble with the harmonic constraint on the α -carbons of pore-lining residues with a force constant of 1 kcal/mol/Å².

Table 4.2. Hydrogen bonds constrained during the equilibration phase

Residue 1	Atom 1	Residue 2	Atom 2
E262	OE2	T199	OG1
H206	ND1	S165	OG
W248	NE1	S161	OG
C267	SG	T200	OG1

4.3.4. Umbrella Sampling Simulations

The force constant on the α -carbons of pore-lining residues were reduced to 0.5 kcal/mol/Å² for the rest of the simulations. While setting up the umbrella sampling windows, the z -coordinate distance of the permeant ion with respect to the geometric center of pore-lining residues was set as the collective variable [159]. We generated a window centered at every 1 Å along the z -coordinate spanning -25 Å to +30 Å using the previous window’s configuration at 100 ps. As a result, a total of 56 windows was generated for each umbrella sampling simulation of an Orai-membrane system and each window was simulated for 4 ns. The windows centered at $z > 24$ Å simulated for 4 ns longer. For the simulations involving calcium as the permeant ion (without the coordination number constrained), each individual window was simulated for 8 ns. The calcium simulations were repeated two more times: the one with an additional constraint of calcium ion being coordinated by 6 water molecules and another with the additional constraint of calcium ion being coordinated by 7 water molecules. All windows of these simulations were run for 12 ns. The force constant for the harmonic constraint used in the umbrella sampling simulations was set to 2.5 kcal/mol/Å² to keep the z -coordinate distance of the permeant ion with respect to the pore center at the desired value. Additionally, a second collective variable (In NAMD terminology,

the collective variable used is named distanceXY) was used in these simulations to constrain the permeant ion inside the pore. With this collective variable, the permeant ions were restricted to stay within a 10 Å (5 Å) radius plane for hexameric (tetrameric) Orai systems in all systems using a force constant of 50 kcal/mol/Å². Free energy profiles of translocating an ion through the Orai pores were generated using Alan Grossfield's Weighted Histogram Analysis Method (WHAM) code (Version 2.0.9) [160] after discarding the first 300 ps of each window. In the case of calcium simulations with the coordination number constraint, the first 4 ns of each window was excluded from the calculation of the free energy profiles. In all calculations, the error on the free energy was estimated within ± 1 kcal/mol by using four 1 ns-long parts of the simulations involving Na⁺ and K⁺ ions and four 3 ns-long parts of the simulations using the Ca²⁺ ion.

4.4. Results and Discussion

4.4.1. Orai Channel Structure and Generation of the Models

Each subunit of the Orai channel consists of four transmembrane helices (TM1 to TM4) and an extension helix (TM4-extension). The Orai subunits assemble into a helical bundle in which the TM1 helices form a central pore, surrounded by a ring of alternating TM2 and TM3 helices (see Figure 4.1A). Helices TM1 to TM4, which form the core of the helical bundle, adopt a quasi-sixfold symmetry (see Figure 4.1A). By contrast, the TM4-extension helices, which are not shown in Figure 4.1A, alternate between two different conformations and give the channel an overall threefold symmetry. Starting from the extracellular side, the permeation pore is lined with negatively-charged residues E178, forming the so-called selectivity filter, followed by hydrophobic residues V174, F171 and L167 (see Figure 4.1B). Below this hydrophobic region are positively-charged residues K163, K159 and R155, forming the “basic” region.

The tetrameric assembly is built from the hexamer crystal structure, by morphing four adjacent units of the “ABABAB” hexamer into a fourfold-symmetric “ABAB” tetramer. Both the hexamer and the tetramer models are built without the TM4-extension helices and, therefore, have sixfold and fourfold symmetries, respectively (see Figure 4.1A and 4.1C). Because the TM4-extension helices are expected to undergo large-scale motions during gating [57,152], their conformations would be difficult to sample using molecular dynamics simulations. These models, which are generated using the crystal structure [11] in which the pore is in a closed state

[58], will be referred to as “closed hexameric” and “closed tetrameric” structures. To generate the “open” hexameric and “open” tetrameric structures, each TM1 helix (residues 144 to 178) is rotated by 30° counter clockwise (for the hexamer, see Figures 4.1D and 4.1E). We use the term “open” because we observe that the rotation of the TM1 helices increases the diameter of the Orai pores and makes ion permeation possible, but we do not expect this movement to fully represent the gating transition induced by STIM proteins. The models are embedded in a pure 1-palmitoyl-2-oleoyl-phosphatidylcholine (POPC) bilayer and solvated in a 150 mM NaCl solution.

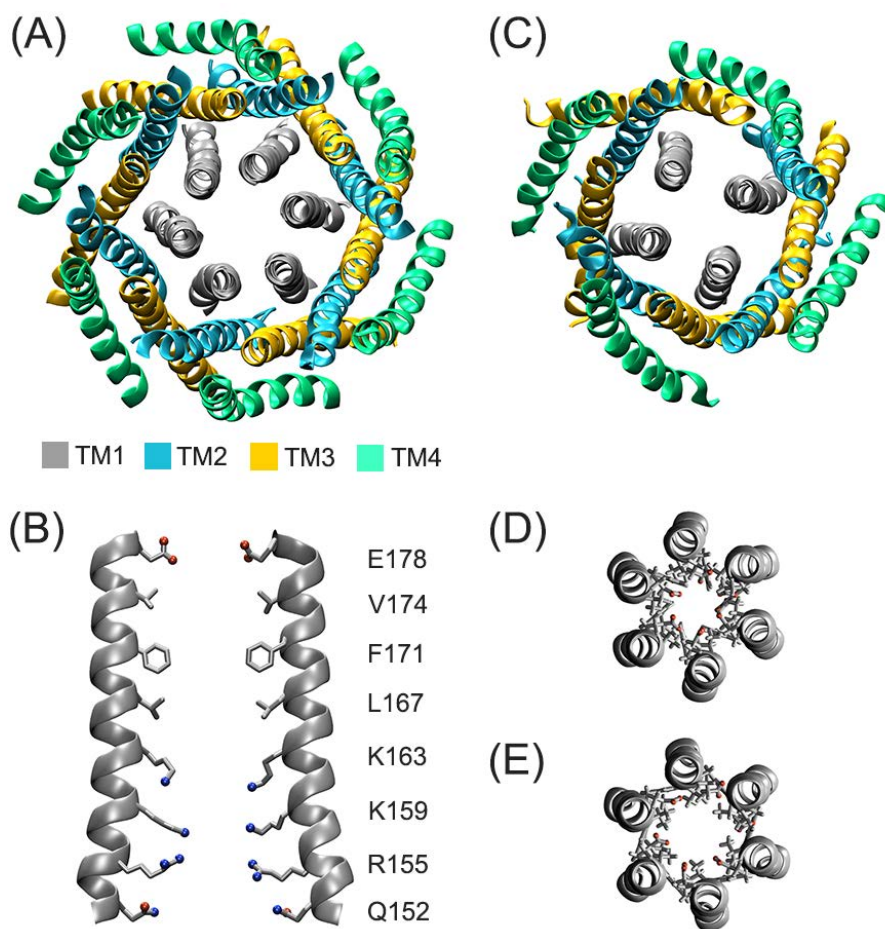


Figure 4.1. (A) Top view of the transmembrane helices forming the hexamer assembly of Orai proteins, after 8 ns of equilibration. (B) Side view of two opposite TM1 helices and their pore-lining residues. (C) Top view of the transmembrane helices forming the tetramer assembly model, after 8 ns of equilibration. Top view of the TM1 helices in the (D) closed and (E) open forms of the hexameric channel. Helices are shown in a cartoon representation whereas side chains of the pore-lining residues are represented as sticks. Oxygen atoms are red and nitrogen atoms are blue. In (D) and (E), for clarity, only the side chains of E178, V174 and F171 are shown.

4.4.2. Stability of Orai Channels

All four systems simulated, the closed and open forms of both hexameric and tetrameric assemblies, display stable pore structures. The average root mean square deviation (RMSD) of the backbone atoms of the transmembrane regions is 1.8 Å for the closed hexamer and 2.3 Å for the open hexamer, while it is 3.2 Å and 3.2 Å for the closed and open tetramer. For the Orai hexamers, the RMSD is calculated relative to the crystal structure and for the Orai tetramers, it is calculated relative to the initial homology model. The higher RMSD values for the tetramers reflect the fact that the radius of the TM1 helix bundle contracts by about 1.5 Å during equilibration. More importantly, the α -helices remain stable in all simulation systems.

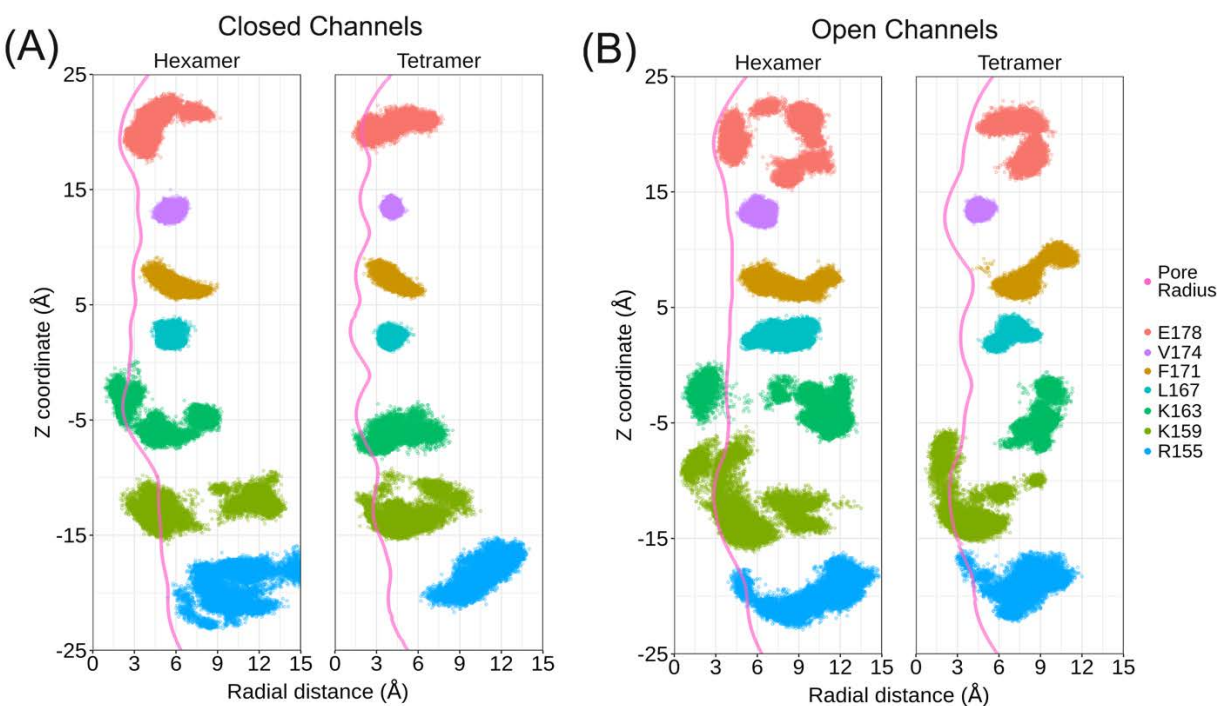


Figure 4.2. Distribution of the geometric center of the sidechain atoms of the pore-lining residues E178 (CD, OE1 and OE2 atoms), V174 (side-chain heavy atoms), F171 (CE2, CG and CZ atoms), L167 (side-chain heavy atoms), K163 and K159 (NZ atoms), R155 (NE, NH1 and NH2 atoms) and the average value of the pore radius along the pore axis in the (A) closed and (B) open Orai channels. The z coordinate is along the pore axis, with $z = 0$ Å corresponding to the center of the lipid bilayer. Analysis is done using the 8 ns-long umbrella sampling production trajectories.

Figure 4.2 shows the profiles of the pore radius for each simulation system (calculated using HOLE [146,148]), as well as the radial positions of the pore-lining residues. In the closed conformation (see Figure 4.2A), the hexamer pore is narrowest around residues E178 and K163

but remains wide enough to accommodate water molecules at any position along the pathway. By contrast, the tetramer pore is narrowest in the hydrophobic region, which suggests that it would be impermeable to any charged species. In the closed conformation, the side chains of residues E178, V174, F171, and L167 are highly ordered, while the more flexible (and better hydrated) residues K163, K159, and R155 can be found in a number of alternate conformations (see Figure 4.2A). For both hexamer and tetramer, the 30° rotation of the TM1 helices results in a widening of the pore (see Figure 4.2B). In that “open” conformation, the narrowest region is around residues E178 and K159 for the hexamer, and around residues V174 and K159 for the tetramer. In the hexamer assembly, this suggests a possible gatekeeping role for E178 and K159 residues.

In all four systems, the extracellular entrance of the pore shows a local concentration of sodium ions around the E178 residues (see Figures 4.3C and 4.3F). Conversely, chloride ions concentrate around basic residues K163, K159 and R155, on the intracellular side of the pore. The simulations show that, while water molecules can be found at all positions along the permeation pore whether it is open or closed, the tetramer pore contains fewer water molecules than the hexamer pore. The tetramer also contains fewer sodium ions around the selectivity filter and fewer chloride ions in the basic region.

For both hexameric and tetrameric assemblies, the 30° rotation of the TM1 helices increases pore hydration. Figure 4.2B shows that side chains E178, F171 and L167 explore a larger area within the pore and therefore allow more water molecules to enter the hydrophobic region. Interestingly, the forced TM1 rotation, which allows the pore to open, also causes a salt bridge to form between E178 and extracellular residue K270. In the open Orai hexamer, an average of two of the six E178 residues interact with K270 residues, while all four E178 residues interact with K270 residues in the open Orai tetramer. As a result of this competition for E178 side chains, fewer sodium ions interact with E178 in the open channels than in the closed channels. For the tetramer in the open conformation, the position of the local sodium concentration shifts outwards by 5 Å, compared to the closed conformation (see Figures 4.3C and 4.3F). This shift is not observed for the open hexamer, which forms only two E178-K270 salt bridges on average.

4.4.3. Ion Permeation through the Closed Hexameric and Tetrameric Channels

4.4.3.1. Closed Hexamer

The free energy profiles for moving single Ca^{2+} , K^+ and Na^+ ions along the closed hexamer Orai pore are shown in Figure 4.3A. The profiles reveal that the pore is impermeable to Ca^{2+} and creates a free energy barrier of 8.8 kcal/mol for Na^+ and of 9.3 kcal/mol for K^+ . The free energy profiles have similar features for both Na^+ and K^+ ions: an energetically favored binding position at the selectivity filter (E178), followed by a steep energy barrier in the hydrophobic region of the pore (V174, F171, L167) and a gradual energy decrease across the basic region (K163, K159, R155). At the selectivity filter, Na^+ and K^+ ions tend to sit below the E178 side chains and are typically coordinated by one or two of the six E178 side chains and by four or five water molecules (see Table 4.3 for detailed coordination numbers).

In preliminary simulations using the force field without any additional bias (see Section 4.3), we find that the Ca^{2+} ion is typically coordinated by three of the six E178 side chains and by three water molecules (see Table 4.3). While the position of the binding site resulting from such coordination is consistent with the crystal structure of Hou et al.[11], the interaction between the Ca^{2+} ion and the multiple E178 side chains, as described by the force field, creates an artificially strong affinity at the selectivity filter (see Figure 4.4). Since the force field was calibrated to describe the pairing of Ca^{2+} with a single carboxylate group in aqueous solution, we do not expect it to be as accurate when multiple carboxylate groups coordinate the ion. To facilitate comparison with the results for the open channel, the free energy profile for Ca^{2+} in Figure 4.3A is computed while constraining the water coordination number of Ca^{2+} to be at least 7. This constraint avoids direct interactions between the divalent ion and the E178 side chains, and, as will be seen later, is more consistent with the coordination spontaneously observed for Ca^{2+} going across the open tetramer channel (see Figure 4.4). Once the constraint is applied, the Ca^{2+} ion interacts with E178 residues less frequently. As a result of the forced water coordination and of more persistent interactions with the Q180 backbones and D182 side chains, the free energy minimum for Ca^{2+} is located at $z = 23 \text{ \AA}$, about 6 \AA above that for Na^+ or K^+ ions (see Figure 4.3A).

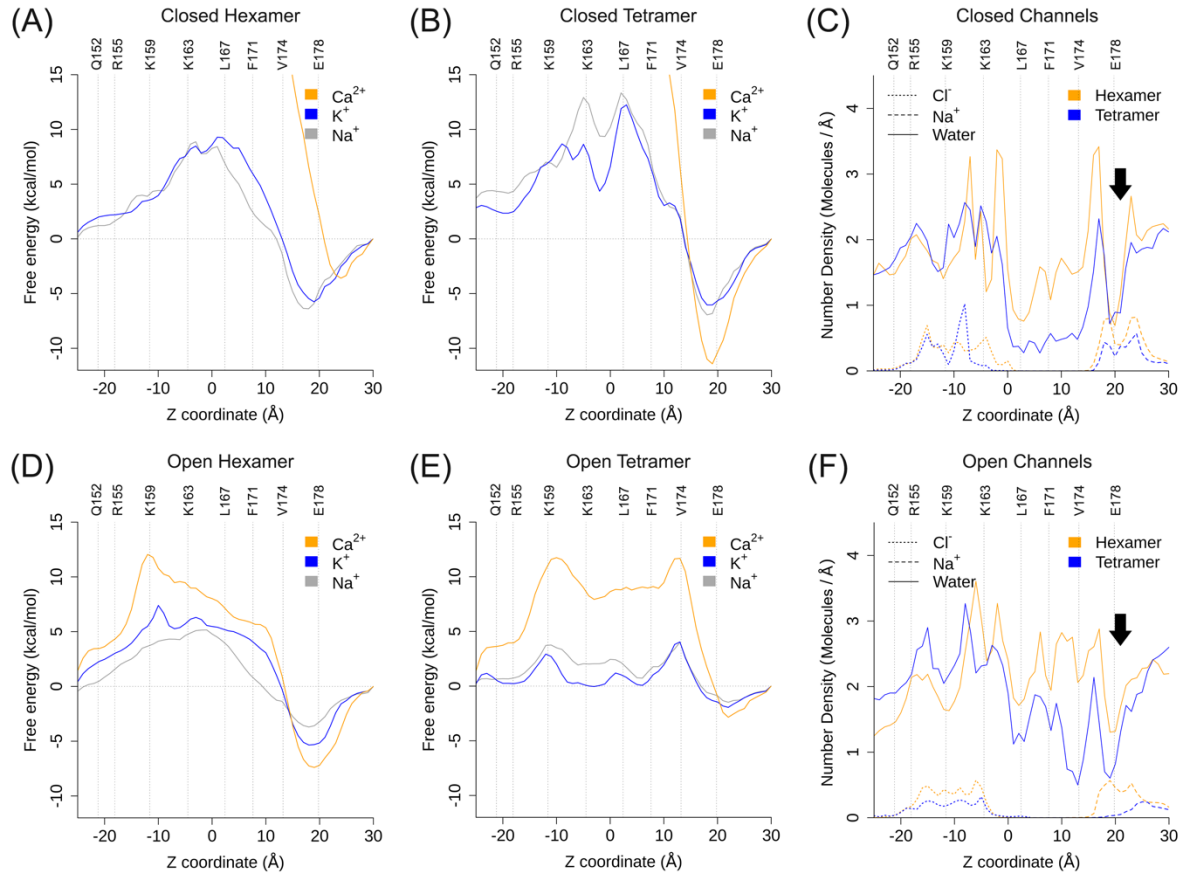


Figure 4.3. Free energy profiles for single Ca²⁺, Na⁺ and K⁺ permeation through the (A) closed hexameric, (B) closed tetrameric, (D) open hexameric, and (E) open tetrameric Orai channels. Panels (C) and (F) show the number densities of salt ions (Cl⁻ and Na⁺) and water molecules along the pores of the closed and open Orai multimers, respectively. The black arrow shows the Ca²⁺ position found in the crystal structure of Orai mutant, K163W [11]. In all graphs, the x-axis represents the z-coordinate of the permeant ion with respect to the center of the pore, whereas the vertical dashed lines represent the average z-coordinate of the side chain atoms of the pore-lining residues (excluding hydrogen atoms). The number density was calculated as the number of molecules within a cylindrical slice along the pore axis (of radius 10 Å and height 1 Å) using the 8 ns-long umbrella sampling production trajectories.

The free energy barrier created by hydrophobic residues V174, F171, and L167 is pronounced for Na⁺ and K⁺ ions but is thermodynamically insurmountable for the divalent Ca²⁺ ion (see Figure 4.3A). A second energy barrier occurs around residues K163, when the permeant ion encounters the Cl⁻ ions that condensate in the basic region of the pore. These Cl⁻ ions disrupt the solvation shell of the cation and the energy barrier reflects the transition from solvent-separated Na⁺/Cl⁻ or K⁺/Cl⁻ pairs to contact pairs. As the Na⁺ or K⁺ ion moves further down the basic region, the pore becomes wider and the ion gets progressively better solvated by both water

molecules and Cl^- ions, and its overall free energy decreases. On the intracellular side, basic residues R155, K159, and K163 create a free energy barrier as the ion moves up into the pore, likely due to the electrostatic repulsion between the cation and the positively charged side chains, which are only partially screened by the Cl^- ions present in the basic region.

Table 4.3. Coordination of the permeant ions through the closed and open Orai channels. The cut-off distance is set to 3.3 Å. For the analysis, 4 ns long umbrella sampling windows are used excluding the first 300 ps. W represents the number of water molecules coordinating the permeant ion.

z (Å)	<i>Closed Hexamer</i>						<i>Closed Tetramer</i>												
	Na ⁺			K ⁺			Ca ^{2+*}			Na ⁺			K ⁺			Ca ^{2+*}			
	W	E178	Cl ⁻	W	E178	Cl ⁻	W	E178	Cl ⁻	W	E178	Cl ⁻	W	E178	Cl ⁻	W	E178	Cl ⁻	
18	4.7	1.1	0	4.1	2.1	0	3.1	3.0	0	4.7	0.9	0	4.8	1.6	0	5.1	1.0	0	
12	5.4	0	0	6.1	0	0	5.3	1.0	0	4.9	0	0	4.4	0	0	5.1	1.0	0	
5	5.5	0	0	5.1	0	0	7.1	0	0	5.0	0	0	4.9	0	0	7.0	0	0	
0	4.5	0	0.6	5.6	0	0.1	5.0	0	1.0	5.2	0	0	4.3	0	0.7	7.0	0	0	
-5	1.2	0	3.4	3.5	0	2.1	4.0	0	2.0	4.7	0	0.4	3.6	0	1.1	5.6	0	0.9	
-10	3.5	0	1.8	2.7	0	2.7	3.0	0	3.0	1.9	0	2.9	2.8	0	2.4	5.6	0	1.0	
z (Å)	<i>Open Hexamer</i>						<i>Open Tetramer</i>												
	18	4.8	0.9	0	5.2	1.6	0	4.0	2.0	0	5.4	0	0	5.9	0.1	0	7.1	0	0
	12	5.4	0	0	6.3	0	0	5.2	0.9	0	5.0	0	0	5.2	0	0	7.0	0.2	0
	5	5.8	0	0	6.4	0	0	7.1	0	0	5.7	0	0	6.1	0	0	7.2	0	0
	0	5.6	0	0.1	6.2	0	0.2	6.2	0	0.5	5.0	0	0.5	6.0	0	0.1	7.1	0	0
	-5	4.9	0	0.7	4.6	0	1.3	6.8	0	0.3	4.3	0	1.1	5.1	0	0.8	6.4	0	0.5
	-10	3.3	0	2.0	3.6	0	2.1	6.2	0	0.5	3.3	0	1.7	3.6	0	0.7	6.1	0	0.6

*Calcium coordination numbers obtained without the restraint on the water coordination number and correspond to the free energy profiles of Figure 4.4. For the free energy profiles of Figure 4.3, the calcium ion is constrained to be coordinated by at least 7 water molecules.

4.4.3.2. Closed Tetramer

Figure 4.3B shows the free energy profiles for moving single ions along the closed tetramer Orai pore. As expected from the pore radius profiles of Figure 4.2A, the free energy profiles confirm that the tetramer creates an even more effective barrier to ions than the hexamer: 13.3 kcal/mol for Na^+ and 12.2 kcal/mol for K^+ . Similar to the closed hexamer, the closed tetramer possesses an

ion binding site around E178 residues, followed by a hydrophobic barrier. That energy barrier is higher than for the hexamer because the hydrophobic region of the pore is more tightly packed and less hydrated. In the closed tetramer, in the narrow region of the pore ($z = 12 \text{ \AA}$), the water coordination number of Na^+ goes down to 4.9, compared to 5.4 in the closed hexamer (see Table 4.3). The difference is larger for a K^+ ion at the same position, with a water coordination number of K^+ is 4.4 in the closed tetramer, compared to 6.1 in the closed hexamer. Since some of the conformations sampled along the permeation pathway of the closed structures are thermodynamically unfavorable, the ion is kept in the central region of the pore using a restraint on its radial distance from the pore center (see Section 4.3 for details). This restraint prevents the ion from escaping between the transmembrane helices as opposed to entering the tightly-packed hydrophobic region in the pore of the closed tetramer channel.

The profiles of Figures 4.3A and 4.3B are better understood in light of Figure 4.3C, which shows the distribution of water molecules and of sodium and chloride ions in the pore, in the absence of any other ion. For instance, the two alternate ion binding sites seen in Figures 4.3A and 4.3B (at $z = 18 \text{ \AA}$ and at $z = 24 \text{ \AA}$) correspond to positions at which periplasmic sodium ions and solvent naturally accumulate. Figure 4.3C also shows that water density in the hydrophobic region of the pore (from $z = 0 \text{ \AA}$ to $z = 15 \text{ \AA}$) is significantly less in the closed tetramer than in the closed hexamer, consistent with the higher barrier to permeation of the tetramer.

Na^+ and K^+ ions have very similar permeation energetics, yet they undergo different coordination structures. At the level of the selectivity filter ($z = 18 \text{ \AA}$) in the closed Orai hexamer, the Na^+ ion is typically coordinated by 5 water molecules and one oxygen of an E178 side chain whereas the K^+ ion is typically coordinated by 4 water molecules and two E178 residues. In the closed Orai tetramer, both ions are coordinated by one side-chain oxygen atom of E178 and 5 water molecules. The coordination number goes down as the ions are pushed into the hydrophobic region of the closed pores (from $z = 12 \text{ \AA}$ to $z = 2 \text{ \AA}$). In the hexamer, the Na^+ ion retains an average coordination of 5.4 water molecules despite the V174 residues disrupting its coordination shell, whereas the K^+ ion is coordinated by 5.6 water molecules on average. In the tetramer, the Na^+ and K^+ ions are coordinated by 4.9 and 4.5 water molecules, respectively. This results in a higher free energy barrier for ion permeation through the closed tetramer. In the basic regions of both hexameric and tetrameric channels ($z < 0 \text{ \AA}$), the permeant ions are coordinated

by water molecules and Cl^- ions. In the closed hexamer, Na^+ and K^+ ions around residues K163 ($z = -5 \text{ \AA}$) are coordinated by 3.4 and 2.1 Cl^- ions, respectively. In the closed tetramer, Na^+ and K^+ are coordinated by 0.4 and 1.1 Cl^- ions, respectively. The absence of Cl^- ions between $z = 0 \text{ \AA}$ and $z = -5 \text{ \AA}$ in the basic section of the closed tetramer results in a second free energy peak for Na^+ and a less steep decrease in the free energy for K^+ (see Figure 4.3C). As the permeant ions move along the basic region, more water molecules coordinating them are replaced by Cl^- ions.

The Ca^{2+} ion strongly binds to the extracellular side of the closed channels but does not permeate further down. Their binding positions are different in the hexamer and tetramer closed channels. In the closed hexamer, the Ca^{2+} ion interacts with one of the E178 residues intermittently and also with a D182 residue located in the loop connecting TM1 and TM2 helices. In addition to these residues, 7 water molecules coordinate the ion. Compared to the simulations without the constraint on the coordination number of Ca^{2+} and water, the interactions between the ion and oxygen atoms from the protein less frequently and create a relatively weaker binding affinity for the ion. On the other hand, the Ca^{2+} ion, coordinated by 7 water molecules, always interact with one E178 residue (around $z = 18 \text{ \AA}$). Although rarely, a second E178 residue also comes in contact with the ion. For these interactions, the Ca^{2+} ion does not need to shed water molecules coordinating itself. As a result, the closed tetramer shows a stronger binding affinity to the Ca^{2+} ion.

4.4.4. Ion Permeation through the Open Hexameric and Tetrameric Channels

Figures 4.3D and 4.3E show the free energy profiles for translocating single Ca^{2+} , K^+ and Na^+ ions along the open hexamer and tetramer Orai pores. For both oligomers, the pores are opened by imposing a 30° counter clockwise rotation of the TM1 helices, which allows more water molecules in the hydrophobic region (see Figure 4.3F) and lowers the energy barrier for ion permeation. With the notable exception of Ca^{2+} ion in the hexamer, helix rotation also reduces the affinity for the external binding site: The rotated E178 side chain are high enough to form salt bridges with residues K270 and are less available to stabilize the fully hydrated ion. On average, the Ca^{2+} is coordinated by 8 water molecules and one E178 residue at the binding site. A second E178 residue rarely comes into the solvation shell.

In the open hexamer, the main energy barrier is 7.4 kcal/mol for K^+ and 5.2 kcal/mol for Na^+ . This barrier is located within the basic region for K^+ and between the hydrophobic and basic regions for Na^+ . In the open tetramer, the barriers are 4.0 kcal/mol for both ions. At $z = -10 \text{ \AA}$, the Na^+ ion is coordinated by three water molecules and two Cl^- ions for both open channels (see Table 4.3 for details). In the open hexamer, the K^+ ion is also coordinated by 3.6 water molecules and 2.1 Cl^- ions whereas it is only coordinated by only 3.6 water molecules and 0.7 Cl^- ions within the open tetramer's pore. K^+ requires a higher coordination number [161] and is therefore not as stable as Na^+ at that position in the tetramer channel.

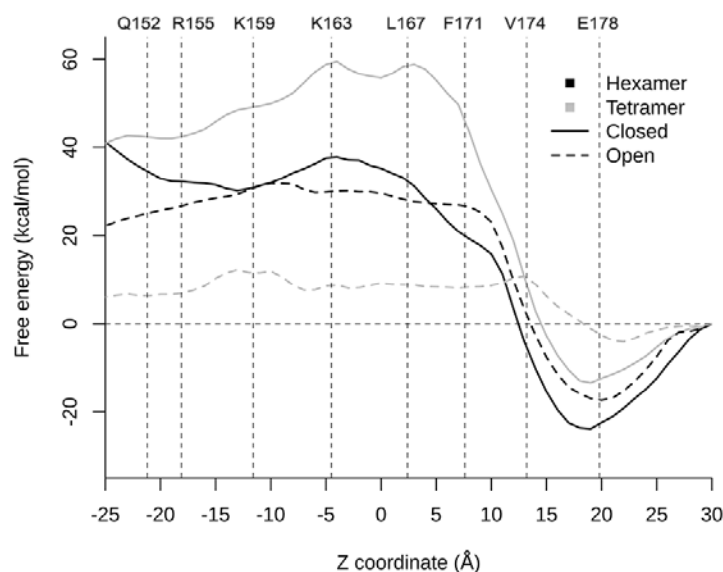


Figure 4.4. Free energy profiles for permeation of a single Ca^{2+} ion through the closed and open Orai multimers. In all graphs, the x -axis represents the z -coordinate of the permeant ion with respect to the center of the pore, whereas the vertical dashed lines represent the average z -coordinate of the side chain atoms of the pore-lining residues (excluding hydrogen atoms). Analysis is done using the 8 ns-long umbrella sampling production trajectories. Unlike for Figure 4.3, molecular dynamics simulations with umbrella sampling are performed without any constraint on the Ca^{2+} -water coordination number (See Table 4.3 for details of the coordination resulting from the simulations).

4.4.4.1. Open Hexamer

Unlike for Na^+ or K^+ , the free energy cost of permeation for Ca^{2+} is dramatically lower in the open hexamer than in the closed hexamer. In the open conformation, the free energy required for Ca^{2+} to reach the ring of L167 side chains is comparable to that of K^+ and Na^+ . For calcium, the profiles reported in Figures 4.3D and 4.3E are obtained by constraining the ion to be coordinated by a minimum of 7 water molecules. This corresponds to the coordination expected in bulk water

[162,163] and we find that not enforcing this minimal water coordination results in higher permeation barriers except for the open tetramer (see Figure 4.4). Although Figure 4.3 reports calcium permeation profiles for a calcium ion with a minimum of 7 water molecules in its first shell, we find similar profiles if the coordination is constrained to a minimum of 6 water molecules (see Figure 4.5). The free energy profile keeps increasing below the L167 ring, once the Ca^{2+} ion reaches the basic region. This increase, however, is largely due to the bias imposed on the Ca^{2+} coordination: By keeping 7 water molecules around the calcium ion at all times, the simulations prevent Ca^{2+} from forming pairs with the Cl^- ions accumulating in that region of the pore, up to the level of the K163 residues (see Figure 4.3F). Ca^{2+} ions are known to interact with Cl^- ions in solution and have been predicted to liberate about 1.1 kcal/mol of free energy per Ca^{2+} - Cl^- pair [164]. Therefore, in the basic region of the pore, the free energy profile is likely going down for $z < 0$ Å, instead of going up.

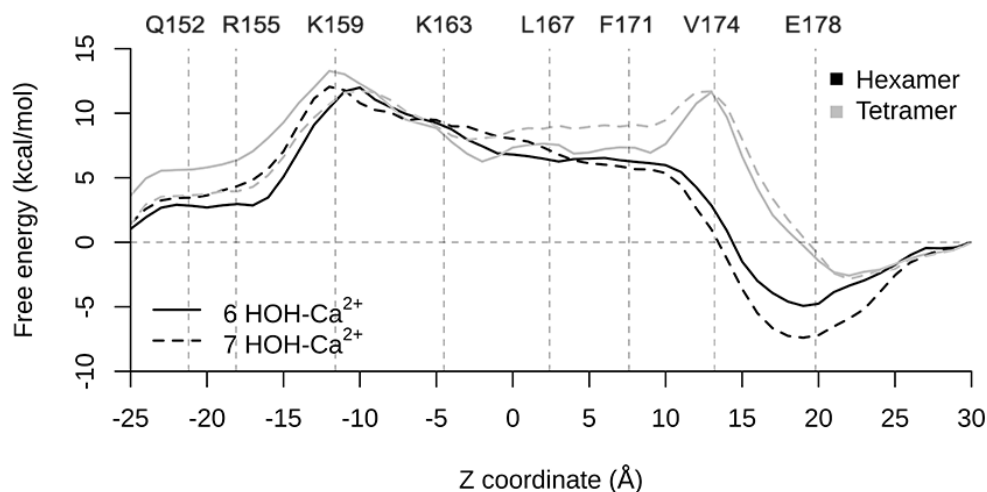


Figure 4.5. Free energy profiles for permeation of a single Ca^{2+} ion coordinated by at least 6 and by at least 7 water molecules, through the open Orai multimers. In all graphs, the x -axis represents the z -coordinate of the permeant ion with respect to the center of the pore, whereas the vertical dashed lines represent the average z -coordinate of the side chain atoms of the pore-lining residues (excluding hydrogen atoms). Analysis is done using the 12 ns-long umbrella sampling production trajectories.

4.4.4.2. Open Tetramer

TM1 helix rotation has a marked effect on the free energy profiles of the tetrameric channel. The extracellular ion binding site in the open conformation of the tetramer is 4 Å higher than in the closed conformation and is shallower. This reflects the fact that, in the open conformation, all

four E178 residues are more solvent-exposed and form transient salt bridges with K270 side chains. Unlike in the closed conformation, a Na^+ or K^+ ion at $z = 18 \text{ \AA}$ in the open conformation is not directly coordinated by the side chains of E178, resulting in weaker binding. Its highest energy peak is located at the entrance of the hydrophobic part of its pore unlike the case of the open hexamer channel (see Figure 4.3E). Along the hydrophobic part, the average number of water molecules coordinating both permeant ions vary similarly (the coordination number of water molecules is 5.4 for Na^+ and 5.6 for K^+). The permeant Na^+ ion, having a coordination of 5.5 in solution, replaces one water molecule with a Cl^- ion at the entrance of the basic part ($z = -5 \text{ \AA}$) while K^+ ion stays hydrated with 6 water molecules. This results in a relatively larger free energy cost for Na^+ permeation. For both ions, the second energy peak occurs at $z = -10 \text{ \AA}$ where they, passing through the side chains of K159 residues, are being coordinated by 3 water molecules and 1.7 Cl^- ions. While the open hexameric structure lets more water into its pore than the open tetrameric structure (see Figure 4.3F), Na^+ and K^+ ions permeate better in the tetramer than in the hexamer (see Figures 4.3D and 4.3E).

On the other hand, the pores of open Orai channels accommodate the permeation of the solvated calcium ion better (See Figure 4.3D and 4.3E). Along the open hexameric Orai pore, the free energy behavior of the solvated Ca^{2+} ion varies similarly to the cases observed for Na^+ and K^+ : The hydrophobic region of the pore poses an energy barrier of 5.9 kcal/mol (located between the F171 and V174 residues). The energy cost increases as the solvated ion moves toward basic part (between K163 and K159). However, the increase in free energy through the basic region is likely to be a side-effect of the coordination number constraint – because of the coordination number constraint, the permeant calcium ion is not permitted to exchange its water molecules with the Cl^- ions stabilizing the basic region. In the case of the open tetrameric channel, the energy barrier of 11.6 kcal/mol occurs at the entrance of the hydrophobic part (V174) and, similarly, the energy cost of being at the basic part gets as high as 13.3 kcal/mol where Ca^{2+} would normally interact with the Cl^- ions (K159). In conclusion, the open tetrameric Orai channel reveals an ion pore significantly selective toward Na^+ and K^+ against Ca^{2+} while the larger pore of the open Orai hexamer seems to pose comparable energy barriers to the permeation of different ions we studied.

4.4.5. Modeling of Calcium Ions for Biomolecular Simulations

Our results draw attention to the need for improved force field parameters for divalent ions such as Ca^{2+} , since these ions are more likely to polarize their surroundings compared to monovalent ions [162,165,166]. For the description of interactions involving divalent ions, it is difficult to find the right balance of attractive-versus-repulsive forces to describe the true nature of interactions between these ions and many ligands [167,168].

We first studied the permeation of a single Na^+ and K^+ ions along the pores of Orai hexamers and tetramers. Following the same simulation procedure for Ca^{2+} simulations, surprisingly, showed that helix rotation reduces the steepness of the free energy peaks significantly in the Orai tetramer. From the extracellular side until halfway through the basic part of the pore, the open tetrameric channel lets Ca^{2+} permeate while being solvated by 7 water molecules. Since the E178 residues form salt bridges with K270 residues, Ca^{2+} can enter the pore of the Orai tetramer without binding to the E178 side chains.

We then repeated our molecular dynamics simulations with umbrella sampling to investigate the free energy profile of Ca^{2+} as coordinated by 6 and by 7 water molecules for all the systems: the closed hexameric and tetrameric Orai channels as well as the open hexameric and tetrameric Orai channels (see Figure 4.5). We chose 6 and 7 water molecules as the ideal cases for Ca^{2+} coordination since they are frequently found in the literature [162,165]. As mentioned earlier, our results must be interpreted cautiously, since our simulation setup is tailored to keep Ca^{2+} -water coordination at 7 and does not allow Ca^{2+} to interact with the Cl^- ions found in the basic region. In reality, Ca^{2+} ions permeating through the Orai pores could easily interact with anions expected to be in the basic region of the Orai pore [11,57]. In addition, Ca^{2+} ions interact with Cl^- ions in solution [164] and are affected by a transmembrane potential, neither of which are considered in our simulations.

As shown in Figure 4.3A and 4.3B, the free energy profiles of Ca^{2+} along the pores of the closed Orai proteins reveal high energy barriers (> 20 kcal/mol). In both closed Orai channels, the initial position of the Ca^{2+} ion solvated with 7 water molecules is identified as the energy minima. As the ion moves further down the pore with its solvation shell, the energy cost increases significantly. On the other hand, the pores of open Orai channels accommodate the permeation of

the solvated Ca^{2+} ion better (see Figure 4.3D and 4.3E). Along the open hexameric Orai pore, the free energy behavior of the solvated Ca^{2+} ion varies similarly to the cases observed for Na^+ and K^+ : the hydrophobic region of the pore creates an energy barrier of 5.9 kcal/mol (located between F171 and V174). The energy cost increases as the solvated ion moves toward basic part (between K163 and K159). However, the increase in free energy through the basic region is likely to be a side-effect of the coordination number constraint – because of this constraint, the permeant Ca^{2+} ion is not permitted to exchange its water molecules with the Cl^- ions stabilizing the basic region. In the case of the open tetrameric channel, the energy barrier of 11.6 kcal/mol occurs at the entrance of the hydrophobic part (V174), and similarly the energy cost of being at the basic part gets as high as 13.3 kcal/mol where Ca^{2+} would normally interact with the Cl^- ions (K159). In conclusion, the open tetrameric Orai channel reveal an ion pore significantly selective toward Na^+ and K^+ against Ca^{2+} , while the larger pore of the open hexameric Orai channel seem to pose comparable energy barriers to the permeation of Ca^{2+} , K^+ and Na^+ .

4.5. Conclusion

In this study, we built model structures of Orai multimers based on the crystal structure of *D. melanogaster* Orai protein. Free energy calculations showed that these models create high energy barriers against ion permeation, confirming that the crystal structure is indeed a closed conformation of the Orai channel. We also tested whether the rotation of pore-forming helices would make the pores of these model channels conductive to Ca^{2+} ions and selective against Na^+ and K^+ ions. We built both Orai multimers (hexamer and tetramer) in an open conformation by rotating their pore-forming helices. The umbrella sampling calculations of these channels showed that helix rotation lowers the energy barrier against ion permeation regardless of the multimeric state of the channel. However, the oligomeric state of the Orai channel makes a difference in the case of Ca^{2+} : the hexamer pore is better adapted to the permeation of a fully-hydrated Ca^{2+} ion than the tetramer pore. When opened, the Orai hexamer reveals comparable free energy profiles for the permeation of Ca^{2+} , K^+ and Na^+ ions. Conversely, the open Orai tetramer shows opposite selectivity, with the permeation of Na^+ and K^+ ions becoming easier than for Ca^{2+} . The opening of the hexameric channel displays changes in relative permeabilities that are consistent with calcium-selective currents. The opening of the hexameric structure barely

makes a difference for the permeation of Na⁺ and K⁺ ions, while opening the tetramer almost completely removes the barrier for these ions.

Calcium coordination with proteins is notoriously difficult to simulate using conventional protein force fields, since Ca²⁺ ions, due to their high charge density, are more likely to polarize their environment compared to the monovalent ions Na⁺ and K⁺ [167]. Fortunately, our simulations suggest that the details of coordination with protein side chains are not as important, since the hydrophobic environment of the Orai pore facilitates calcium permeation by simply accommodating its complete hydration shell.

As a highly selective calcium channels, Orai proteins form an unusual permeation pathway for Ca²⁺ ions. Due to low extracellular concentrations of these ions, Orai proteins must show a high calcium selectivity to function. Like other calcium channels, they also have a selectivity filter formed by a ring of glutamate residues. For example, the selectivity filter of voltage-gated calcium channels is formed by a conserved EEEE locus known to be responsible for their selectivity of Ca²⁺ over Na⁺ ions [170,171]. At the extracellular mouth of the Orai pore, there are two aspartate residues (D182 and D184) in the loop of each Orai monomer, in addition to the selectivity filter formed by E178 residues. These residues can attract Ca²⁺ ions that would electrostatically repel monovalent ions. As proposed for eukaryotic calcium channels [169], the selectivity filter of the Orai channel might be occupied by one or more Ca²⁺ ions that guard the pore against monovalent ions. The importance of glutamate residues is also supported by experimental data. A mutation in the selectivity filter, changing the glutamate to an aspartate (E178D corresponding to E106D in *H. sapiens* Orai1), lowered calcium selectivity, whereas mutating E178 to A or C caused loss of calcium selectivity [45,155].

Past the selectivity filter, there is a hydrophobic part to the Orai pore. As suggested by our results, a residue in this part (V174) plays a vital role in channel gating. This is further supported by functional studies of Orai mutants. Similarly, mutations in the hydrophobic part in the pore (V174 and F171 to polar or mildly hydrophobic residues) resulted in leaky channels [49,67]. The presence of a hydrophobic domain in the pore draws attention to the possibility of the permeant ion being hydrated, since this hydrophobic region does not provide any polar moieties to coordinate the ion. After the hydrophobic part, the Orai pore has a region lined with basic

residues (K163, K159 and R155). This unusual basic part is thought to be stabilized by anions in the closed conformation [11]. In an open conformation, this basic domain could create a local concentration of positive charges, and hence lower permeation rate by electrostatically repelling the permeant cation. Ctr1, a copper transporter whose crystal structure was recently determined, also has a basic cavity below its selectivity filter which was suggested to play a role in its low conductance [172]. The same could be the case for the Orai channel. Following the hydrophobic part, the basic residues in the Orai pore might be responsible for its extremely low conductance, which was estimated to be around 10-30 fS in 2-100 mM Ca^{2+} [154].

There are two major ideas on how Orai channels are gated by STIM: via the pore dilation in the basic region [11], or through helix rotation as a mechanism of hydrophobic gating [67]. The latter is supported by various experimental studies. A recent study showed that a single mutation in the hydrophobic part of the Orai pore (V174A) creates an open channel in the absence of STIM [137]. Yamashita et al. concluded that STIM-mediated channel activation rotates the pore helices and increases pore hydration involving V174 and F171 residues [67]. In addition, Dong et al. computationally investigated ion permeation through the wild-type and V174 mutant Orai channels and emphasized the importance of pore waters for ion permeation [58]. Finally, Gudlur et al. used disulfide cross-linking to probe how STIM binding alters the conformation of pore helices and concluded that the conformational rearrangement occurs at the extracellular mouth of the Orai pore [137]. Together with these studies, our results support the idea of hydrophobic gating. In every case we explored, there is an energy barrier within the hydrophobic part of the pore. Especially considering the tight-packing in the hydrophobic part, a pore dilation in the basic part might not alter the energy barrier created by the hydrophobic part even in the structures with rotated helices. Helix rotation significantly lowers the hydrophobic energy barrier in the hexamer and tetrameric Orai pores without altering the size of their basic domains.

Chapter 5. Modeling the Effect of Salinity on the Cytoplasmic C-Terminal Domain of Osmolyte Transporter ProP

5.1. Abstract

Increases in osmotic pressure threaten cells with dehydration. Osmosensing transporters prevent this by detecting increases in osmotic pressure and respond by mediating organic solute uptake. In *Escherichia coli* (*E. coli*), osmosensing transporter ProP activates when cellular dehydration elevates cytoplasmic cation concentration, modulating electrostatic interactions. In our previous work, molecular dynamics simulations have suggested that the cytoplasmic C-terminal domain (CTD) of monomeric ProP either associates with the membrane surface, or forms an antiparallel, homodimeric alpha-helical coiled-coil with an adjacent ProP. We then proposed that the coiled-coil formation prevents the CTD-membrane association, and therefore locks ProP in an active conformation. In this work, we aim to understand what drives the CTD-membrane disassociation as salt concentration increases. We used homology modeling to create a model system of ProP including the CTD and the Transmembrane Helix XII (TMXII). Since there was no template available for the loop connecting the CTD to TMXII, we performed molecular dynamics simulations combined with the adaptive biasing force method in order to examine the possible conformations of the loop and the effect of salinity on these conformations. To investigate how salt concentration alters the intramolecular interactions of CTD and intermolecular interaction between CTD and lipid, we performed molecular dynamics simulations of the CTD with and without TMXII, at different salt concentrations: 0 M KCl (only counter ions), 0.25 M KCl and 0.5 M KCl. Our data identify how salt affects the relevant interactions within ProP as well as between ProP and the membrane; and also complement biochemical analyses of ProP sequence variants to further develop our structural model for osmosensing.

5.2. Introduction

Changes in extracellular osmotic pressure alter the hydration of prokaryotic and eukaryotic cells because phospholipid membranes are highly water permeable, but solute-impermeable. In response to variations in osmotic pressure, cells maintain cellular hydration, growth and survival through several mechanisms [173]. Channels and transporters residing in the cell membrane constitute this osmoregulatory system. ProP of *E. coli* is an osmosensing transporter which

detects the increasing cytoplasmic cation concentration that results from cellular dehydration, responds by pumping osmolytes into cells, and therefore forestalls dehydration [80]. It catalyzes proton-osmolyte symport via an alternating access mechanism (see Figure 1.5). ProP activity is a sigmoid function of the osmolality in intact cells and in proteoliposomes reconstituted with the purified protein [80].

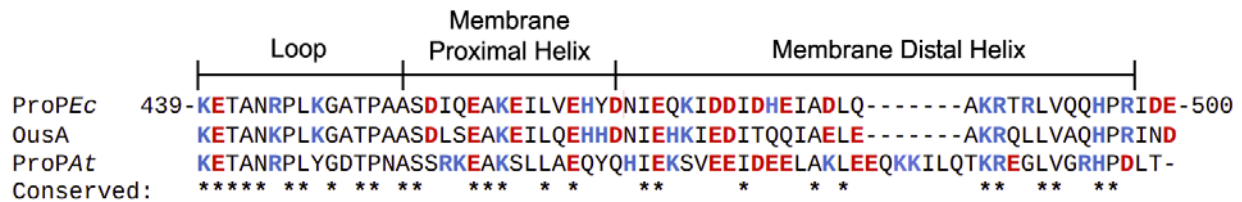


Figure 5.1. The alignment of the sequences of the cytoplasmic C-terminal domains (CTDs) of the ProP orthologues from *E. coli* (ProPEc), *Dickeya dadantii* (OusA) and *Agrobacterium tumefaciens* (ProPAI) were done with CLUSTALW [174] by using the full length sequences. These proteins function as osmoregulatory transporters [78,91,175]. The illustrated ProPEc segment includes residues K439-E500. Experimental data show that M438 of ProPEc is intramembrane, at the cytoplasmic end of TMXII [176]. Here, acidic residues (D, E) are red and basic residues (H, K, R) are blue. Conserved residues are marked with asterisks (*). Residues in the membrane distal part form the antiparallel coiled-coil [85].

ProP is a 500 amino acid residue Major Facilitator Superfamily member, embedded in the cytoplasmic membrane, with 12 transmembrane helices (TMs) and an extended, cytoplasmic C-terminal domain (CTD) [84]. The CTDs of adjacent ProP molecules form antiparallel, homodimeric alpha-helical coiled-coils: Zoetewey et al. [85] determined the NMR structure of the coiled-coil using peptides corresponding to the residues 468-497 of ProP (the membrane-distal portion of the CTD helix) and Hillar et al. [84] used chemical cross-linking to demonstrate the antiparallel association of the CTDs in full length ProP, in vivo. No secondary structure is predicted for residues 439-454, whereas the rest of the CTD (residues 455-500) is predicted to be alpha-helical. In two other studies [90,91], experiments and molecular dynamics simulations showed that a peptide corresponding to the CTD of ProP (residues 439-500) can either form a coiled-coil dimer or associate as a monomer with the membrane surface. Culham et al. further showed that increasing osmolality decreases the membrane fluidity in *E. coli* lipid liposomes [91]. In addition, the osmolality response of ProP is modulated by the proportion of anionic phospholipids in its host membrane [90,175]. All of these observations led us to compare (1) the

osmolality dependence of the activities of ProP sequence variants and (2) interactions between corresponding peptides and liposomes to propose a model for osmosensing in our previous work (see Figure 1.5) [91].

According to this model, CTD-membrane association locks the transporter in an inactive conformation. That association is destabilized when cytoplasmic cation concentration increases as a result of increasing osmolality. This increase in cytoplasmic cation concentration decreases membrane fluidity. The CTD is released, activating the transporter. Coiled-coil formation then stabilizes the active conformation. In principle, the increase in cation concentration could result in the folding or assembly of the CTD; an increase in local charge density on the membrane surface; and contact of the CTD and membrane surfaces during activation [88]. Here, we aim to test these hypotheses using molecular dynamics.

The NMR structure [85] for the homodimeric coiled-coil provides a starting point for molecular dynamics simulations. Using the NMR structure as a template, we built a homology model of the CTD and performed molecular dynamics simulations at different salt concentrations in order to study the impact of increasing salinity on the peptide-peptide and peptide-membrane salt bridges. New insights regarding the salt dependence of the CTD-membrane association emerged from the molecular dynamics simulations of the CTD model structure that includes the external loop 6 and the transmembrane helix XII (TMXII).

5.3. Computational Details

5.3.1. Building Model Structures of the *E. coli* ProP CTD

As explained in our previous work [91], a homology model of the monomeric C-terminal domain (CTD) of ProP (residues 439-500) was generated with Modeller [97], using the NMR structure of the coiled-coil dimer of the *E. coli* ProP [85] (PDB ID: 1R48) as a template. The helices A and B from the NMR structure were used to model residues 468-497 and 454-483, respectively, whereas there was no available template for residues 439-453. The peptide was oriented on the membrane surface using the Positioning of Proteins in Membrane 2.0 web server (PPM) [138].

CHARMM-GUI Membrane-Builder [140] was used to generate all the simulation boxes including a monomeric ProP CTD peptide (residues 439-500), a pre-equilibrated palmitoyl

(16:0)/palmitoleoyl(16:1) phosphatidylethanolamine and palmitoyl(16:0)/palmitoleoyl(16:1) phosphatidylglycerol (PEPG 80:20) membrane, water and salt (KCl). More specifically, three simulation systems were built; one simulation box contained 0 M KCl (only counter-cations were added to neutralize the net charge in the simulation system) and the other simulation boxes contained 0.25 M KCl and 0.5 M KCl, respectively. The resulting hexagonal simulation boxes ($a = b = c = 111 \text{ \AA}$) and consisted of ~ 106800 atoms (see Table 5.1).

The CHARMM36 [110] force field and the TIP3P [141] water model were used. The molecular dynamics simulations were performed using NAMD 2.9 [145]. Temperature (298.15 K) and pressure (1 atm) were kept constant using Langevin dynamics with a coupling coefficient of 1 ps^{-1} and using a Nosé-Hoover Langevin piston [108,109] with a piston period of 50 fs and a piston decay of 25 fs. All bonds involving hydrogen atoms were constrained using the SHAKE/RATTLE algorithm [142]. Nonbonded interactions were calculated using Particle Mesh Ewald [143] and the recommended CHARMM cut-off scheme [144]. Timestep was set to 2 fs. All simulation systems were relaxed using the six-step scheme in the NVT ensemble as suggested by Jo et al. [140] and simulated for 100 ns in the NPT ensemble.

Table 5.1. Number of lipid molecules, salt ions, water molecules and total number of atoms in the simulation boxes

Systems	$N_{PE,upper}$	$N_{PG,upper}$	$N_{PE,lower}$	$N_{PG,lower}$	N_{K^+}	N_{Cl^-}	N_{water}	N_{atoms}
ProP peptide (439-500) at 0 M KCl	128	32	128	32	76	0	21862	105870
ProP peptide (439-500) at 0.25 M KCl	128	32	128	32	153	77	22115	106783
ProP peptide (439-500) at 0.5 M KCl	128	32	128	32	268	192	22115	107013
ProP peptide (412-500) at 0 M KCl	136	34	128	32	73	0	17104	92197
ProP peptide (412-500) at 0.25 M KCl	136	34	128	32	149	76	17046	92175
ProP peptide (412-500) at 0.5 M KCl	136	34	128	32	226	153	17052	92347

5.3.2. Investigating the conformational dynamics of the loop

In the simulations of ProP 439-500 systems, the loop (residues 439-450), generated without a template in Modeller [97], often flipped back toward the CTD and moved, freely, toward the solution. In other words, the loop structure did not experience its physiological environment during the simulations with our initial model of the CTD helix. Since this loop (residues 439-

450) normally connects the CTD helix with TMXII, in a complete ProP structure, it would be constrained by TMXII and also by the membrane association of residues 454-500. In addition, the loop can adopt different conformations as a response to changes in salt concentration.

To explore how salt concentration affects the dynamics of the loop, we (1) removed the CTD helix (residues 451-500) from our ProP model (439-500); (2) neutralized the N and C termini of the peptide formed by the residues 439-450 (a neutral acetylated N-terminus and a neutral N-methylamide C-terminus, respectively); and (3) solvated by adding water and 0.5 M KCl. Using CHARMM-GUI [139], an octahedral simulation box ($a = b = c = 58 \text{ \AA}$) was generated. The resulting simulation box consisted of a total of ~ 14000 atoms. Molecular dynamics simulations were performed with the same parameters as explained in the previous section. Molecular dynamics enhanced with the adaptive biasing force method (ABF) [127] was used to generate the free energy profile as a function of the distance between the C_α atoms of residues 439 and 450 (i.e. the end-to-end distance of the loop). During the ABF calculations, the lower and higher limits to the end-to-end distance were set to 3 and 30 \AA , respectively. The upper and lower wall constants were set to 10 kcal/mol/ \AA^2 . The width for the end-to-end distance was set to 1 \AA . 500 samples of the instantaneous force acting along the end-to-end distance were collected before the estimation of the average force. The simulation was performed for 300 ns to ensure the convergence of the estimation of free energy. This simulation was repeated at three different salt concentrations: 0 M (counter ions only), 0.25 M and 1 M KCl, to investigate the effect of salt on the dynamics of the loop. Each ABF calculation, at different salt concentrations, generated an estimation of free energy as the end-to-end distance of the loop changes. All of these calculations showed that a hairpin-like conformation of the peptide (residues 439-450) with an end-to-end distance of 4 \AA corresponded to the free energy minimum. Therefore, this conformation was used as a template to generate a longer, more realistic model of the ProP peptide (see the Next section).

5.3.3. Building a more realistic model of the ProP peptide

To generate a model structure of a longer ProP peptide, external loop 6 (residues 412-418) and transmembrane helix XII (TMXII) (residues 419-438) were modeled and attached to the CTD (residues 439-500). The protein homology/analogy recognition engine 2.0 (Phyre) server [177] was used to generate a homology model of ProP based on the crystal structure of bacterial xylose

transporter, XylE from *E. coli* (PDB ID: 4GBZ) [178]. The Phyre homology model (for the residues 412-438), a representative conformation of the loop (residues 439-450) based on the ABF simulation trajectories giving the lowest free energy, and the simulated structure from our previous work [91] (for the residues 451-500) were connected together with Modeller [97] to create a ProP peptide formed by the residues 412-500. The same simulation setup was repeated for this peptide. Counter cations (87 K⁺ ions) were added to this simulation box to neutralize the system. A hexagonal box ($a = b = 121 \text{ \AA}$ and $c = 122 \text{ \AA}$) consisted of 29856 water molecules, 405 lipid molecules (PEPG (80:20)) and 1415 peptide atoms resulting in a total of 139427 atoms. The ProP peptide (residues 412-500) was simulated for 100 ns with a harmonic constraint on the loop; the distance between the C_α atoms of the residues 439 and 450 was kept at 5 Å, with a force constant of 2.5 kcal/mol/Å².

The atomic coordinates to the ProP peptide (residues 412-500) at the end of 100 ns were used to set up three simulation systems: the ProP peptide (412-500) embedded into the PEPG (80:20) membrane at 0 M (only counterions), 0.25 M and 0.5 M KCl. In these systems, the loop (residues 439 and 450) was unconstrained. The procedure as explained in Section 5.3.1 was repeated for the simulation setup. The hexagonal simulation boxes ($a = b = 110 \text{ \AA}$ and $c = 99 \text{ \AA}$) consisted of ~93000 atoms (see Table 5.1 for further details). Using NAMD 2.9 [145], unbiased molecular dynamics simulations were performed for 100 ns.

The simulation trajectories were analyzed using different tools: Bio3D [147] was used for the calculation of side-chain contacts, MDAnalysis [148,149] for the computation of hydrogen bonds, and VMD [150] for the rest of the analysis. Throughout these analyses, two molecules were assumed to be in contact (or interacting), if the distance between a pair of their non-hydrogen atoms was shorter than or equal to 5 Å. The graphs were plotted with the ggplot2 package in R [151].

5.4. Results and Discussion

5.4.1. What can Molecular Dynamics Simulations of the ProP CTD Tell Us?

The initial structure of the ProP CTD peptide (residues 439-500) was generated by Modeller as explained in our previous work [91] (see Figure 5.2A). Molecular dynamics simulations of the

peptide, oriented on a PEPG membrane surface using the PPM server [138], were performed at 0 M KCl (only counter ions were added to neutralize the net charge of the system), 0.25 M KCl and 0.5 M KCl. These salt concentrations were chosen to cover the range relevant for ProP activation which is a sigmoid function of the osmolality in proteoliposomes reconstituted with the purified protein [89]. The alpha-helix, formed by the residues P451-Q494, remained stable throughout these simulations. The root mean square deviation (RMSD) of all backbone atoms in the helical part of this peptide was calculated as $2.0 \text{ \AA} \pm 0.5 \text{ \AA}$ at 0 M KCl, $1.4 \text{ \AA} \pm 0.4 \text{ \AA}$ at 0.25 M KCl, and $1.6 \text{ \AA} \pm 0.4 \text{ \AA}$ at 0.5 M KCl, with respect to the initial structure.

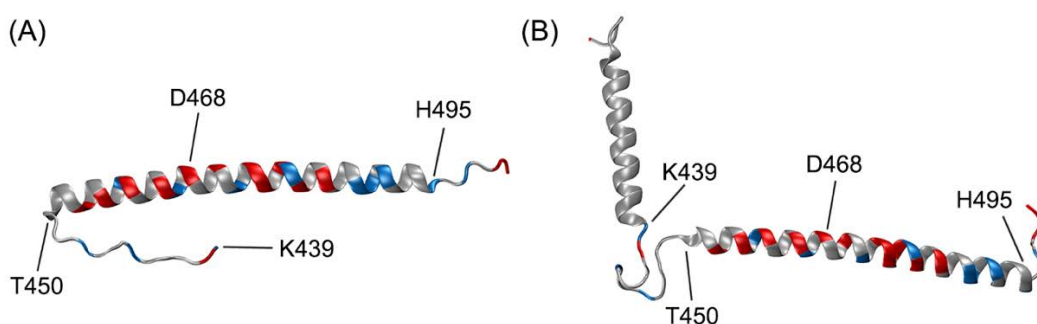


Figure 5.2. (A) Initial structure of the ProP CTD peptide formed by residues 439-500 (short peptide). The acidic residues (D and E) are shown in red whereas the basic residues (H, K and R) are represented in blue. The rest of the peptide is colored gray. The loop is formed by residues 439-450. Residues 451-467 are known as the membrane proximal helix, whereas the residues 468-495 are the membrane distal helix, which forms the coiled-coil. The cartoon representation of the peptide was generated with VMD [150]. (B) Initial structure of the longer ProP peptide formed by residues 412-500 (long peptide).

Molecular dynamics simulations showed that the ProP peptide maintained stable side-chain contacts and hydrogen bonds. Although a change in salt concentration did not significantly alter the average number of side-chain contacts or hydrogen bonds within the peptide, more salt ions interact with the peptide as salinity increases. More interactions with K^+ ions are expected since the peptide is overall anionic (see Figure 5.2A). At 0.25 M and 0.5 M KCl, the basic residues of the peptide interacted with a few Cl^- ions. The total number of lipid molecules interacting with the peptide did not significantly vary as the salinity changed. However, as salt concentration increased, the CTD interacted less with PE lipids, and more with PG lipids (see Table 5.2).

Table 5.2. Intra-peptide CTD contacts (side-chain contacts and hydrogen bonds) and average number of salt ions and lipid molecules interacting with the CTD

Simulations	[KCl]	$N_{sc\text{-contacts}}$	N_{Hbonds}	N_{K^+}	N_{Cl^-}	N_{PE}	N_{PG}
450-500 from the short peptide (439-500)	0 M	43 ± 3	66 ± 5	3 ± 1	-	20 ± 3	6 ± 1
	0.25 M	42 ± 4	64 ± 4	5 ± 2	0 ± 1	18 ± 2	9 ± 1
	0.5 M	43 ± 4	62 ± 4	7 ± 2	1 ± 1	15 ± 2	10 ± 1
450-500 from the long peptide (412-500)	0 M	39 ± 4	62 ± 4	4 ± 2	-	16 ± 3	6 ± 2
	0.25 M	40 ± 3	60 ± 5	7 ± 2	1 ± 1	20 ± 2	4 ± 1
	0.5 M	40 ± 4	60 ± 5	8 ± 2	2 ± 1	17 ± 2	3 ± 2

A contact (or interaction) was counted only if the distance between a pair of non-hydrogen atoms was less than 5Å. This analysis was done, using the 100 ns-long trajectories, for two different ProP systems at 0 M, 0.25 M and 0.5 M KCl: the short ProP peptide formed by the residues 439-500 and the long ProP peptide formed by the residues 412-500. In both cases, only the contacts involving the CTD helix (residues 450-500) were taken into account. The calculation of the side-chain contacts excluded the contacts within the same residue and between a residue and two residues sequentially following that residue.

Figure 5.3 shows the fraction of simulation time each ProP residue spent forming a contact with a lipid head group (the probability of a contact). In Figure 5.3A, these contacts are ranked according to their probability of contact. The area under these curves represents the amount of contacts between the peptide and lipids at each salt concentration. The peptide formed more contacts with the lipid head groups and these contacts were maintained through the whole simulation time (the probability of formation was 1) at 0.25 M KCl. At 0 M and 0.5 M KCl, similar residues interacted with the lipid head groups and the probabilities of these contacts were also comparable.

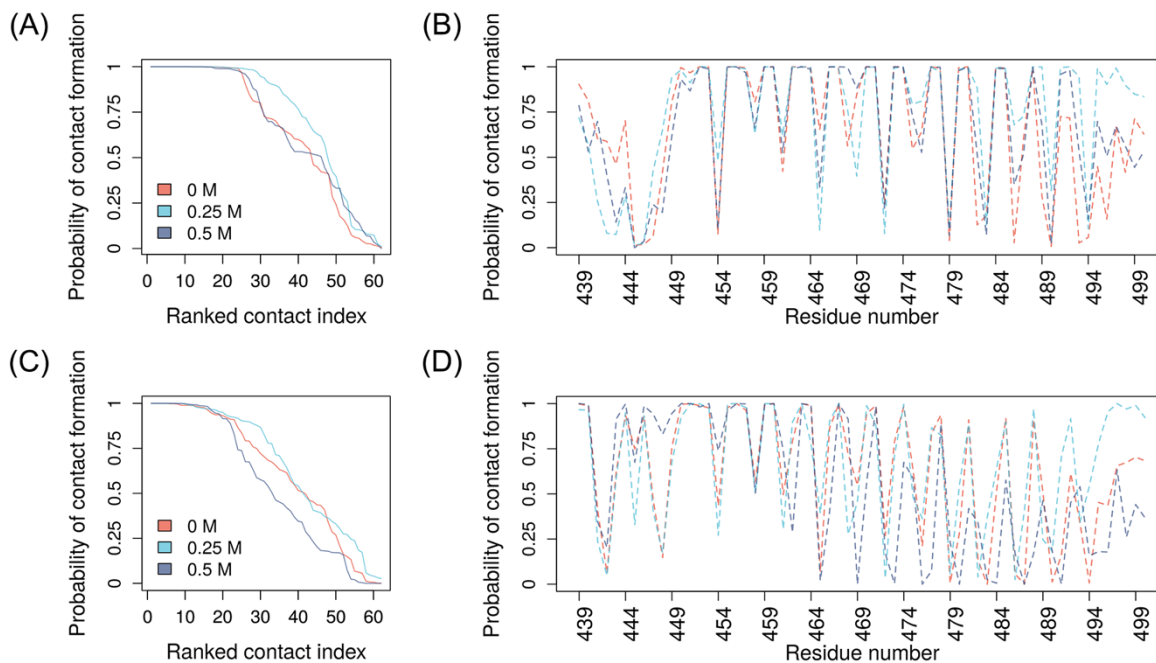


Figure 5.3. (A, C) Contacts between a residue and a lipid head group ranked by their fraction of simulation time for which the contact was formed. (B, D) The fraction of simulation time for a contact with the lipids per residue. A lipid molecule and a ProP residue were considered to be in contact if the distance between any non-hydrogen atom of the peptide and a non-hydrogen atom of the lipid was not larger than 5 Å. 100 ns-long unbiased molecular dynamics trajectories were used for the analysis. Graphs in A and B show the data for the short ProP peptide formed by residues 439-500 whereas the ones in C and D represent the data for the same portion of the peptide (residues 439-500) from the simulations of the longer ProP peptide (formed by residues 412-500).

Since Culham et al. [88] proposed that Coulombic effects are crucial for ProP activation, it is important to explore the nature of the intra-peptide contacts formed by the CTD. Salt bridges, which occur between oppositely charged residues that are close enough (≤ 5 Å) to each other, can be analyzed to probe Coulombic effects. Figure 5.4A shows the salt bridges formed within the short ProP peptide (439-500). At 0 M KCl, the peptide formed five salt bridges, involving residues R444, K447, E458, E461, E465, D476 and K473, occurring at least half of the simulation time. This number went down to three at 0.25 M and two at 0.5 M KCl. At high salt concentrations, fewer residues were involved in forming salt bridges. With increasing salinity, more salt ions interacted with the peptide, and therefore screened the electrostatic interactions within the residues (see Table 5.2). In addition, most of these salt bridges were formed by the loop residues (439-450) flipping back toward the membrane proximal helix (residues 454-468), and therefore are unlikely to occur in the full ProP structure. In ProP, this loop would connect the

CTD to the transmembrane helix XII (TMXII). Without TMXII, the loop becomes unnaturally unconstrained, forming salt bridges with the helical part in the CTD. Therefore, the short peptide with its free loop is not likely to portray the true nature of the system. In fact, the loop might hinder the possible interactions within the peptide and/or between the peptide and the lipid.

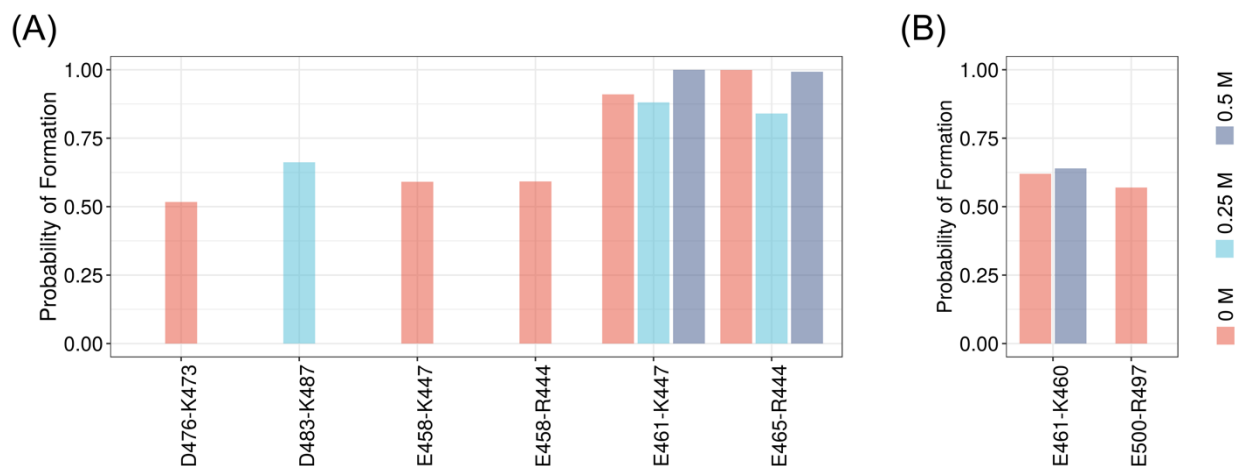


Figure 5.4. (A) Intra-peptide salt bridges calculated from the molecular dynamics simulations of the short ProP peptides including the residues 439-500. (B) Intra-peptide salt bridges, formed by the residues (439-500), calculated from the molecular dynamics simulations of the long ProP peptide (residues 412-500). The *x* axis represents the residue pairs forming a salt bridge, whereas the *y* axis shows the probability of formation of each salt bridge, calculated as the fraction of simulation time at which the distance between the atoms, forming each salt bridge, was smaller than 5 Å. The bars are colored according to the salt concentration at which the simulations were performed.

5.4.2. Residues 439-450 Form a Salt-Sensitive Loop.

The short ProP peptides analyzed so far are formed by the residues 439-500, and therefore include this loop and the CTD helix. However, in order to examine the interactions within the CTD and between the CTD and membrane, the loop must be modeled carefully. One step further toward a more realistic model of the ProP CTD would be constraining the loop with a transmembrane helix so that it behaves like in its native-like environment. Restraining the loop with TMXII would allow a better evaluation of not only the intra-peptide salt bridges but also the salt bridges between the peptide and lipid head groups.

Before generating a homology model of a longer ProP peptide (residues 412-500) including the external loop 6 and TMXII, a variety of conformations of the loop (residues 439-450) that might be accessible to the ProP peptide (residues 412-500) were explored by molecular dynamics simulations enhanced with the adaptive biasing force method (ABF) [127]. These simulations were performed on the loop in solution under four different salt concentrations: 0 M, 0.25 M, 0.5 M and 1 M KCl. Figure 5.5A shows the estimated free energy of the system as a function of the end-to-end distance of the loop (defined as the distance between the C α atoms of the K439 and T450 residues). Regardless of salt concentration, the free energy minimum was located at the end-to-end distance of 4 Å and corresponded to a hairpin conformation of the loop (see Figure 5.5B). Our results indicated that the loop is more resistant to extension as the salt concentration increases. Only at 0.25 M KCl, the loop was more likely to extend up to 10 Å (< 1 kcal/mol of free energy cost).

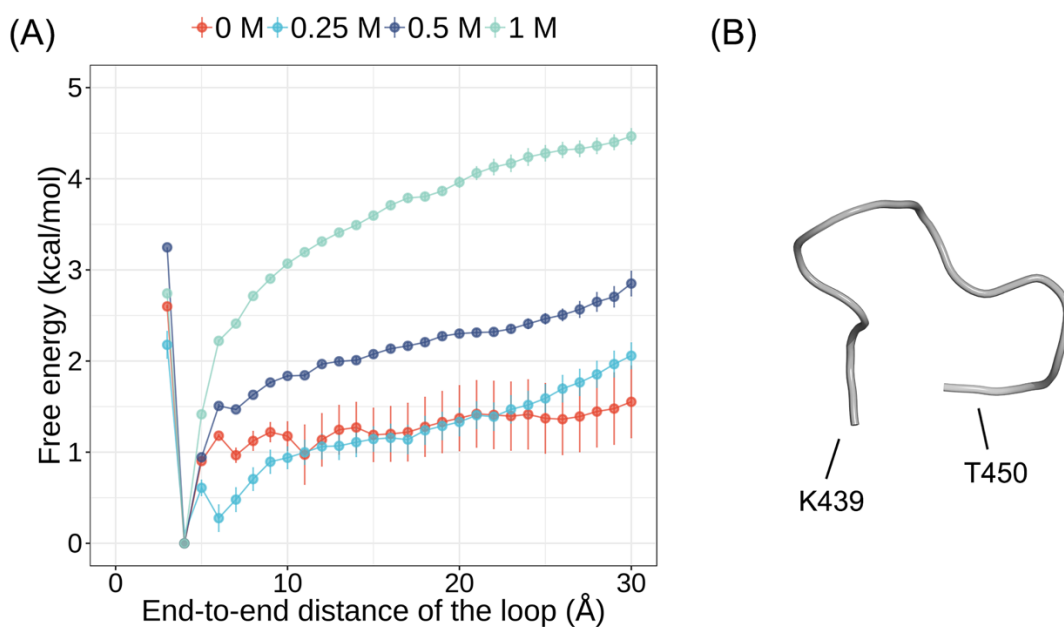


Figure 5.5. (A) Free energy profiles of the loop in solution under different salt concentrations: 0 M, 0.25 M, 0.5 M and 1 M KCl. The x axis shows the end-to-end distance of the loop defined as the distance between the C α of K439 and T450. The y axis represents the free energy estimation. The 300 ns-long ABF simulations were divided into 10 ns-long sub-trajectories. The first 150 ns of these simulations were excluded. For each system, the free energy was calculated as the average of the free energy values coming from all sub-trajectories in the last 150 ns-long ABF simulation. The error bars show the standard deviation of these average values. (B) A representative hairpin conformation taken from the ABF simulation at 0.5 M KCl.

5.4.3. The dissociation of the CTD-lipid does not require a significant conformational change in the peptide.

We used the conformation corresponding to the free energy minimum in the ABF simulation at 0.5 M KCl and built a longer ProP peptide which includes the TMXII and the external loop 6. This representative hairpin conformation of the loop (residues 439-450) is shown in Figure 5.5B. The template for TMXII was a homology model of the ProP transporter, generated by the Phyre2 server [177] and was based on a crystal structure of xylose transporter XylE of *E. coli* [178] (PDB 4GBZ). To assemble the TMXII and the external loop 6 with the short ProP peptide (residues 439-500), we used Modeller. The resulting homology model of the longer ProP peptide was from the residues 412-500 as shown in Figure 5.2B (see Methods for further details). The TMXII part of this peptide was embedded into a pre-equilibrated PEPG membrane with the PPM server [138]. A new set of molecular dynamics simulations was performed for 100 ns at 0 M, 0.25 M and 0.5 M KCl. The secondary structure of the peptide was stable through these simulations: the alpha-helical transmembrane helix (residues M418-M438) followed by the loop (K439-T450), and then a stable alpha-helix (residues P451-Q494). The root mean square deviation (RMSD) of all backbone atoms in the helical parts of this peptide was calculated as $2.4 \text{ \AA} \pm 0.8 \text{ \AA}$ at 0 M KCl, $3.7 \text{ \AA} \pm 1.0 \text{ \AA}$ at 0.25 M KCl and $2.9 \text{ \AA} \pm 0.9 \text{ \AA}$ at 0.5 M KCl with respect to the initial structure. In all three simulations, the end-to-end distance of the loop was unconstrained and remained within 5.7-6.2 \AA .

Table 5.2 shows the average numbers of intra-peptide, peptide-salt and peptide-lipid contacts calculated from the simulations of the long ProP peptide (412-500). In order to compare these results with the existing data from the short peptide, the contacts were counted only when they involved the residues 450-500, forming the helical part of the CTD. Compared to the short peptide, the long peptide also maintained steady side-chain contacts and hydrogen bonds within itself. Interestingly, molecular dynamics simulations of the longer peptide revealed differences in the peptide-salt ion and peptide-lipid contacts compared to those of the short peptide. More salt ions interacted with the peptide throughout the simulations at 0.25 M and 0.5 M KCl. The decrease in the number of PE lipids in contact with the peptide was less pronounced for the long peptide while the number of PG lipids interacting with the CTD decreased with increasing

salinity. The simulations of the peptide formed by residues 412-500 indicated that an increase in salt concentration disrupts some of the interactions between the CTD and the lipid membrane.

Figure 5.3B shows that the interactions between the lipids and the membrane distal part of the CTD (residues 468-500) decreased progressively as salt concentration increased. Interestingly, this decrease cannot be explained in terms of intra-peptide or peptide-lipid electrostatic interactions. In fact, the simulations of the long peptide model not only constrained the loop with TMXII – preventing it from forming salt bridges with the CTD – but also showed that no new salt bridges emerged within the peptide. Therefore, the number of stable salt bridges significantly decreased in this peptide regardless of salinity in the simulations. Figure 5.4B shows that a stable salt bridge, formed by R497 and E500, was identified only at 0 M KCl. In this simulation as well as the one at 0.5 M KCl, the peptide formed a second salt bridge between the adjacent residues K460 and E461. However, this interaction occurred between a pair of adjacent residues. Therefore, the simulations of both peptides infer that intra-peptide salt bridges are not the driving force in the activation mechanism of ProP.

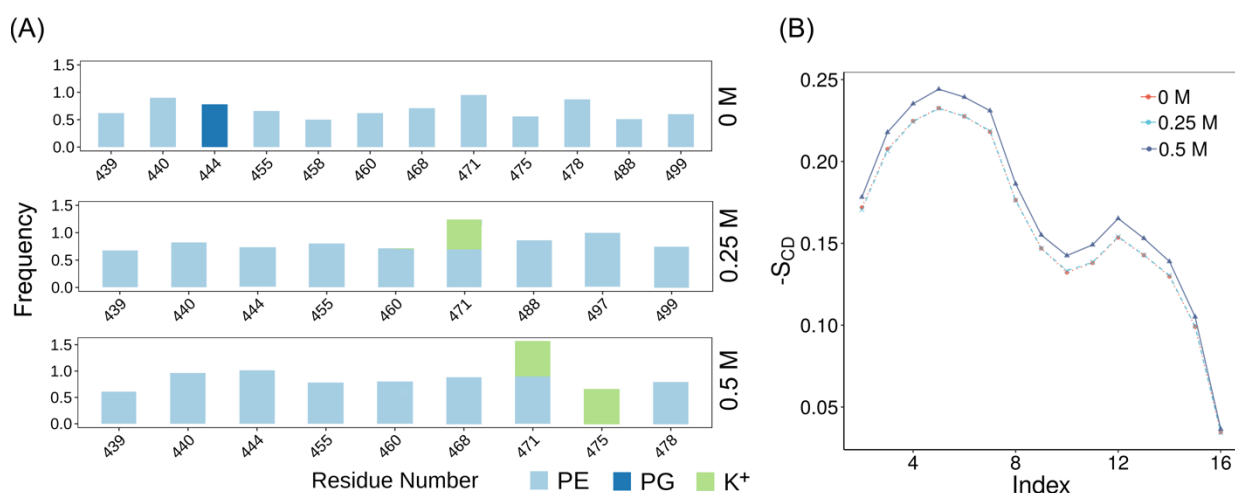


Figure 5.6. (A) The salt bridges between the ProP peptide (412-500) and the lipid head groups. Frequency was calculated as the fraction of the simulation time during which at least one salt bridge between a ProP residue and a lipid molecule (or a K⁺ ion) was formed. Here, only the salt bridges with frequencies higher than 0.5 are shown. The cut-off distance for a salt bridge was set to 5 Å. (B) The order parameter of the lipids at 0 M, 0.25 M and 0.5 M KCl. The calculation was performed with MEMPLUGIN [179] from the 100 ns-long molecular dynamics simulations.

Figure 5.6A shows the frequencies with which one or more salt bridges formed with the lipid head groups and acidic or basic residues in the peptide. The peptide formed salt bridges dominantly with PE lipids. There were only two instances where a residue formed two simultaneous salt bridges with PE lipids: R497 at 0.25 M KCl and R444 at 0.5 M KCl. Neither of these residues is a part of the alpha-helix of the CTD (see Figure 5.1). At 0 M KCl, eight residues (the first half from the membrane-proximal part of the CTD helix (D455, E458, K460 and D468) and the second half from the membrane-distal part of the CTD helix (E471, D475, D478 and R488)) formed salt bridges with a PE head group (see Figure 5.1). At 0.25 M, only four helical residues from each part of the CTD helix (D455 and K460 from the membrane-proximal part and E471 and R488 from the membrane-distal part) were involved in forming at least one stable salt bridge with the PE head groups. One of these residues, E471, also interacted with K^+ ions. At 0.5 M KCl, more acidic residues interacted with K^+ ions (see Figure 5,6A). Among those residues E471 formed the most frequent electrostatic interactions with PE head groups and K^+ ions. Even though the peptide includes the side chains of basic residues as shown in Figure 5.2, none of the CTD residues formed stable salt bridges with PG head groups at higher salinity. This could be a result of the net negative charge of the peptide and/or the changes in the membrane fluidity.

Increasing salt concentration weakens the association of the peptide and the lipid. This is not due to a conformation change in the peptide. In fact, the increase in the salt concentration causes the disassociation of the CTD and the membrane without changing the helicity of the CTD or its orientation with respect to the membrane surface (see Figure 5.7). Instead, the peptide-membrane disassociation correlated with the decrease in membrane fluidity. The experimentally-observed decrease in membrane fluidity [91] was also implied indirectly as an increase in the calculated order parameter ($-S_{CD}$) of the membrane at 0.5 M KCl (see Figure 5.6B). A less fluid membrane might not accommodate the interactions with the anionic peptide. In this case, since ProP functions without the help of other proteins and does not respond to the changes in the membrane tension [78], it can be speculated that it might get activated with increasing salinity that causes a decrease in membrane fluidity. In other words, our results suggest that the membrane can act as an antenna that senses the osmotic upshifts, while the ProP acts as an osmoregulator.

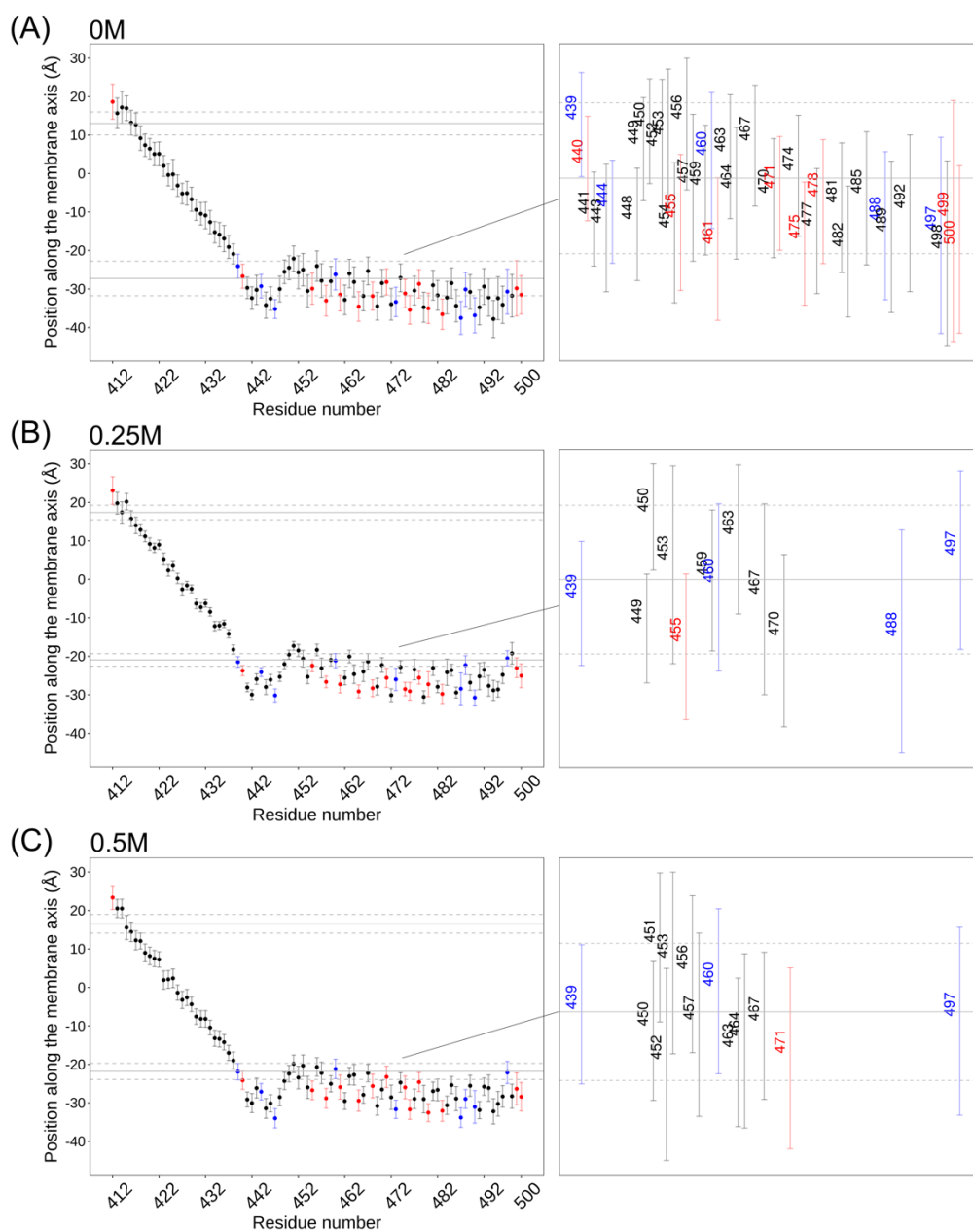


Figure 5.7. The position along the membrane axis of the lipid head groups and the ProP residues at (A) 0 M, (B) 0.25 M and (C) 0.5 M KCl. Here, the position of the geometric center of the non-hydrogen atoms in the lipid head groups were calculated only if any non-hydrogen lipid atom was closer than 5 Å to any non-hydrogen protein atom. The solid horizontal lines represent the average positions of the lipid head groups along the membrane axis calculated from the 100 ns-long molecular dynamics simulations, whereas the dashed horizontal lines show the standard deviation of the average position. The acidic and basic residues are colored in red and blue, respectively. The rest of the residues is colored in black. The square frame given next to each plot shows the residue number of any residue whose average position is within the one standard deviation on either side of the average position of the lipid head groups.

5.5. Conclusion

TMXII was attached to the CTD with the loop in a hairpin conformation in order to build a more realistic model of the ProP peptide (formed by residues 412-500) than the model of the peptide without TMXII. Our results showed that the attachment of TMXII significantly changes the frequency of interaction between the lipids and the membrane distal part of the ProP peptide, as well as the occurrence of salt bridges (within the peptide and between the peptide and the lipid). Probing the nature of interactions between the CTD helix and the membrane, we showed that increasing salt concentration changes the distance of the CTD helix from the membrane without altering intra-peptide contacts or hydrogen bonds. It also decreases the association between the peptide and lipids. The weakening of the peptide-lipid interaction is likely to arise from the decrease in the membrane fluidity. The membrane, as it becomes more ordered, might create local surface charge densities and therefore cause the peptide to move away from its surface. These results, as well as the long ProP peptide, can now be used to look at the association in more detail; molecular dynamics simulations can be combined with molecular biology tools for the investigation of different ProP CTD sequence variants and their capabilities for osmosensing and/or osmoregulating.

Chapter 6. Conclusion

This thesis focuses on the molecular modeling of the Orai calcium channel and ProP transporter. In the first part of this work, we built a homology model of the tetrameric assembly of the Orai protein based on the hexameric crystal structure from *D. melanogaster*. Since several studies in the literature identified a tetrameric assembly of Orai proteins as the active, calcium-selective Orai channel [42–44,50,52,53,132,133], we performed molecular dynamics simulations of hexameric and tetrameric Orai assemblies in order to investigate the structural dynamics. The conformational changes necessary for Orai gating by STIM are expected to be transmitted via contacts between the transmembrane domains of the channel [67,68,128]. Therefore, we compared these multimers in terms of contacts and pore dynamics as they are vital for channel function. The simulations showed that the tetramer model retains most of these structural features of the Orai hexamer, except for some differences. Notably, the number of side-chain contacts are higher in the hexamer, while stable salt bridges are more frequent in the tetramer. Finally, the most significant difference between these multimers is observed in their pores: compared to the hexamer, the tetramer channel displays tighter packing in the hydrophobic part of its pore, which contains almost no water molecules. Overall, our results suggest that the tetramer has potential to be a functional channel.

Recent studies hypothesized that the binding of STIM opens the Orai pore via a rotation of its pore-forming helices [67,68]. To test this idea, we built model structures of both assemblies with rotated pore-forming helices and performed molecular dynamics simulations. Although both structures can sustain the conformational changes due to the helix rotation and remain stable, their responses are different. When opened, the hexamer loses several contacts, whereas the tetramer gains contacts. Also, while helix rotation causes an increase in pore hydration for both multimers, the degree of this change is much higher in the tetrameric pore.

Next, we performed molecular dynamics simulations enhanced with umbrella sampling to examine ion permeation through the pores of Orai channels in their closed and open conformations. The closed Orai channels bind to Ca^{2+} at their selectivity filter better than they bind to Na^+ or K^+ , but create high energy barriers against ion permeation. When Orai multimers open, the permeation of a fully-hydrated Ca^{2+} ion becomes possible. The results clearly demonstrate that helix rotation significantly lowers the energy cost of translocating a hydrated

ion along the Orai pore. These observations are independent of the stoichiometry of the Orai channel. What depends on stoichiometry is the Ca^{2+} versus Na^+ selectivity. The effect of channel opening on Na^+ permeability is much more pronounced for the tetramer than for the hexamer. Conversely, the effect of helix rotation on Ca^{2+} permeation is more significant for the hexamer than the tetramer. Especially in the entrance of its hydrophobic part, the open tetrameric pore becomes too narrow to effectively mediate the permeation of a solvated Ca^{2+} ion. Therefore, the energy barrier posed by the tetramer is higher compared to that of the hexamer. It indicates that the hexameric Orai pore creates a more suitable environment for the permeation of a fully-hydrated Ca^{2+} ion. Along the rest of the pore, our results might not be accurate since they involve the permeation of a Ca^{2+} ion solvated by 6 and 7 water molecules, preventing the possibility of any favorable interaction between the permeant ion and Cl^- ions residing in the basic part of the pore. Nevertheless, our results do not show any weakness either in the structural integrity or pore dynamics of the tetramer, consistent with the tetramer being suggested as the functional Orai channel in several studies [42–50]. All these results underline that the tetramer could be functional, and therefore should be further studied experimentally.

We also demonstrated that the Orai pores form an unusual environment for permeant ions. The selectivity filter can directly coordinate permeant ions as long as it is not forming a salt bridge with K270 residues. Along the rest of the pore, the backbone oxygen atoms do not contribute to ion permeation. The pore is too wide for the direct coordination of the backbone atoms and considering the hydrophobic and basic parts of the pore, there are no candidates among the side chain atoms that could coordinate any permeant ion. This environment is very different when compared with other ion channels such as Na^+ and K^+ channels along which it is more common to find a permeant ion partially coordinated by the protein atoms [17]. Especially in most of canonical potassium channels –that are in general tetrameric– the TVGYG motif is responsible for coordinating K^+ ions preferentially over Na^+ ions [2,180]. As observed in Ca_v channels [2,181], Ca^{2+} selectivity seems to originate from an interplay between local negative charge density created by a ring of glutamate residues at the extracellular entrance of Orai pores and the concentration gradient of Ca^{2+} ions. Our results suggest that Orai channels provide a unique permeation pathway to Ca^{2+} ions along which they can permeate while being fully hydrated, in contrast to being directly coordinated by protein atoms as in other ion channels. Recently, the permeation of a nearly fully-hydrated Ca^{2+} ion was also observed through the ryanodine

receptors [182]. Combined together, these two studies form the first set of examples showing the permeation of fully-hydrated Ca^{2+} ions through channel proteins.

Calcium coordination with proteins is challenging to simulate using conventional protein force fields, since Ca^{2+} ions, due to their high charge density, polarize their environments more compared to monovalent ions such as Na^+ and K^+ [167]. The current Ca^{2+} force field does not accurately represent the binding affinity of the ion to one or more glutamate side chains [157,158,168,182]. Therefore, an improved Ca^{2+} force field can provide a better estimation of the ion selectivity of channel proteins. Fortunately, our simulations suggest that the details of coordination with protein side chains might not be important, since the pores of both Orai multimers sustain the permeation of a Ca^{2+} ion with its complete hydration shell. Otherwise, an improved Ca^{2+} force field would be absolutely necessary. Two other factors are worthwhile to consider: (1) the transmembrane potential, since divalent ions feel its effect more strongly, and (2) the presence of anions larger than Cl^- ions, since they are expected to be found within the basic region, stabilizing the closed conformation of the Orai pore [11].

Further understanding of Orai gating at atomistic detail requires the crystal structure of Orai channels in an open conformation and/or the crystal structure of the Orai-STIM assembly. A structure of the Orai-STIM assembly could provide more insight into how STIM binding alters the ion selectivity of the Orai channel. It might even resolve the debate on the multimeric state of the active Orai channel: if E178 and K270 residues in the tetramer form several salt bridges in the presence of STIM proteins (i.e. in an open state), then the channel would be less selective toward Ca^{2+} since these salt bridges would reduce the binding affinity to Ca^{2+} ions. Even though the free energy calculations presented in this thesis support the idea of the Orai hexamer being the calcium-selective Orai channel, it would be worthwhile to further investigate the possibility of the tetramer being functional, since our results indicate that, in the closed conformation, it retains most of the structural features of the hexamer and gains more contacts upon helix rotation. In the literature, the physiologically relevant oligomeric state of other ion channels was a matter of debate. For example, Hoogenboom et al. [183] showed a multitude of oligomeric states the voltage-dependent anion channels at a native-like environment by the use of AFM. The studies on the mechanosensitive channels of large conductance (MscL) led to different multimeric states: tetramer [184] and pentamer [185,186]. The debate on the multimeric state of the functional

MscL channel gained more interest after the resolution of two different crystal structures of MscL channel by X-ray crystallography and was resolved by Dorwart et al. who demonstrated that the detergent used in the X-ray study of the MscL tetramer can alter the stoichiometry of membrane proteins *in vitro* [186].

The last chapter in this thesis aimed to computationally investigate the role of the cytoplasmic C-terminal domain (CTD) of the ProP transporter in osmosensing. We studied interactions of the cytoplasmic CTD with the membrane in three parts. First, molecular dynamics simulations of the CTD helix were performed at different salt concentrations, showing that the CTD of the monomeric ProP either associates with the membrane surface or forms an antiparallel, homodimeric alpha-helical coiled-coil with an adjacent ProP. Second, we performed free energy calculations on the loop part of the CTD and showed that the loop is salt-sensitive. Finally, we built a homology model of the ProP peptide, including the transmembrane helix XII, the loop and the CTD and performed molecular dynamics simulations. The simulations showed that the CTD-membrane dissociation does not result from a salinity-dependent rearrangement of salt bridges. Instead, the weakening of the CTD-membrane interaction correlates with a decrease in membrane fluidity. This raises the possibility of ProP responding to the changes in membrane fluidity. With increasing osmolality, and therefore cytosolic K^+ concentration, a decrease in membrane fluidity is computationally and experimentally observed [91]. As the membrane becomes less fluid, the osmotically induced cation concentration may neutralize the membrane surface charge. These changes in the membrane might be responsible for the CTD-lipid dissociation. Other studies also showed the interaction between the membrane and a helical peptide to be coupled to the physical properties of the membrane. For instance, helix induction and membrane association of the intrinsically disordered protein α -synuclein were reported to be affected by membrane fluidity [187,188]. In the case of the α -helical antimicrobial peptides, an increase in membrane fluidity altered the membrane association of the peptides [189,190].

In this ongoing project, our next step would be to use molecular biology tools combined with molecular dynamics simulations to carefully investigate different ProP CTD sequence variants and their capabilities for osmosensing and/or osmoregulating. Therefore, our results, presented in Chapter 5, should be thought of as complementary to the vast experimental work being done in Dr. Wood's laboratory [77]. A detailed molecular modeling study of the complete ProP

transporter would require crystal structures of the transporter in its closed and open conformations. Fortunately, this requirement started to become more achievable especially due to the cryo-EM breakthrough in structural biology [191].

On a wider scope, this thesis demonstrates that molecular modeling is versatile to examine the relationship between the structures and functions of transport proteins in a high temporal and spatial resolution that is not achievable with experimental techniques. However, molecular modeling should be complemented by experiments, and often does require experimental input, including the structure of a protein as a starting point. This requirement becomes less and less problematic due to the cryo-EM revolution in structural biology. Cryo-electron microscopy (cryo-EM) has provided near-atomic resolution for a variety of proteins including several transport proteins. However, while these techniques generate data to be used in future computational studies, they can also spark more questions. For example, the recent cryo-EM structures of TRPV3 channels revealed differences in the closed and ligand-bound conformations of the channel [192,193]. Molecular dynamics simulations of ion channels can be used for investigating why these channels adopt different conformations in different environments (in lipid nanodiscs vs in detergent micelles) and validate the applicability of the experimental procedures on transport proteins.

Present challenges have yet to be addressed, particularly for molecular modeling of transport proteins. One of the most crucial fields in need of improvement is the development of force field parameters for the description of complex configurations involving divalent ions. Conventional protein force field parameters do not implement polarization and charge transfer effects that are vital for the modeling of divalent ions. Computational studies of ion selectivity and permeation in complex channels, such as the Orai calcium channel, can provide more precise details if the description of ions in different environments (water, protein, other biomolecules etc.) is better represented. This also applies to modeling the environment of transport proteins. Since transport proteins are a class of membrane proteins, they are affected by the treatment of surrounding lipids. The accuracy of simulations involving transport proteins can only be achieved if the simulated membranes are also treated correctly. The known issues with the geometrical and dynamical properties of membranes are associated with poor force field parameters [26]. Another important challenge is the high computational cost. All relevant states of a biomolecular

system must be sampled for a meaningful characterization of the system of interest. Fortunately, with advances in computational technology, larger biomolecular systems with longer time scales will be achieved, allowing us to study more complex phenomena. As long as simulation results are interpreted carefully by considering the shortcomings of the force field or the sampling technique, molecular modeling can provide atomistic level details into the fascinating world of transport proteins. As the technology advances, molecular modeling will continue to not only deepen scientific understanding of membrane proteins and cellular interactions as a whole but also develop potential therapeutics for channelopathies.

References

- [1] Hille, B. (2001). *Ion channels of excitable membranes*. Sunderland, MA: Sinauer Associates.
- [2] Zhekova, H. R., Ngo, V., da Silva, M. C., Salahub, D. & Noskov, S. (2017). Selective ion binding and transport by membrane proteins – A computational perspective. *Coord. Chem. Rev.* 345, 108–136.
- [3] Gadsby, D. C. (2009). Ion channels versus ion pumps: the principal difference, in principle. *Nat. Rev. Mol. Cell Biol.* 10(5), 344.
- [4] MacLennan, D. H. & Green, N. M. (2000). Structural biology: pumping ions. *Nature* 405(6787), 633–634.
- [5] Martin, R. B. (2006). Bioinorganic chemistry. In R. A. Meyers (Ed.) *Rev. Cell Biol. Mol. Med.* doi:10.1002/3527600906.mcb.200200012.
- [6] Gadsby, D. C. (2004). Ion transport: spot the difference. *Nature* 427(6977), 795–797.
- [7] Roux, B. (2017). Ion channels and ion selectivity. *Essays Biochem.* 61, 201–209.
- [8] Dubyak, G. R. (2004). Ion homeostasis, channels, and transporters: an update on cellular mechanisms. *Adv. Physiol. Educ.* 28, 143–154.
- [9] Milo, R. & Phillips, R. (2015). *Cell biology by the numbers*, Garland Science.
- [10] Etienne, A., Génard, M., Lobit, P., Mbéguié-A-Mbéguié, D. & Bugaud, C. (2013). What controls fleshy fruit acidity? A review of malate and citrate accumulation in fruit cells. *J. Exp. Bot.* 64, 1451–1469.
- [11] Hou, X., Pedi, L., Diver, M. M. & Long, S. B. (2012). Crystal structure of the calcium release-activated calcium channel Orai. *Science* 338(6112), 1308–1313.

- [12] Doyle, D. A., Cabral, J. M., Pfuetzner, R. A., Kuo, A., Gulbis, J. M., Cohen, S. L., Chait, B. T. & MacKinnon, R. (1998). The structure of the potassium channel: Molecular basis of K^+ conduction and selectivity. *Science* 280(5360), 69–77.
- [13] Kandt, C., Ash, W. L. & Tieleman, D. P. (2007). Setting up and running molecular dynamics simulations of membrane proteins. *Methods* 41(4), 475–488.
- [14] Corry, B. (2016). Computer simulation of ion channels. In *Computational biophysics of membrane proteins* (pp. 161–196). Cambridge: The Royal Society of Chemistry.
- [15] Roux, B. B., Allen, T., Bernèche, S. & Im, W. (2004). Theoretical and computational models of biological ion channels. *Q. Rev. Biophys.* 37(1), 15–103.
- [16] Roux, B. & Schulten, K. (2004). Computational studies of membrane channels. *Structure* 12(8), 1343–1351.
- [17] Lev, B., Noskov, S. Y., Yu, H., Rowley, C. N., Roux, B., Egwolf, B. & Bernèche, S. (2011). Ion selectivity in channels and transporters. *J. Gen. Physiol.* 137(5), 415–426.
- [18] Allen, T. W., Andersen, O. S. & Roux, B. (2004). Energetics of ion conduction through the gramicidin channel. *Proc. Natl. Acad. Sci.* 101(1), 117–122.
- [19] Bernèche, S. & Roux, B. (2005). A gate in the selectivity filter of potassium channels. *Structure* 13(4), 591–600.
- [20] Noskov, S. Y. & Roux, B. (2007). Importance of hydration and dynamics on the selectivity of the KcsA and NaK channels. *J. Gen. Physiol.* 129(2), 135–143.
- [21] Noskov, S. Y. & Roux, B. (2008). Control of ion selectivity in LeuT: two Na^+ binding sites with two different mechanisms. *J. Mol. Biol.* 377(3), 804–818.
- [22] Rui, H., Artigas, P. & Roux, B. (2016). The selectivity of the Na^+/K^+ -pump is controlled by binding site protonation and self-correcting occlusion. *Elife*, 5, e16616.

- [23] Feng, T., Kalyaanamoorthy, S., Ganesan, A. & Barakat, K. (2019). Atomistic modeling and molecular dynamics analysis of human Cav1.2 channel using external electric field and ion pulling simulations. *Biochim. Biophys. Acta.* 1863(6), 1116–1126.
- [24] Möller, I. R., Slivacka, M., Nielsen, A. K., Rasmussen, S. G. F., Gether, U., Loland, C. J. & Rand, K. D. (2019). Conformational dynamics of the human serotonin transporter during substrate and drug binding. *Nat. Commun.* 10(1), 1687.
- [25] Leone, V., Waclawska, I., Kossmann, K., Koshy, C., Sharma, M., Prisner, T. F., Ziegler, C., Endeward, B. & Forrest, L. R. (2019). Interpretation of spectroscopic data using molecular simulations for the secondary active transporter BetP. *J. Gen. Physiol.* 151(3), 381–394.
- [26] Khalili-Araghi, F., Gumbart, J., Wen, P.-C., Sotomayor, M., Tajkhorshid, E. & Schulten, K. (2009). Molecular dynamics simulations of membrane channels and transporters, *Curr. Opin. Struct. Biol.* 19(2), 128–137.
- [27] Hou, X. (2018). Ion channels. In *Advances in Membrane Proteins* (pp. 17–45), Singapore: Springer.
- [28] Prakriya, M. & Lewis, R. S. (2015). Store-operated calcium channels. *Physiol. Rev.* 95(4), 1383–1436.
- [29] Yeung, P. S. W. & Prakriya, M. (2018). The exquisitely cooperative nature of Orail channel activation. *J. Gen. Physiol.* 150(10), 1352–1355.
- [30] Zhang, S. L., Yu, Y., Roos, J., Kozak, J. A., Deerinck, T. J., Ellisman, M. H., Stauderman, K. A. & Cahalan, M. D. (2005). STIM1 is a Ca²⁺ sensor that activates Crac channels and migrates from the Ca²⁺ store to the plasma membrane. *Nature*, 437(7060), 902–905.
- [31] Liou, J., Kim, M. L., Do Heo, W., Jones, J. T., Myers, J. W., Ferrell Jr, J. E. & Meyer, T. (2005). STIM is a Ca²⁺ sensor essential for Ca²⁺-store-depletion-triggered Ca²⁺ influx. *Curr. Biol.* 15(13), 1235–1241.

- [32] Roos, J., DiGregorio, P. J., Yeromin, A. V., Ohlsen, K., Lioudyno, M., Zhang, S., Safrina, O., Kozak, J. A., Wagner, S. L., Cahalan, M. D. & others. (2005) STIM1, an essential and conserved component of store-operated Ca^{2+} channel function. *J. Cell Biol.* 169(3), 435–445.
- [33] Vig, M., Peinelt, C., Beck, A., Koomoa, D. L., Rabah, D., Koblan-Huberson, M., Kraft, S., Turner, H., Fleig, A., Penner, R. & others. (2006). CRACM1 is a plasma membrane protein essential for store-operated Ca^{2+} entry. *Science* 312(5777), 1220–1223.
- [34] Prakriya, M., Feske, S., Gwack, Y., Srikanth, S., Rao, A. & Hogan, P. G. (2006). Orai1 is an essential pore subunit of the Crac channel. *Nature*, 443(7108), 230–233.
- [35] Zhang, S. L., Yeromin, A. V., Zhang, X. H. F., Yu, Y., Safrina, O., Penna, A., Roos, J., Stauderman, K. A. & Cahalan, M. D. (2006). Genome-wide RNAi screen of Ca^{2+} influx identifies genes that regulate Ca^{2+} release-activated Ca^{2+} channel activity *Proc. Natl. Acad. Sci.* 103(24), 9357–9362.
- [36] Yen, M. & Lewis, R. S. (2018). Physiological CRAC channel activation and pore properties require STIM1 binding to all six Orai1 subunits. *J. Gen. Physiol.* 150(10), 1373–1385.
- [37] Stathopoulos, P. B., Schindl, R., Fahrner, M., Zheng, L., Gasmi-Seabrook, G. M., Muik, M., Romanin, C. & Ikura, M. (2013). Stim1/Orai1 coiled-coil interplay in the regulation of store-operated calcium entry. *Nat. Commun.* 4, 2963.
- [38] Li, Z., Liu, L., Deng, Y., Ji, W., Du, W., Xu, P., Chen, L. & Xu, T. (2011). Graded activation of Crac channel by binding of different numbers of Stim1 to Orai1 subunits. *Cell Res.* 21(2), 305–315.
- [39] Park, C. Y., Hoover, P. J., Mullins, F. M., Bachhawat, P., Covington, E. D., Raunser, S., Walz, T., Garcia, K. C., Dolmetsch, R. E. & Lewis, R. S. (2009). STIM1 clusters and activates Crac channels via direct binding of a cytosolic domain to Orai1. *Cell* 136(5), 876–890.

- [40] Zhou, Y., Meraner, P., Kwon, H. T., Machnes, D., Oh-Hora, M., Zimmer, J., Huang, Y., Stura, A., Rao, A. & Hogan, P. G. (2010). Stim1 gates the store-operated calcium channel Orai1 *in vitro*. *Nat. Struct. Mol. Biol.* 17(1), 112-116.
- [41] Derler, I., Plenk, P., Fahrner, M., Muik, M., Jardin, I., Schindl, R., Gruber, H. J., Groschner, K. & Romanin, C. (2013). The extended transmembrane Orai1 N-terminal (ETON) region combines binding interface and gate for Orai1 activation by Stim1. *J. Biol. Chem.* 288(40), 29025–29034.
- [42] Mignen, O., Thompson, J. L. & Shuttleworth, T. J. (2008). Orai1 subunit stoichiometry of the mammalian Crac channel pore. *J. Physiol.* 586(2), 419–425.
- [43] Penna, A., Demuro, A., Yeromin, A. V., Zhang, S. L., Safrina, O., Parker, I. & Cahalan, M. D. (2008). The Crac channel consists of a tetramer formed by Stim-induced dimerization of Orai dimers. *Nature* 456(7218), 116–120.
- [44] Maruyama, Y., Ogura, T., Mio, K., Kato, K., Kaneko, T., Kiyonaka, S., Mori, Y., & Sato, C. (2009). Tetrameric Orai1 is a teardrop-shaped molecule with a long, tapered cytoplasmic domain. *J. Biol. Chem.* 284(20), 13676–13685.
- [45] McNally, B. A., Yamashita, M., Engh, A. & Prakriya, M. (2009). Structural determinants of ion permeation in Crac channels. *Proc. Natl. Acad. Sci.* 106(52), 22516–22521.
- [46] Thompson, J. L., Mignen, O. & Shuttleworth, T. J. (2009). The Orai1 severe combined immune deficiency mutation and calcium release-activated Ca²⁺ channel function in the heterozygous condition. *J. Biol. Chem.* 284(11), 6620–6626.
- [47] Madl, J., Weghuber, J., Fritsch, R., Derler, I., Fahrner, M., Frischauf, I., Lackner, B., Romanin, C. & Schütz, G. J. (2010). Resting state Orai1 diffuses as homotetramer in the plasma membrane of live mammalian cells. *J. Biol. Chem.* 285(52), 41135–41142.
- [48] Zhang, S. L., Yeromin, A. V., Hu, J., Amcheslavsky, A., Zheng, H. & Cahalan, M. D. (2011). Mutations in Orai1 transmembrane segment 1 cause STIM1-independent activation of Orai1 channels at glycine 98 and channel closure at arginine 91. *Proc. Natl. Acad. Sci.* 108(43), 17939–17843.

- [49] McNally, B. A., Somasundaram, A., Yamashita, M. & Prakriya, M. (2012). Gated regulation of Crac channel ion selectivity by Stim1. *Nature* 482, 241–245.
- [50] Thompson, J. L. & Shuttleworth, T. J. (2013). How many Orai's does it take to make a CRAC channel?. *Sci. Rep.* 3, 1961.
- [51] Gwack, Y., Srikanth, S., Feske, S., Cruz-Guilloty, F., Oh-hora, M., Neems, D. S., Hogan, P. G. & Rao, A. (2007). Biochemical and functional characterization of orai proteins. *J. Biol. Chem.* 282(22), 16232–16243.
- [52] Ji, W., Xu, P., Li, Z., Lu, J., Liu, L., Zhan, Y., Chen, Y., Hille, B., Xu, T. & Chen, L. (2008). Functional stoichiometry of the unitary calcium-release-activated calcium channel. *Proc. Natl. Acad. Sci.* 105(36), 13668–13673.
- [53] Zhou, Y., Ramachandran, S., Oh-hora, M., Rao, A. & Hogan, P. G. (2010). Pore architecture of the Orai1 store-operated calcium channel. *Proc. Natl. Acad. Sci.* 107(11), 4896–4901.
- [54] Balasuriya, D., Srivats, S., Murrell-Lagnado, R. D. & Edwardson, J. M. (2014). Atomic force microscopy (AFM) imaging suggests that stromal interaction molecule 1 (Stim1) binds to Orai1 with sixfold symmetry. *FEBS Lett.* 588(17), 2874–2880.
- [55] Cai, X., Zhou, Y., Nwokonko, R. M., Loktionova, N. A., Wang, X., Xin, P., Trebak, M., Wang, Y. & Gill, D. L. (2016). The Orai1 store-operated calcium channel functions as a hexamer. *J. Biol. Chem.* 291(50), 25764–25775.
- [56] Yen, M., Lokteva, L. A. & Lewis, R. S. (2016). Functional analysis of Orai1 concatemers supports a hexameric stoichiometry for the Crac channel. *Biophys. J.* 111(9), 1897–1907.
- [57] Hou, X., Burstein, S. R. & Long, S. B. (2018). Structures reveal opening of the store-operated calcium channel Orai. *Elife*, 7, e36758.
- [58] Dong, H., Fiorin, G., Carnevale, V., Treptow, W. & Klein, M. L. (2013). Pore waters regulate ion permeation in a calcium release-activated calcium channel. *Proc. Natl. Acad. Sci.* 110(43), 17332–17337.

- [59] Alansary, D., Schmidt, B., Dörr, K., Bogeski, I., Rieger, H., Kless, A. & Niemeyer, B. A. (2016). Thiol dependent intramolecular locking of Orai1 channels. *Sci. Rep.* 6, 33347.
- [60] Sampath, B. & Sankaranarayanan, K. (2016). Glu106 targeted inhibitors of Orai1 as potential Ca^{2+} release-activated Ca^{2+} (Crac) channel blockers—molecular modeling and docking studies. *J. Recept. Signal Transduct.* 36(6), 572–585.
- [61] Maganti, L., Ghosh, M. & Chakrabarti, J. (2018). Molecular dynamics studies on conformational thermodynamics of Orai1–calmodulin complex. *J. Biomol. Struct. Dyn.* 36(13), 3411–3419.
- [62] Maganti, L., Dutta, S., Ghosh, M. & Chakrabarti, J. (2019). Allostery in Orai1 binding to calmodulin revealed from conformational thermodynamics. *J. Biomol. Struct. Dyn.* 37(2), 493–502.
- [63] Frischauf, I., Zayats, V., Deix, M., Hochreiter, A., Jardin, I., Muik, M., Lackner, B., Svobodová, B., Pammer, T., Litviňuková, M., Sridhar, A. A., Derler, I., Bogeski, I., Romanin, C., Ettrich, R. H. & Schindl, R. (2015). A calcium-accumulating region, CAR, in the channel Orai1 enhances Ca^{2+} permeation and SOCE-induced gene transcription. *Sci. Signal.* 8(408), ra131.
- [64] Frischauf, I., Litvivňuková, M., Schober, R., Zayats, V., Svobodová, B., Bonhenry, D., Lunz, V., Cappello, S., Tociu, L., Reha, D., Stallinger, A., Hochreiter, A., Pammer, T., Butorac, C., Muik, M., Groschner, K., Bogeski, I., Ettrich, R. H., Romanin, C. & Schindl, R. (2017). Transmembrane helix connectivity in Orai1 controls two gates for calcium-dependent transcription. *Sci. Signal.* 10(157), eaao0358.
- [65] Fahrner, M., Pandey, S. K., Muik, M., Traxler, L., Butorac, C., Stadlbauer, M., Zayats, V., Krizova, A., Plenk, P., Frischauf, I. ... & Derler, I. (2018). Communication between N terminus and loop2 tunes Orai activation. *J. Biol. Chem.* 293(4), 1271–1285.
- [66] Derler, I., Butorac, C., Krizova, A., Stadlbauer, M., Muik, M., Fahrner, M., Frischauf, I. & Romanin, C. (2018). Authentic Crac channel activity requires Stim1 and the conserved portion of the Orai N terminus. *J. Biol. Chem.* 293(4), 1259–1270.

- [67] Yamashita, M., Yeung, P. S. W., Ing, C. E., McNally, B. A., Pomès, R. & Prakriya, M. (2017). Stim1 activates Crac channels through rotation of the pore helix to open a hydrophobic gate. *Nat. Commun.* 8, 14512.
- [68] Yeung, P. S. W., Yamashita, M., Ing, C. E., Pomès, R., Freymann, D. M. & Prakriya, M. (2018). Mapping the functional anatomy of Orail transmembrane domains for Crac channel gating. *Proc. Natl. Acad. Sci.* 115(22), E5193–E5202.
- [69] Nesin, V., Wiley, G., Kousi, M., Ong, E. C., Lehmann, T., Nicholl, D. J., Suri, M., Shahrizaila, N., Katsanis, N., Gaffney, P. M., Wierenga, K. J. & Tsiokas, L. (2014). Activating mutations in Stim1 and Orail cause overlapping syndromes of tubular myopathy and congenital miosis. *Proc. Natl. Acad. Sci.* 111(11), 4197–4202.
- [70] Böhm, J., Bulla, M., Urquhart, J. E., Malfatti, E., Williams, S. G., O’Sullivan, J., Szlauer, A., Koch, C., Baranello, G., Mora, M., Ripolone, M., Violano, R., Moggio, M., Kingston, H., Dawson, T., DeGoede, C. G., Nixon, J., Boland, A., Deleuze, J. F., Romero, N., Newman, W. G., Demareux, N. & Laporte, J. (2017). Orail mutations with distinct channel gating defects in tubular aggregate myopathy. *Hum. Mutat.* 38(4), 426–438.
- [71] Chou, J., Badran, Y. R., Yee, C. S. K., Bainter, W., Ohsumi, T. K., Al-Hammadi, S., Pai, S. Y., Feske, S. & Geha, R. S. (2015). A novel mutation in Orail presenting with combined immunodeficiency and residual T-cell function. *J. Allergy Clin. Immunol.* 136(2), 479–482.
- [72] Feske, S., Gwack, Y., Prakriya, M., Srikanth, S., Puppel, S. H., Tanasa, B., Hogan, P. G., Lewis, R. S., Daly, M. & Rao, A. (2006). A mutation in Orail causes immune deficiency by abrogating Crac channel function. *Nature* 441, 179–185.
- [73] Feske, S., Picard, C. & Fischer, A. (2010). Immunodeficiency due to mutations in ORAI1 and STIM1. *Clin. Immunol.* 135(2), 169–182.
- [74] Lian, J., Cuk, M., Kahlfuss, S., Kozhaya, L., Vaeth, M., Rieux-Laucat, F., Picard, C., Benson, M. J., Jakovcevic, A., Bilic, K., Martinac, I., Stathopoulos, P., Kacs Kovics, I., Vraetz, T., Speckmann, C., Ehl, S., Issekutz, T., Unutmaz, D. & Feske, S. (2018). Orail

- mutations abolishing store-operated Ca^{2+} entry cause anhidrotic ectodermal dysplasia with immunodeficiency. *J. Allergy Clin. Immunol.* 142(4), 1297-1310.
- [75] McCarl, C. A., Picard, C., Khalil, S., Kawasaki, T., Röther, J., Papolos, A., Kutok, J., Hivroz, C., LeDeist, F., Plogmann, K., Ehl, S., Notheis, G., Albert, M. H., Belohradsky, B. H., Kirschner, J., Rao, A., Fischer, A. & Feske S. (2009). Orai1 deficiency and lack of store-operated Ca^{2+} entry cause immunodeficiency, myopathy, and ectodermal dysplasia. *J. Allergy Clin. Immunol.* 124, 1311-1318.
- [76] Lacruz, R. S. & Feske, S. (2015) Diseases caused by mutations in Orai1 and Stim1. *Ann. N. Y. Acad. Sci.* 1356(1), 45–79.
- [77] Wood, J. M. (2010). Bacterial Osmoregulation: A Paradigm for the Study of Cellular Homeostasis. *Annu. Rev. Microbiol.* 65, 215–238.
- [78] Poolman, B., Spitzer, J. J. & Wood, J. M. (2004). Bacterial osmosensing: roles of membrane structure and electrostatics in lipid–protein and protein–protein interactions. *Biochim. Biophys. Acta (BBA)-Biomembranes* 1666(1-2), 88–104.
- [79] Wood, J. M. (2007). Bacterial osmosensing transporters. In *Methods in enzymology* (Vol. 428, pp.77–107). Academic Press.
- [80] Wood, J. M. (2015). Bacterial responses to osmotic challenges. *J. Gen. Physiol.* 145(5), 381–388.
- [81] Racher, K. I., Voegelé, R. T., Marshall, E. V., Culham, D. E., Wood, J. M., Jung, H., Bacon, M., Cairns, M. T., Ferguson, S. M., Liang, W. J. ... & Hallet, F. R. (1999). Purification and reconstitution of an osmosensor: transporter ProP of *Escherichia coli* senses and responds to osmotic shifts. *Biochemistry* 38(6), 1676–1684.
- [82] Wood, J. M. (1999). Osmosensing by bacteria: signals and membrane-based sensors. *Microbiol. Mol. Biol. Rev.* 63(1), 230–262.

- [83] Culham, D. E., Tripet, B., Racher, K. I., Voegelé, R. T., Hodges, R. S. & Wood, J. M. (2000). The role of the carboxyl terminal α -helical coiled-coil domain in osmosensing by transporter ProP of *Escherichia coli*. *J. Mol. Recognit.* 13(5), 309–322.
- [84] Wood, J. M., Culham, D. E., Hillar, A., Vernikovska, Y. I., Liu, F., Boggs, J. M. & Keates, R. A. B. (2005). A structural model for the osmosensor, transporter, and osmoregulator ProP of *Escherichia coli*. *Biochemistry* 44(15), 5634–5646.
- [85] Zoetewey, D. L., Tripet, B. P., Kutateladze, T. G., Overduin, M. J., Wood, J. M. & Hodges, R. S. (2003). Solution structure of the C-terminal antiparallel coiled-coil domain from *Escherichia coli* osmosensor ProP. *J. Mol. Biol.* 334(5), 1063–1076.
- [86] Hillar, A., Culham, D. E., Vernikovska, Y. I., Wood, J. M. & Boggs, J. M. (2005). Formation of an antiparallel, intermolecular coiled coil is associated with *in vivo* dimerization of osmosensor and osmoprotectant transporter ProP in *Escherichia coli*. *Biochemistry* 44(30), 10170–10180.
- [87] Culham, D. E., Henderson, J., Crane, R. A. & Wood, J. M. (2003). Osmosensor ProP of *Escherichia coli* responds to the concentration, chemistry, and molecular size of osmolytes in the proteoliposome lumen. *Biochemistry* 42(2), 410–420.
- [88] Culham, D. E., Shkel, I. A., Record, M. T. & Wood, J. M. (2016). Contributions of Coulombic and Hofmeister effects to the osmotic activation of *Escherichia coli* transporter ProP. *Biochemistry* 55(9), 1301–1313.
- [89] Romantsov, T., Stalker, L., Culham, D. E. & Wood, J. M. (2008). Cardiolipin controls the osmotic stress response and the subcellular location of transporter ProP in *Escherichia coli*. *J. Biol. Chem.* 283(18), 12314–12323.
- [90] Romantsov, T., Culham, D. E., Caplan, T., Garner, J., Hodges, R. S. & Wood, J. M. (2017). ProP-ProP and ProP-phospholipid interactions determine the subcellular distribution of osmosensing transporter ProP in *Escherichia coli*, *Mol. Microbiol.* 103(3), 469–482.

- [91] Culham, D. E., Marom, D., Boutin, R., Garner, J., Ozturk, T. N., Sahtout, N., Tempelhagen, L., Lamoureux, G. & Wood, J. M. (2018). Dual role of the C-terminal domain in osmosensing by bacterial osmolyte transporter ProP. *Biophys. J.* 115(11), 2152–2166.
- [92] Carpenter, E. P., Beis, K., Cameron, A. D. & Iwata, S. (2008). Overcoming the challenges of membrane protein crystallography. *Curr. Opin. Struct. Biol.* 18(5), 581–586.
- [93] Krieger, E., Nabuurs, S. B. & Vriend, G. (2003). Homology modeling. In *Structural bioinformatics* (vol 44, pp. 507–521).
- [94] Lesk, A. M. & Chothia, C. (1980). How different amino acid sequences determine similar protein structures: The structure and evolutionary dynamics of the globins. *J. Mol. Biol.* 136(3), 225–270.
- [95] Chothia, C. & Lesk, A. M. (1986). The relation between the divergence of sequence and structure in proteins. *EMBO J.* 5(4), 823–826.
- [96] Illergård, K., Ardell, D. H. & Elofsson, A. (2009) Structure is three to ten times more conserved than sequence – A study of structural response in protein cores. *Proteins Struct. Funct. Bioinforma.* 77(3), 499–508.
- [97] Šali, A. & Blundell, T. L. (1993). Comparative protein modelling by satisfaction of spatial restraints. *J. Mol. Biol.* 234(3), 779–815.
- [98] Fiser, A. & Šali, A. (2003). Modeller: generation and refinement of homology-based protein structure models. In *Methods in enzymology* (vol 374, pp. 461–91).
- [99] Eswar, N., Eramian, D., Webb, B., Shen, M. & Šali, A. (2008). Protein structure modeling with Modeller. In *Structural proteomics – Methods in molecular biology* (vol 426, pp.145–159).

- [100] Geer, L. Y., Marchler-Bauer, A., Geer, R. C., Han, L., He, J., He, S., Liu, C., Shi, W. & Bryant, S. H. (2009). The NCBI biosystems database, *Nucleic Acids Res.* 38, D492–D496.
- [101] Berman, H. M., Westbrook, J., Feng, Z., Gilliland, G., Bhat, T. N., Weissig, H., Shindyalov, I. N. & Bourne, P. E. (2000). The protein data bank, *Nucleic Acids Res.* 28(1), 235–242.
- [102] Tramontano, A. (1998). Homology modeling with low sequence identity. *Methods* 14(3), 293–300.
- [103] Eswar, N., Webb, B., Marti-Renom, M. A., Madhusudhan, M. S., Eramian, D., Shen, M., Pieper, U. & Šali, A. (2006). Comparative protein structure modeling using Modeller. *Curr. Protoc. Bioinforma.* 15(1), 5.6.1–5.6.30.
- [104] Braun, E., Gilmer, J., Mayes, H. B., Mobley, D. L., Jacob, I., Prasad, S. & Zuckerman, D. M. (2018). Best practices for foundations in molecular simulations [Article v1.0]. *Living Journal of Computational Molecular Science*, 1(1), 5957.
- [105] Leach, A. R. (2001). *Molecular modelling: principles and applications*. Pearson education.
- [106] Frenkel, D. & Smit, B. (2001). *Understanding molecular simulation: from algorithms to applications* (vol 1). Elsevier.
- [107] Adcock, S. A. & McCammon, J. A. (2006) Molecular dynamics: survey of methods for simulating the activity of proteins. *Chem. Rev.* 106(5). 1589–1615.
- [108] Martyna, G. J., Tobias, D. J. & Klein, M. L. (1994). Constant pressure molecular dynamics algorithms. *J. Chem. Phys.* 101(5), 4177–4189.
- [109] Feller, S. E., Zhang, Y., Pastor, R. W. & Brooks, B. R. (1995). Constant pressure molecular dynamics simulation: the Langevin piston method. *J. Chem. Phys.* 103(11), 4613–4621.

- [110] Huang, J. & MacKerell Jr, A. D. (2013). CHARMM36 all-atom additive protein force field: Validation based on comparison to NMR data. *J. Comput. Chem.* 34(25), 2135–2145.
- [111] Guvench, O., Mallajosyula, S. S., Raman, E. P., Hatcher, E., Vanommeslaeghe, K., Foster, T. J., Jamison, F. W. & MacKerell Jr, A. D. (2011). CHARMM additive all-atom force field for carbohydrate derivatives and its utility in polysaccharide and carbohydrate-protein modeling. *J. Chem. Theory Comput.* 7(10), 3162–3180.
- [112] Georgoulia, P. S. & Glykos, N. M. (2019). Molecular simulation of peptides coming of age: Accurate prediction of folding, dynamics and structures. *Arch. Biochem. Biophys.* 664, 76–88.
- [113] Ferraro, M. & Colombo, G. (2018). Targeting difficult protein-protein interactions with plain and general computational approaches. *Molecules* 23(9), 2256.
- [114] Durrant, J. D. & McCammon, J. A. (2011). Molecular dynamics simulations and drug discovery. *BMC Biol.* 9(1), 71.
- [115] Lei, H. & Duan, Y. (2007). Improved sampling methods for molecular simulation. *Curr. Opin. Struct. Biol.* 17(2), 187–191.
- [116] Kästner, J. (2011). Umbrella sampling. *Wiley Interdiscip. Rev. Comput. Mol. Sci.* 1(6), 932–942.
- [117] Souaille, M. & Roux, B. (2001). Extension to the weighted histogram analysis method: combining umbrella sampling with free energy calculations. *Comput. Phys. Commun.* 135(1), 40–57.
- [118] Hansen, N. & van Gunsteren, W. F. (2014). Practical aspects of free-energy calculations: A review. *J. Chem. Theory Comput.* 10(7), 2632–2647.
- [119] Christ, C. D., Mark, A. E. & van Gunsteren, W. F. (2010). Basic ingredients of free energy calculations: A review. *J. Comput. Chem.* 31(8), 1569–1582.

- [120] van Gunsteren, W. F., Daura, X. & Mark, A. E. (2002). Computation of free energy. *Helv. Chim. Acta* 85(10), 3113–3129.
- [121] Hill, T. L. (1986). An introduction to statistical thermodynamics. Courier Corporation.
- [122] Blossey, R. (2006). Computational biology: A statistical mechanics perspective. Chapman and Hall/CRC Press.
- [123] Zuckerman, D. M. (2010). Statistical physics of biomolecules: An introduction. CRC Press.
- [124] Beveridge, D. L. & DiCapua, F. M. (1989). Free energy via molecular simulation: applications to chemical and biomolecular systems. *Annu. Rev. Biophys. Biophys. Chem.* 18, 431–492.
- [125] Hénin, J., Fiorin, G., Chipot, C. & Klein, M. L. (2010). Exploring multidimensional free energy landscapes using time-dependent biases on collective variables. *J. Chem. Theory Comput.* 6, 35–47.
- [126] Hénin, J., Gumbart, J., & Chipot, C. (2017). Free energy calculations along a reaction coordinate: A tutorial for adaptive biasing force simulations [PDF file]. Retrieved from <https://www.ks.uiuc.edu/Training/Tutorials/namd/ABF/tutorial-abf.pdf>.
- [127] Darve, E., Rodríguez-Gómez, D. & Pohorille, A. (2008). Adaptive biasing force method for scalar and vector free energy calculations, *J. Chem. Phys.* 128(14), 144120.
- [128] Yeung, P. S. W., Yamashita, M. & Prakriya, M. (2017). Pore opening mechanism of Crac channels. *Cell Calcium* 63, 14–19.
- [129] Prakriya, M. (2013). Store-operated Orai channels: Structure and function. In *Current topics in membranes* (Vol 71, pp. 1–32).
- [130] Feske, S. (2010). Crac channelopathies. *Pflugers Arch. Eur. J. Physiol.* 460(2), 417–435.

- [131] Amcheslavsky, A., Wood, M. L., Yeromin, A. V., Parker, I., Freites, J. A., Tobias, D. J. & Cahalan, M. D. (2015). Molecular biophysics of Orai store-operated Ca^{2+} channels. *Biophys. J.* 108(2), 237–246.
- [132] Demuro, A., Penna, A., Safrina, O., Yeromin, A. V., Amcheslavsky, A., Cahalan, M. D. & Parker, I. (2011). Subunit stoichiometry of human Orai1 and Orai3 channels in closed and open states. *Proc. Natl. Acad. Sci.* 108(43), 17832-17837.
- [133] Inayama, M., Suzuki, Y., Yamada, S., Kurita, T., Yamamura, H., Ohya, S., Giles, W. R. & Imaizumi, Y. (2015). Orai1-Orai2 complex is involved in store-operated calcium entry in chondrocyte cell lines. *Cell Calcium* 57(5-6), 337–47.
- [134] Bulla, M., Gyimesi, G., Kim, J. H., Bhardwaj, R., Hediger, M. A., Frieden, M. & Demaurex, N. (2019). Orai1 channel gating and selectivity is differentially altered by natural mutations in the first or third transmembrane domain. *J. Physiol.* 597(2), 561–582.
- [135] Zhou, Y., Cai, X., Loktionova, N. A., Wang, X., Nwokonko, R. M., Wang, X., Wang, Y., Rothberg, B. S., Trebak, M. & Gill, D. L. (2016). The Stim1-binding site nexus remotely controls Orai1 channel gating. *Nat. Commun.* 7, 13725.
- [136] Yeromin, A. V., Zhang, S. L., Jiang, W., Yu, Y., Safrina, O. & Cahalan, M. D. (2006). Molecular identification of the Crac channel by altered ion selectivity in a mutant of Orai. *Nature* 443, 226–229.
- [137] Gudlur, A., Quintana, A., Zhou, Y., Hirve, N., Mahapatra, S. & Hogan, P. G. (2014). Stim1 triggers a gating rearrangement at the extracellular mouth of the Orai1 channel. *Nat. Commun.* 5, 5164.
- [138] Lomize, M. A., Pogozheva, I. D., Joo, H., Mosberg, H. I. & Lomize, A. L. (2011). OPM database and PPM web server: resources for positioning of proteins in membranes. *Nucleic Acids Res.* 40, D370–D376.
- [139] Jo, S., Kim, T., Iyer, V. G. & Im, W. (2008). Charmm-Gui: A web-based graphical user interface for Charmm. *J. Comput. Chem.* 29(11), 1859–1865.

- [140] Jo, S., Kim, T. & Im, W. (2007). Automated builder and database of protein/membrane complexes for molecular dynamics simulations. *PLoS One* 2(9), e880.
- [141] Price, D. J. & Brooks, C. L. (2004). A modified TIP3P water potential for simulation with Ewald summation. *J. Chem. Phys.* 121, 10096–10103.
- [142] Andersen, H. C. (1983). Rattle: A “velocity” version of the shake algorithm for molecular dynamics calculations. *J. Comput. Phys.* 52, 24–34.
- [143] Essmann, U., Perera, L., Berkowitz, M. L., Darden, T., Lee, H. & Pedersen, L. G. (1995). A smooth particle mesh Ewald method. *J. Chem. Phys.* 103, 8577–8593.
- [144] MacKerell, A. D., Bashford, D., Bellott, M., Dunbrack, R. L., Evanseck, J. D., Field, M. J., Fischer, S., Gao, J., Guo, H., Ha, S., Joseph-McCarthy, D., Kuchnir, L., Kuczera, K., Lau, F. T. K., Mattos, C., Michnick, S., Ngo, T., Nguyen, D. T., Prodhom, B., Reiher, W. E., Roux, B., Schlenkrich, M., Smith, J. C., Stote, R., Straub, J., Watanabe, M., Wiórkiewicz-Kuczera, J., Yin, D. & Karplus, M. (1998). All-Atom Empirical Potential for Molecular Modeling and Dynamics Studies of Proteins. *J. Phys. Chem. B* 102(18), 3586–3616.
- [145] Phillips, J. C., Braun, R., Wang, W., Gumbart, J., Tajkhorshid, E., Villa, E., Chipot, C., Skeel, R. D., Kalé, L. & Schulten, K. (2005). Scalable molecular dynamics with NAMD. *J. Comput. Chem.* 26(16), 1781–1802.
- [146] Smart, O. S., Neduelil, J. G., Wang, X., Wallace, B. A. & Sansom, M. S. P. (1996). HOLE: a program for the analysis of the pore dimensions of ion channel structural models. *J. Mol. Graph.* 14(6), 354–360.
- [147] Grant, B. J., Rodrigues, A. P. C., ElSawy, K. M., McCammon, J. A. & Caves, L. S. D. (2006). Bio3d: An R package for the comparative analysis of protein structures. *Bioinformatics* 22(21), 2695–2696.
- [148] Michaud-Agrawal, N., Denning, E. J., Woolf, T. B. & Beckstein, O. (2011). MDAnalysis: A toolkit for the analysis of molecular dynamics simulations. *J. Comput. Chem.* 32(10), 2319–2327.

- [149] Gowers, R., Linke, M., Barnoud, J., Reddy, T., Melo, M., Seyler, S., Domański, J., Dotson, D., Buchoux, S., Kenney, I. & Beckstein, O. (2016). MDAnalysis: A Python Package for the Rapid Analysis of Molecular Dynamics Simulations. In *Proc. of the 15th Python in Science Conf.* (Vol. 98, pp 98–105). Austin, TX: SciPy.
- [150] Humphrey, W., Dalke, A. & Schulten, K. (1996). VMD: Visual molecular dynamics. *J. Mol. Graph.* 14(1), 33–38.
- [151] Wickham, H. (2016). *ggplot2: Elegant graphics for data analysis*. Springer International Publishing.
- [152] Liu, X., Wu, G., Yu, Y., Chen, X., Ji, R., Lu, J., Li, X., Zhang, X., Yang, X. & Shen, Y. (2019). Molecular understanding of calcium permeation through the open Orai channel. *PLoS Biol.* 17(4), e3000096.
- [153] Hoth, M. & Penner, R. (1993). Calcium release-activated calcium current in rat mast cells. *J. Physiol.* 465(1), 359–386.
- [154] Zweifach, A. & Lewis, R. S. (1993). Mitogen-regulated Ca^{2+} current of T lymphocytes is activated by depletion of intracellular Ca^{2+} stores. *Proc. Natl. Acad. Sci.* 90(13), 6295–6299.
- [155] Prakriya, M. & Lewis, R. S. (2006). Regulation of Crac channel activity by recruitment of silent channels to a high open-probability gating mode. *J. Gen. Physiol.* 128(3), 373–386.
- [156] Mignen, O., Thompson, J. L. & Shuttleworth, T. J. (2008). Both Orai1 and Orai3 are essential components of the arachidonate-regulated Ca^{2+} -selective (ARC) channels. *J. Physiol.* 586(1), 185–195.
- [157] Flood, E. (2017). Molecular simulations of ion permeation and selectivity in sodium selective ion channels. (Doctoral dissertation). Retrieved from RMIT University Research Repository. (Accession No. 162374)

- [158] Åqvist, J. (1990). Ion-water interaction potentials derived from free energy perturbation simulations. *J. Phys. Chem.* *94*(21), 8021–8024.
- [159] Fiorin, G., Klein, M. L. & Hémin, J. (2013). Using collective variables to drive molecular dynamics simulations. *Mol. Phys.* *111*(22-23), 3345–3362.
- [160] Grossfield, A. WHAM: the weighted histogram analysis method, Version 2.0.9.
- [161] Rowley, C. N. & Roux, B. (2012). The solvation structure of Na⁺ and K⁺ in liquid water determined from high level ab initio molecular dynamics simulations. *J. Chem. Theory Comput.* *8*(10), 3526–3535.
- [162] Bako, I., Hutter, J. & Palinkas, G. (2002). Car–Parrinello molecular dynamics simulation of the hydrated calcium ion. *J. Chem. Phys.* *117*(21), 9838–9843.
- [163] Lightstone, F. C., Schwegler, E., Allesch, M., Gygi, F. & Galli, G. (2005). A First-Principles Molecular Dynamics Study of Calcium in Water. *Chem. Phys. Chem.* *6*(9), 1745–1749.
- [164] Salanne, M., Tazi, S., Vuilleumier, R. & Rotenberg, B. (2017). Ca²⁺–Cl[−] Association in Water Revisited: The Role of Cation Hydration. *Chem. Phys. Chem.* *18*(19), 2807–2811.
- [165] Bucher, D. & Kuyucak, S. (2008). Polarization of water in the first hydration shell of K⁺ and Ca²⁺ ions. *J. Phys. Chem. B* *112*(35), 10786–10790.
- [166] Corry, B. (2013). Na⁺/Ca²⁺ selectivity in the bacterial voltage-gated sodium channel NavAb. *PeerJ* *1*, e16.
- [167] Yoo, J., Wilson, J. & Aksimentiev, A. (2016). Improved model of hydrated calcium ion for molecular dynamics simulations using classical biomolecular force fields. *Biopolymers* *105*(10), 752-763.
- [168] Martinek, T., Duboué-Dijon, E., Timr, Š., Mason, P. E., Baxová, K., Fischer, H. E., Schmidt, B., Pluhařová, E. & Jungwirth, P. (2018). Calcium ions in aqueous solutions:

- Accurate force field description aided by ab initio molecular dynamics and neutron scattering. *J. Chem. Phys.* 148(22), 222813.
- [169] Hess, P. & Tsien, R. W. (1984). Mechanism of ion permeation through calcium channels. *Nature* 309, 453–6.
- [170] Catterall, W. A. (2000). Structure and regulation of voltage-gated Ca²⁺ channels. *Annu. Rev. Cell Dev. Biol.* 16, 521–555.
- [171] Tyson, J. R. & Snutch, T. P. (2013). Molecular nature of voltage-gated calcium channels: Structure and species comparison. *Wiley Interdiscip. Rev. Membr. Transp. Signal.* 2(5), 181–206.
- [172] Ren, F., Logeman, B. L., Zhang, X., Liu, Y., Thiele, D. J. & Yuan, P. (2019). X-ray structures of the high-affinity copper transporter Ctr1. *Nat. Commun.* 10, 1386.
- [173] Wood, J. M., Bremer, E., Csonka, L. N., Kraemer, R., Poolman, B., van der Heide, T., & Smith, L. T. (2001). Osmosensing and osmoregulatory compatible solute accumulation by bacteria. *Comp. Biochem. Physiol. Part A Mol. Integr. Physiol.* 130(3), 437–460.
- [174] Larking, M. A., Blackshields, G., Brown, N. P., Chenna, R., McGettigan, G. A., McWilliam, H., ... & Thompson, J. D. (2007). Clustal W and Clustal X version 2.0. *Bioinformatics* 23(21), 2947–2948.
- [175] Tsatskis, Y., Kwok, S. C., Becker, E., Gill, C., Smith, M. N., Keates, R. A., ... & Wood, J. M. (2008). Core Residue Replacements Cause Coiled-Coil Orientation Switching *in vitro* and *in vivo*: Structure–Function Correlations for Osmosensory Transporter ProP. *Biochemistry* 47(1), 60–72.
- [176] Liu, F., Culham, D. E., Vernikovska, Y. I., Keates, R. A. B., Boggs, J. M. & Wood, J. M. (2007). Structure and function of transmembrane segment XII in osmosensor and osmoprotectant transporter ProP of *Escherichia coli*. *Biochemistry* 46(19), 5647–5655.

- [177] Kelley, L. A., Mezulis, S., Yates, C. M., Wass, M. N. & Sternberg, M. J. E. (2015). The Phyre2 web portal for protein modeling, prediction and analysis. *Nat. Protoc.* 10(6), 845–858.
- [178] Sun, L., Zeng, X., Yan, C., Sun, X., Gong, X., Rao, Y. & Yan, N. (2012). Crystal structure of a bacterial homologue of glucose transporters GLUT1–4. *Nature* 490, 361–366.
- [179] Guixà-González, R., Rodríguez-Espigares, I., Ramírez-Anguita, J. M., Carrió-Gaspar, P., Martínez-Seara, H., Giorgino, T. & Selent, J. (2014). MEMBPLUGIN: Studying membrane complexity in VMD. *Bioinformatics* 30(10), 1478–1480.
- [180] Furini, S. & Domene, C. (2013). K⁺ and Na⁺ Conduction in Selective and Nonselective Ion Channels Via Molecular Dynamics Simulations. *Biophys. J.* 105(8), 1737–1745.
- [181] Sather, W. A. & McCleskey, E. W. (2003). Permeation and selectivity in calcium channels. *Annu. Rev. Physiol.* 65(1), 133–159.
- [182] Zhang, A., Yu, H., Liu, C. & Song, C. (2019). The Ca²⁺ permeation mechanism of the ryanodine receptor revealed by a multi-site ion model. *bioRxiv*, 682328.
- [183] Hoogenboom, B. W., Suda, K., Engel, A. & Fotiadis, D. (2007). The supramolecular assemblies of voltage-dependent anion channels in the native membrane. *J. Mol. Biol.* 370(2), 246–255.
- [184] Liu, Z., Gandhi, C. S. & Rees, D. C. (2009). Structure of a tetrameric MscL in an expanded intermediate state. *Nature* 461, 120–124.
- [185] Perozo, E., Cortes, D. M., Sompornpisut, P., Kloda, A. & Martinac, B. (2002). Open channel structure of MscL and the gating mechanism of mechanosensitive channels. *Nature* 418, 942–948.
- [186] Dorwart, M. R., Wray, R., Brautigam, C. A., Jiang, Y. & Blount, P. (2010). *S. aureus* MscL is a pentamer *in vivo* but of variable stoichiometries *in vitro*: implications for detergent-solubilized membrane proteins. *PLOS Biol.* 8(12), e1000555.

- [187] Pfefferkorn C M, Jiang Z & Lee J C 2012. Biophysics of α -synuclein membrane interactions. *Biochim. Biophys. Acta (BBA)-Biomembranes* 1818(2), 162–171.
- [188] O’Leary E I, Jiang Z, Strub M-P & Lee J C 2018. Effects of phosphatidylcholine membrane fluidity on the conformation and aggregation of N-terminally acetylated α -synuclein. *J. Biol. Chem.* 293 11195–205.
- [189] Huang, H. W. & Charron, N. E. (2017). Understanding membrane-active antimicrobial peptides. *Q. Rev. Biophys.* 50, e10.
- [190] Marquette, A. & Bechinger, B. (2018). Biophysical investigations elucidating the mechanisms of action of antimicrobial peptides and their synergism, *Biomolecules* 8(2), 18.
- [191] Bai, X., McMullan, G. & Scheres, S. H. W. (2015). How cryo-EM is revolutionizing structural biology. *Trends Biochem. Sci.* 40(1), 49–57.
- [192] Singh, A. K., McGoldrick, L. L. & Sobolevsky, A. I. (2018). Structure and gating mechanism of the transient receptor potential channel TRPV3. *Nat. Struct. Mol. Biol.* 25, 805–813.
- [193] Zubcevic, L., Herzik, M. A., Wu, M., Borschel, W. F., Hirschi, M., Song, A. S., Lander, G. C. & Lee, S. Y. (2018). Conformational ensemble of the human TRPV3 ion channel. *Nat. Commun.* 9, 4773.